UNIVERSITY
OF
JOHANNESBURG

FATE AND BEHAVIOUR OF WO_3 NANOPARTICLES IN WASTEWATER TREATMENT PLANT

---

by

Sandile Simelane

(201214396)

Dissertation in fulfilment of the requirement for the degree

MASTER OF SCIENCE

in

CHEMISTRY

in the

FACULTY OF SCIENCE

of the

UNIVERSITY OF JOHANNESBURG

Supervisor : Dr. L.N. Dlamini

Co-supervisor : Prof. J.C. Ngila

DECLARATION

I hereby declare that this dissertation, which I herewith submit for the research qualification

MASTER OF SCIENCE DEGREE IN CHEMISTRY

to the University of Johannesburg, Department of Applied Chemistry, is, apart from the recognised assistance of my supervisors, my own work and has not previously been submitted by me to another institution to obtain a research diploma or degree.

________________________________ on this 21st day of August 2017

(Sandile Simelane)

________________________________ on this 21st day of August 2017

(Dr. Langelihle N. Dlamini)

________________________________ on this 21st day of August 2017

(Prof. Jane C. Ngila)

DEDICATION

This work is dedicated to the Khumalo family, you have been the parents, brothers and sisters to me that I did not have. I would not have made it without your guidance and love. You are my inspiration and strength to keep moving forward.

ACKNOWLEDGEMENTS

In life, a person never makes it on his own. I am grateful and Sincerely acknowledges my supervisors and friends. I would like to recognize the input, commitment, support and dedication of the following people and institutions:

- My Heavenly father, who had proven to me that life outside him will be void and meaningless. Thank you for the provisions, protection and wisdom. I owe it all to you. YHWH is your name.
- My supervisors: Dr. L.N. Dlamini, and Prof. J.C. Ngila for your unconditional assistance in this journey.
- I am also grateful to Dr. L.N. Dlamini, for his efforts in ensuring a healthy research and learning environment. Your desire Nkhosi Dlamini to impart knowledge and changing my intellect. May God richly bless you and take you to where you see yourself.
- Financial support from UJ Global Excellence Stature (GES), National Research Foundation (NRF), Water Research Commission (WRC) and the University of Johannesburg, Department of Applied Chemistry.
- Dr. S.P. Malinga, for giving up your time, inputs and moral support during our research group presentations provided valuable information and ideas. For that, I am obliged.
- Daspoort wastewater treatment works for having trusted us with access to your facility and for allowing us to use your wastewater.
- Mr. L.C. Mahlalela, a man who not only has become a brother to me but “my twin”. Your love and passion, your support, ideas and to share your knowledge and expertise with me, God bless you twin.
- Mr. E. Ngigi for your friendship, and assistance in the characterization of my samples. I am where I am now because of you. May God keep blessing you.
- To my research group members, Mr. D. Vlotman, Mrs. N.S. Lehutso, Mr. M.M. Thwala, Mr. S. Dube for your input. You have become a part of my family.

- Members of the Department of Applied Chemistry in the Faculty of Science at the University of Johannesburg, I express my gratitude for their friendship and unconditional support during my studies
- My best friend Ms. N. Motsa, Ms. T. Simelane and Mr. N. Ngwenya, your support is amazing.

PRESENTATIONS AND PUBLICATIONS

The work outlined in this dissertation has been submitted to peer-reviewed journals and presented at conferences as shown below:

Presentations

1. S. Simelane, J. C. Ngila, and L. N. Dlamini. Stability and aggregation kinetics of tungsten trioxide nanoparticles in industrial effluent. In **6th University of Johannesburg Inter-Faculty Postgraduate Symposium**, 14th October 2016, Johannesburg, South Africa.
2. S. Simelane, J. C. Ngila, and L. N. Dlamini. Stability and aggregation kinetics of WO_3 nanoparticles in industrial effluent**. In 17 WaterNet/WARFSA/GWP-SA Symposium, Integrated Water Resources Management: Water Security, Sustainability and Development in Eastern and Southern Africa**, 26-28th October 2016, Gaborone, Botswana.
3. S. Simelane, J. C. Ngila, and L. N. Dlamini. The fate, behaviour and effect of WO_3 nanoparticles on the functionality of an anaerobic treatment unit. **In 9th World Congress on Materials Science and Engineering**, June 12-14, 2017, Rome, Italy.

Publications

1. S. Simelane, J. C. Ngila, and L. N. Dlamini (2017). The effects of humic acid on the stability and aggregation kinetics of WO_3 nanoparticles. Particulate Science and Technology accepted manuscript in press http://dx.doi.org/10.1080/02726351.2017.1302536
2. S. Simelane, J. C. Ngila, and L. N. Dlamini. The fate, behaviour and effect of WO_3 nanoparticles on the functionality of an aerobic treatment unit submitted for publication in a peer-reviewed journal.

ABSTRACT

With the widespread use of nanoparticles, a concern has been raised to understand their behaviour in the actual environment. Monoclinic tungsten trioxide nanoparticles (*m*-WO_3) have gained considerate interest as a photocatalyst particularly in the photodegradation of organic pollutants and oxidation of water resulting in the evolution of oxygen. As a result, the increased application will inherently lead to large amounts of *m*-WO_3 being found in wastewater effluent. Wastewater effluent is a confluence of several chemicals; molecules such as natural organic matter, surfactants and amino acids to name a few. Natural organic matter present in wastewater include substances like humic acid and fulvic acid. Thus this study aimed to understand the fate and behaviour of *m*-WO_3 nanoparticles in a wastewater treatment system. This research involved investigation of solution chemistry and its effects on the stability and aggregation kinetics of *m*-WO_3. Thus, accurate characterization of the physicochemical properties was paramount as they could be extrapolated to their toxicological effects. The physicochemical properties measured included size distribution, aggregation/agglomeration, surface area, crystal structure, and surface charge.

In the presence of humic acid, the zeta potential of the nanoparticle was negative at all concentrations. However, the hydrodynamic diameter increased in the presence of divalent cations indicating, a suppressed electric double layer. The agglomeration rate was consistently high around the point-of-zero-charge (pzc), pH 2.5 - resulting in larger hydrodynamic diameters in this range. At pH 5, the rate of agglomeration was found to be reasonable enough to show agglomeration and dispersion of nanoparticles, thus was chosen as the optimum working pH to measure the change in the physicochemical properties of the NPs. Using the DLVO theory, it was evident that the dominant interaction forces were found to be repulsions forces in monovalent cations (Na^+) while the van-der-Waals attractive forces were prevalent when divalent cations (Mg^{2+} and Ca^{2+}) were in solution. In natural waters where humic acid is mostly found, infers that *m*-WO_3 will be dispersed when monovalent cations are predominant, yet, agglomeration of the nanoparticles will be evident when divalent cations are excessive.

Understanding the fate and behaviour of the *m*-WO_3 nanoparticles and how its impacts the functionality on the treatment plant is of paramount importance for accurate toxicological risk assessment. This was achieved through acclimatization of activated sludge to the simulated wastewater treatment plant operated per the Organisation for Economic Co-operation and Development (OECD) 303A guidelines.

During acclimatization, chemical oxygen demand (COD), and a five-day biological oxygen demand (BOD_5) were monitored. Humic acid impact on the functionality of the domestic wastewater treatment plant was investigated as it is a major constituent of wastewater and surface water. The COD removal was above 80% suggesting that humic acid had no impact on the activated sludge activity.

The fate of *m*-WO_3 was monitored using Powder x-ray diffraction (PXRD) and scanning electron microscope coupled with electron dispersive x-ray. Powder x-ray diffraction analysis indicated the presence of *m*-WO_3 in the sludge which was further confirmed with electron dispersive x-ray -mapping which showed the presence of tungsten signifying adsorption of the nanoparticles on the sludge. This is evident that the activity of the activated sludge had no effect on the polymorph of WO_3 as sharp peaks appeared in the PXRD patterns which are indicative of the crystallinity of the *m*-WO_3 in sludge. The addition of 15 mg/L^{-1} *m*-WO_3 showed to influence the functionality of the treatment plant as the COD removal dropped to 70 % which is below the 80% stipulated guideline signifying adequate removal of the CODs. This implied that *m*-WO_3 nanoparticles possess toxicity effects on the activated sludge. An increase in conductivity was observed in the test effluent suggesting the possibility of dissolution of the nanoparticle. The ICP-OES analyses showed that 80% of W was retained in the sludge while 20-21% m/m run out with the effluent.

TABLE OF CONTENTS

LIST OF FIGURES

Section ***Description*** ***Page***

LIST OF TABLES

Section ***Description*** ***Page***

LIST OF ABBREVIATIONS

BET	Brunauer-Emmett-Teller
BOD	Biological oxygen demand
BOD_5	Five-day biological oxygen demand
COD	Chemical oxygen demand
CVD	Chemical vapour deposition
DI	Deionised water
DLS	Dynamic light scattering
DLVO	Derjauin-Landau-Verwey-Overbeek
DNA	Deoxyribonucleic acid
DO	Dissolve oxygen
DRS	Dffuse reflectance spectroscopy
EDL	Electrical double layer
EDS	Energy dispersive X-ray spectroscopy
ELS	Electrophoretic light scattering
ENMs	Engineered nanomaterials
ENPs	Engineered nanoparticles
EPM	Electrophoretic mobility

F/M	Food to microorganism ratio
FAS	Ferrous ammonium sulphate
FTIR	Fourier transform infrared spectroscopy
HA	Humic acid
HRT	Hydraulic retention time
HS	Humic substances
ICP-OES	Inductively coupled plasma – optical emission spectroscopy
IEP	Isoelectric point
MB	Methylene blue
MLSS	Mixed liquor suspended solids
MLVSS	Mixed liquor volatile suspended solids
NIOP	Nano iron oxide particle
NOM	Natural organic matter
NPs	Nanoparticles
nZVI	Nanoscale zerovalent iron
OECD	Organisation for economic co-operation and development
PEG	Polyethylene glycol
pzc	Point-of-zero-charge

RAS	Return activated sludge
RhB	Rhodamine B
ROS	Reactive oxygen species
SD	Standard deviation
SEM	Scanning electron microscopy
SRT	Sludge retention time
SS	Suspended solids
SWTP	Simulated wastewater treatment plant
TDS	Total dissolved solids
TEM	Transmission electron microscopy
TGA	Thermogravimetric analysis
UV	Ultraviolet
V_A	Van der waals attractive forces
V_R	Double layer repulsion
V_T	Net total interaction
WWTPs	Wastewater treatment plants
XPS	X-ray photoelectron spectroscopy
PXRD	Powder X-ray diffraction spectroscopy

CHAPTER 1
INTRODUCTION

1.1 Problem statement

A report released by the Royal Society and the Royal Academy of Engineering in 2004, on nanoscience and nanotechnology drew the attention of environmental managers and policy makers. This is due to the possible toxicological and pathological risks to human health and to the environment that may be presented by engineered nanomaterials from the interface between biotechnology and nanotechnology, as in the development of nanotechnology-based drug delivery systems (The Royal Society & The Royal Academy of Engineering,2004; Moore 2006) In order to accurately assess the risk involved in the use of nanoparticles and consider the eventual environmental liabilities associated with it, a thorough understanding of the behaviour of nanoparticles in organisms and the ecosystem is needed (Belen et al. 2013). Moreover, correlation of the physiological properties of the nanoparticles (NPs) to their fate and behaviour relies on the accurate characterization of the nanoparticles before, during and after applications (Jingkun et al. 2009; Koetsem et al. 2015; Fang et al. 2009).

Nanotechnology holds a great potential in advancing water and wastewater treatment efficiencies (Qu et al. 2013). The production and application quantities of the engineered nanomaterials (ENM's) are growing and it has to be expected that ecosystems will be exposed to significant levels of such materials. The industrial and domestic products and wastewater containing ENM's are released either directly or indirectly into the water systems. Once they are released into the environment, ENM's will to some extent agglomerate with other suspended solids or sediments, potentially accumulate to organisms and finally entre the food chain or drinking water (Gottschalk et al. 2011). ENMs generate reactive oxygen species (ROS) such as free radicals (OH^-), singlet oxygen ($^1O_2$) and superoxides (O_2^-) which exert several adverse effects on microorganisms including disruption of cell wall, damage of DNA/RNA (Eduok et al. 2013; Pelletier et al. 2010). Therefore, ENM’s are among the increasing emerging contaminants in the wastewater treatment plant (WWTP) (Gottschalk et al. 2011).

WWTPs have been utilized for the removal and/or degradation of contaminants from wastewater for generations, and they still play a pivotal role in the sustainable wastewater recycling. The treated wastewater effluent is discharged into the natural water reservoirs that include rivers and lakes. The sludge generated during wastewater treatment has several applications that include use as fertilizer in agriculture. However, under certain circumstances, the sludge is disposed for incineration where the residue ashes are landfilled or the sludge is landfilled without any further treatment (Chaúque 2014). Once NPs are in are in the soil, several processes can affect their fate and bioavailability. These key processes include dissolution, sorption/aggregation, plant bioaccumulation, invertebrate accumulation and toxicity, microbial toxicity and particle migration (Klaine et al. 2008). Furthermore, soil treatment with nC_{60} had no effect on respiration, microbial biomass, and protozoan abundance, however reduction in numbers of bacteria, a shift in bacterial and protozoan gene patterns have been reported (Brar et al. 2010; Klaine et al. 2008).

1.2 Justification

The development and manufacturing of nanomaterials have increased rapidly with the global market estimated to have reached $1 trillion in 2015 with more than 1600 commercial products containing ENMs available (Jennings et al. 2015). Nanoscience and nanotechnology are widely seen as having huge benefits to many areas and are attracting investments from governments and business in many parts of the world. Yet their application in different scientific fields including engineering, biotechnology, biomedical, environmental and materials sciences may raise new challenges in the safety, regulatory or ethics domain (Sillanpää et al. 2011; The Royal Society & The Royal Academy of Engineering,2004).

Therefore, exposure assessment is very important because their environmental impact is poorly understood as they are released into the biosphere whether inadvertently of intentionally (Dwivedi et al. 2015). The interaction between the

NPs and water components in the formation or breakage of aggregates is mainly determined by their surface properties which are controlled by the solution chemistry (Baalousha 2009; Zhou et al. 2015). Solution pH and surface charge mainly govern the stability of NPs in aqueous solution. NPs are mobile in most pH ranges except where the pH is close to the point of zero charge. Inorganic salts also have a direct effect on the NPs aggregation and addictive's such as surfactants and natural organic matter significantly improves the dispersion of NPs. The natural environment, groundwater aquifers and surface water have high concentrations of magnesium and calcium which favour high aggregation and deposition of NPs (Finnegan 2006; Snoswell et al. 2005; Fang et al. 2009). This, therefore, makes wastewater an appropriate matrix for the investigation of the behaviour of NPs as all these properties greatly vary.

WWTP receives a significant amount of nanomaterials from both domestic and industrial sources. Some are expected to precipitate into the sludge but may find their way back into the aquatic system via sludge used as fertilizers and the remaining effluent will enter directly into both freshwater and marine environment (Jennings et al. 2015). Thus, understanding the fate and behaviour of the nanoparticles in different environmental matrices is crucial for predicting their potential ecotoxic effects in various environmental species (The Royal Society & The Royal Academy of Engineering,2004).

1.3 Aim and Objectives

The aim of the study was:

To monitor the fate and behaviour pristine WO_3 nanoparticles in a simulated wastewater treatment plant (SWTP) by monitoring their physicochemical properties.

The objectives of the study were:

I. To synthesize and characterize pristine WO_3 nanoparticles (NPs)

II. To measure and monitor the chemical stability of WO_3 NPs by varying ionic strength, pH, electrolyte and NOM.

III. To monitor the WO_3 present in the sludge and effluent and determine the mass balance.

IV. To determine the effect of WO_3 on the functionality of a WWTP by monitoring factors including COD, BOD_5, TDS and conductivity.

1.4 Outline of the Dissertation

From this chapter the dissertation continues as follows:

Chapter 2 details the literature review on WO_3 nanoparticles synthetic routes and its properties. A review on the stability of nanoparticles and how they can be transported or rather react in the environment is also presented. The wastewater treatment process is also examined and the important factors that influence the wastewater treatment processes.

Chapter 3 outlines the methodology employed to meet the objectives of this work. The synthetic route and characterization techniques are detailed in this chapter as well as the setup and simulation of the WWTP.

Chapter 4 summarizes the characterization of WO_3 nanoparticles and provides information on how the stability of the nanoparticles is influenced by pH, Ionic strength, electrolytes and humic acid. The aggregation kinetics of the nanoparticles under this conditions is explained

Chapter 5 describes the fate and behaviour of WO_3 nanoparticles in a SWTP. The impact of the nanoparticles on the functionality of the treatment plant is also explained and the mass balance of WO_3 introduced in the system is provided.

Chapter 6 (Conclusions and recommendations) provides the key findings of this research work and further provides recommendations on further work relating to providing an accurate risk assessment of WO_3 nanoparticles in the environment.

References are listed at the end of each chapter.

Appendix section: selected prominent data are detailed in this section.

1.5 References

Baalousha, M., 2009. Aggregation and disaggregation of iron oxide nanoparticles: Influence of particle concentration, pH and natural organic matter. Science of the *Total Environment, 407(6),* pp.2093–2101.

Belen, M., Fidalgo, M.M. & Cortalezzi, D., 2013. An experimental study on the aggregation of TiO_2 nanoparticles under environmentally relevant conditions. *Water Research, 47(12)*, pp.3887–3898.

Brar,S. K., Vermab, M., Tyagi, R. D., & Surampalli, R.Y., 2010. Engineered nanoparticles in wastewater and wastewater sludge – Evidence and impacts. *Waste Management, 30(3),* pp.504–520.

Chaúque, E.F., 2014. Monitoring of Physiochemical Parameters and the Behaviour of Zinc Oxide Nanoparticles in a Simulated Wastewater Treatment Plant. The university of Johannesburg @ https://ujdigispace.uj.ac.za/handle/10210/11321. Accessed 15 March 2016.

Dwivedi, A.D., Dubeya,S. P., Sillanpääa, M., Kwonb, Y., Leeb, C., Varma, R. S., 2015. Fate of engineered nanoparticles: Implications in the environment. *Coordination Chemistry Reviews, 287,* pp.64–78.

Eduok, S., Martin, B., Villa, R. Nocker, A., Jefferson, B.,& Coulon, F., 2013. Evaluation of engineered nanoparticle toxic effect on wastewater microorganisms: Current status and challenges. *Ecotoxicology and Environmental Safety, 95*, pp.1–9.

Fang, J., Shana, X., Wena, B., Lin, J., & Owens, G., 2009. Stability of titania nanoparticles in soil suspensions and transport in saturated homogeneous soil columns. *Environmental Pollution, 157(4)*, pp.1101–1109.

Finnegan, M.P., 2006. Influence of Surface Potential on Aggregation and Transport of Titania Nanoparticles. *Environmental Science Technololgy, 40(24),* pp.7688–7693.

Gottschalk, F., Ort, C., Scholz, R. W. & Nowack, B, 2011. Engineered nanomaterials in rivers - Exposure scenarios for Switzerland at high spatial and temporal resolution. *Environmental Pollution, 159(12),* pp.3439–3445.

Jennings, V., Goodhead, R. & Tyler, C.R., 2015. Ecotoxicology of Nanomaterials in Aquatic Systems. *Frontiers of Nanoscience, 8*, pp.3-45.

Jingkun Jiang, Pratim Biswas, Gunter Oberdorster, 2009. Characterization of size , surface charge , and agglomeration state of nanoparticle dispersions for toxicological studies. *Journal of Nanoparticle Research, 11,* pp.77–89.

Klaine, S.J., Alvarez, P. J. J., Batley, G. E., Fernandes,T.F., Handy, D. R., Lyon, D.Y., Mahendra,S., Mclaughlin, M. J., & Lead, J. R.,, 2008. Nanomaterials in the Environment: Behaviour, fate, bioavailability and effects. Environmental T*oxicology and Chemistry, 27(9),* pp.1825–1851.

Van Koetsema, F., Geremewa, T. T., Wallaertb, E., Kim V, Van der Meerenc, P., & Du Laing, G., 2015. Fate of engineered nanomaterials in surface water : Factors affecting interactions of Ag and CeO_2 nanoparticles with (re) suspended sediments. *Ecological Engineering, 80,* pp.140–150.

Moore, M.N., 2006. Do nanoparticles present ecotoxicological risks for the health of the aquatic environment? *Environment International, 32(8)*, pp.967–976.

Pelletier, D. A., Suresh, A. K., Holton, G. A., McKeown, C. K., Wang, W., Gu, B., Mortensen, N. P., Allison, David P., Joy, D. C., Allison, M. R., Brown, S. D., Phelps, T. J., & Doktycz, M. J., 2010. Effects of engineered cerium oxide nanoparticles on bacterial growth and viability. *Applied and Environmental Microbiology, 76(24), pp.7981–7989.*

Qu, X., Alvarez, P.J.J. & Li, Q., 2013. Applications of nanotechnology in water and wastewater treatment. *Water Research, 47(12*), pp.3931–3946.

Sillanpää, M., Paunu, T. & Sainio, P., 2011. Aggregation and deposition of engineered TiO2 nanoparticles in natural fresh and brackish waters. *Journal of Physics:12018(Conference Series 304),* pp.1–8.

Snoswell, D. R. E., Duan, J., Fornasiero, D. & Ralston, J., 2005. Colloid stability of synthetic titania and the influence of surface roughness. J*ournal of Colloid and Interface Science, 286*, pp.526–535.

The Royal Society & The Royal Academy of Engineering,2004. Nanoscience and nanotechnologies: opportunities and uncertainties. *The Royal Society*, RS policy document 19/04, 1-116, London.

Zhou, X. Huang,Zhou, B., Tao, L.,Shi,Y., 2015. Aggregation behaviour of engineered nanoparticles and their impact on activated sludge in wastewater treatment. *Chemosphere, 119, pp.568–76.*

CHAPTER 2
LITERATURE REVIEW

2.1 Introduction

Nanomaterials are defined as materials smaller than 100 nm in at least one of the three dimensions. At this scale, materials possess novel sized-dependent properties different from their large counterparts and they are controlled by effects of quantum mechanics rather than classical physics, many of which have been explored for applications in water and wastewater treatment (Qu, Alvarez, & Li 2013; Barkalina et al. 2014). ENMs can be homogeneous or heterogeneous, these include particles with core-shell structure in terms of structure and composition or multi-functional nanoparticles. They also have different morphologies such as sphere, needles, tubes and plates with differing properties that can respond uniquely to organisms and the environment. Unlike metal salts in solution, the main component of nanoparticles are normally not ionized, their oxidation state is often zero (Min et al. 2016).

Nanoparticles can be surface coated intentionally (polymers and proteins) or naturally (NOMs) and such coatings determine their environmental fate and behaviour. These coatings influence how ENMs aggregate, their reactivity and their behaviour in the WWTP.

Nanoparticles have been classified among the emerging contaminants, posing challenges to conventional waste treatment system (Demirel 2016). A shortfall in the wastewater plant efficiency would have adverse effects on the environment and the quality of life. The entrance of NPs in the wastewater stream results in them being found in the treatment plant where they have been said to inhibit bacterial species in the in the activated sludge and result in a reduction in the efficiency in the biological WWTP (Puay, Qiu, & Ting 2015). NPs enters the environment and WWTP either from direct or indirect sources. Direct release occurs through open windows to air when powdery materials are used unconsciously or from transport accidents and from all kind of spills. The indirect release is when surface run-off, domestic and industrial wastewater effluent containing NP is drained to the river and marine environment (Jennings, Goodhead, & Tyler 2015; Fadri Gottschalk & Nowack 2011; Moore 2006; F. Gottschalk et al. 2011).

2.2 Physicochemical properties of NPs

ENMs possess structure dependent properties such as chemical, mechanical, electrical, optical, and biological. These properties may potentially lead to nanostructure-dependent biological activities that differ and is not directly predicted by the bulk properties of the constituent chemicals and compounds. The biological activity of particles increases as the particles size decreases, smaller particles occupy less volume, resulting in a large number of particles with a greater surface area per unit mass and increased the potential for biological interaction (Oberdörster et al. 2005). NPs aggregates can either homo/hetero-aggregates. The ENM's reactivity relies on the surface area to volume ratio which gets reduced during aggregation. The sedimentation rate, organisms uptake, toxicity and transportation of NP is dependent on ENM size (Ranville, Manuel D. Montaño & James 2014). **Table 2.1** summarizes different ENMs properties and provides a brief explanation of the significance of these properties (Tiede et al. 2008).

Table 2.1: Nanoparticle properties and their importance for measurement (Tiede et al. 2008).

Property	**Importance of measurement**
Aggregation	Nanoparticles that tend to aggregate may keep their functionality, however, the increase in size could lead to decrease in uptake
Elemental composition	Different particle composition leads to different behaviour/impact, e.g. Cd versus Fe
Mass concentration	Normally increased contaminant concentration leads to increase in toxicity/impact, this is no always applicable for

	nanoparticles
Particle number concentration	Nanoparticles have low mass concentrations but show high percentage of total particle numbers
Shape	Different particle shapes (e.g. spherical, tubular) can possess different affinities or accessibilities, e.g. transport through membranes into cells, different antibacterial behaviour
Size and size distribution	Nanoparticles are defined and classed by their size, and size is one of the primary properties describing transport behaviour
Solubility	Soluble nanoparticles; their ionic form can be harmful or toxic (e.g. ZnO versus Zn^{2+})
Speciation	Different species can have different behaviour, toxicity, impact (e.g. C_{60} versus C_{70}, ENP complexes with natural organic matter or oxidation state)
Structure	The structure can influence stability or behaviour (e.g. rutile or anatase as possible crystal structures of TiO_2)
Surface area (and porosity)	Increase in surface area increases reactivity and sorption behaviour
Surface charge	Surface charge has influence on particle stability especially in dispersions
Surface chemistry	Coatings can consist of different chemical compositions and influence particle behaviour or toxicity (e.g. quantum dots with CdSe core and ZnS shell)

2.3 Tungsten trioxide (WO_3)

Due to the economic benefits of using visible light radiation and because of its predominance in the solar spectrum, the development of photocatalysts with high activity under visible light radiation is desirable(Vamvasakis et al. 2015). Tungsten trioxide (WO_3) is a visible light responsive photocatalyst that absorbs radiation in the region up to 500 nm (Liu et al. 2007; Vamvasakis et al. 2015). Its main disadvantage though is that bare WO_3 has lower light energy conversion efficiency than the widely used TiO_2. Its advantages are, easily preparation of high purity NPs, strong absorption in near ultraviolet and visible regions, and long-term stability during irradiation in a variety of aqueous electrolytes (Liu et al. 2007). WO_3 has a band gap ranging from 2.2 to 3.2 eV (Di Valentin et al. 2013; Liu et al. 2007; Vamvasakis et al. 2015).

WO_3 possess different crystalline phases as shown in **Table 2.2**, originating from the three-dimensional array of the corner and edged sharing WO_6 metal-oxygen octahedra in the original structure. The distortion is a result of the tungsten atom being displaced from the octahedral centre and this displacement is temperature dependent. The crystalline phase has been observed between the temperature range of <123K to 1013K and it consists mainly monoclinic, triclinic, orthorhombic and tetragonal obtained through the annealing and cooling process (Hai-Ning Cui 2011; Baserga et al. 2007).

Table 2.2: Show different WO_3 crystal structures and occurrence temperature (Zheng et al. 2011).

Crystal structure	Crystalline phase	Temperature formation
Monoclinic II	ε-WO_3	<-43
Triclinic	δ-WO_3	-43 to 17
Monoclinic I	Ƴ-WO_3	17 to 330
Orthorhombic	β-WO_3	330 to 740
Tetragonal	α-WO_3	>740

However, these crystalline phases are partly reversible resulting in the monoclinic phase being the most stable. Because of the existence of the corner-sharing in the WO_3, it possesses the perovskite-like atomic configuration structure as illustrated in **Figure 2.1** (Hai-Ning Cui 2011; Baserga et al. 2007) and the polyhedral representation of the different polymorphs is shown in **Figure 2.2**.

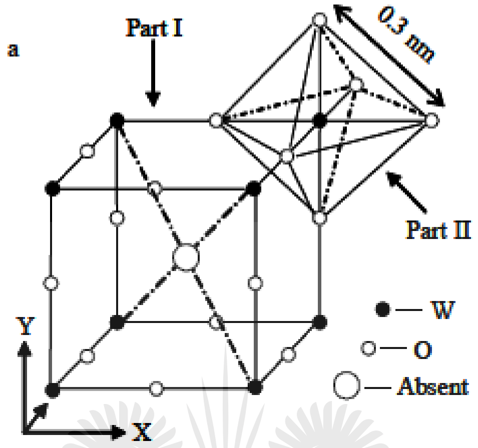

Figure 0.1: Unit cell for the perovskite lattice (Part I) and octahedral symmetries (Part II) in the perovskite structure (Hai-Ning Cui 2011).

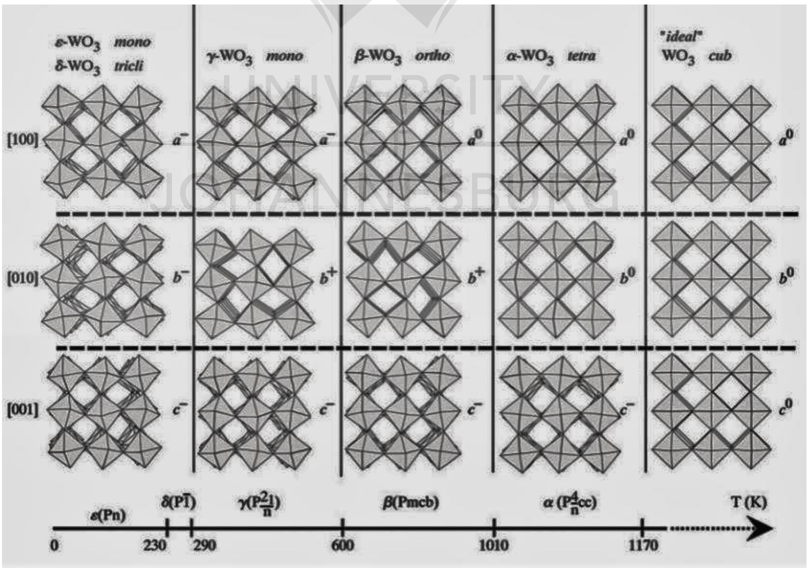

Figure 2.2: Tilt patterns and stability temperature domains of the different polymorphs of WO_3 (Zheng et al. 2011)**.**

When WO_3 is under neutral electrical conditions, two structural models can be expected. Supposing one-half of the crystallographic plan of the W atoms, in the valence state W^{6+} connected to terminal oxygen ions resulting in a transfer of electrons to the nearest W ion thus forming a W^{5+} state while in the other part W atoms at the surface changes their valence state to W^{5+} to represent the surface by $W^{5+}O_{20}$ as shown in **Figure 2.3**. The formation of W^{6+}-OH results from oxidation reaction with atmospheric air in humid conditions (Kuzmin et al. 1998).

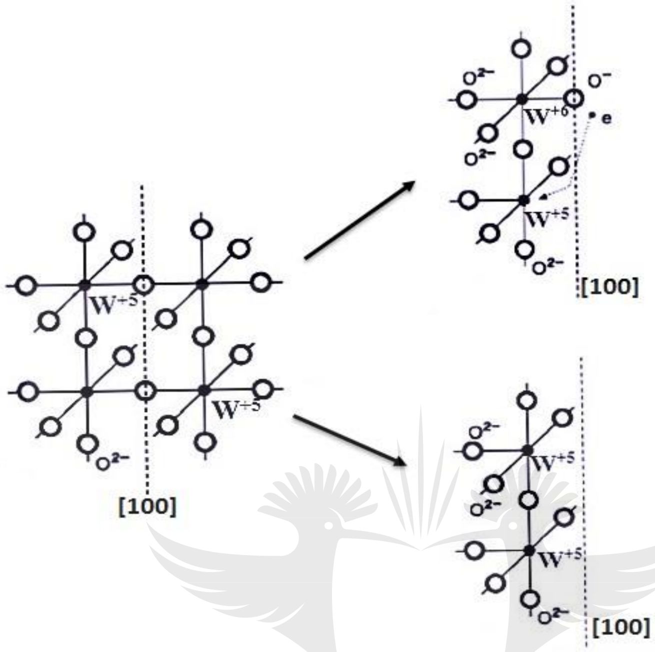

Figure 2.3: Structural model of monoclinic WO_3 grain surface along (100) with two possible states (Qadri 2014).

2.3.1 Synthesis of WO_3

Nanoparticle synthesis and assembly strategies mostly involve precursors from whether liquid, solid and gas phase while using either chemical or physical deposition approaches (Saravanan et al. 2008). The variety of techniques used can be classified into either top-down or bottom-up approach. The bottom-up approach includes miniaturization of materials components up to atomic level with a further self-assembly process leading to nanostructure formation. During the self-assembly process, physical forces operating at nanoscale are used to combine basic units into larger stable structures. This approach consists of chemical synthesis, chemical vapour deposition, thermal spray technique, inert gas condensation, rapid solidification and electrodeposition (Saravanan et al. 2008).

Numerous methods such as pyrolysis, thermal decomposition, colloidal chemistry routine, Chemical vapour deposition (CVD), hydrothermal reactions, pulse laser deposition, sol-gel (Shah & Muzyyan 2009; Wicaksana et al. 2014; Nogueira et al. 2004; Vijayakumar et al. 2015), microwave-solvothermal (Wu et al. 2008) method, emulsion technique(Abazari & Sanati 2013), solid-state methods (Mu et al. 2015) have been used to prepare WO_3 nanostructure.

According to R. Abazari et al., these methods are complex and involve a series of steps to perform yet their yield is low. Hydrothermal method is the most commonly used technique, however, it still requires prolong reaction times and highly controlled reaction conditions such as pH, temperature and templates (Mu et al. 2015). The emulsion technique may be used to synthesise nanostructures with controlled size, morphology and crystallinity (Abazari & Sanati 2013).

2.3.1.1 Sol-gel synthesis

The sol-gel method is a wet chemistry technique used in the preparation of ceramic from liquid precursors to a sol and a network structure called ‘gel’ (Danks et al. 2015; Tseng et al. 2010). The starting materials for this process involves a metal and metalloid elements surrounded by different ligands which undergo various forms of hydrolysis and polycondensation reactions (Brinker & Scherer 1990). The formation of a metal oxide is made possible by connecting the metal centres with either oxo (M–O–M) or hydroxo (M–OH–M) bridges, and generating metal-oxo or metal-hydroxo polymers in solution(Tseng et al. 2010) as shown in equation **2.1**, **2.2a**, and **2.2b** below.

$W\text{-}OR + H_2O = W\text{-}OH + ROH$ (hydrolysis) **(2.1)**

$W\text{-}OH + OR\text{-}W = W\text{-}O\text{-}W + ROH$ (condensation) **(2.22a)**

$W\text{-}OH + HO\text{-}W = W\text{-}O\text{-}W + H_2O$ (condensation) **(2.2b)**

The sol-gel process is affected by the R-group present, the ratio of water to alkoxide and presence and concentration of catalysts (Simonsen & Søgaard 2010;

Danks et al. 2015). The synthetic route of the sol-gel process such as polymerization and polycondensation of metal alkoxide, ion exchange method and the oxidizing reaction of metallic W with a solution of hydrogen peroxide is determined by the starting materials present (Dimitriev et al. 2005). The main advantage of this process is centred on its ability to produce solid-state materials from a homogenized chemical precursor achieved by trapping the “randomness of the solution state” thus ensuring atomic level mixing of precursors. The sol-gel method provides control over size and morphology of particles produced while heating and the reaction time does influence these properties (Danks et al. 2015).

2.3.1.2 Hydrothermal synthesis

Hydrothermal synthesis is generally defined as crystal, synthesis or crystal growth under high temperature and pressure water conditions from substances which are insoluble under ordinary temperature and pressure. The particle size of metal oxide depends on the hydrolysis rate and solubility of the metal oxide itself. When synthesising under supercritical water the rate is enhanced 10^3 times than under the conventional hydrothermal conditions (Hayashi & Hakuta 2010; Khanjani & Morsali 2010).

This method has been achieved by either using the batch type reaction or the continuous flow type thus. In this method, the control of reaction conditions is achieved by instantaneous mixing. Sudden temperature increase, results in supersaturation and rapid heating which is paramount in producing small and homogenous NPs (Aoki et al. 2016).

2.3.1.3 Precipitation synthesis

The homogeneous precipitation method is the most attractive method considering its low cost, use in large-scale industrial production without utilizing expensive raw materials and sophisticated equipment’s (Zhang et al. 2005; Kant et al. 2016). This method produces a high yield. However, it is challenging to obtain high surface area powders because of the irregular particle morphology, large particle size distribution and the high degree of agglomeration (Acarbas et al. 2007). As a result of nonuniform supersaturation in the solution, this could be controlled using homogeneous precipitate that utilizes chemical reaction such as urea decomposition (Acarbas et al. 2007).

Various organic compounds have been used as templates and stabilizers in this method. This includes citric acid, (Sanchez-Martı´nez et al. 2013) urea, (Martínez et al. 2011) polyethylene glycol (PEG), (Luévano-hipólito et al. 2014) and ethanol (Gomez et al. 2013). WO_3 NPs synthesised with citric acid and urea successfully degraded rhodamine B after three hundred minutes (Sanchez-Martı´nez et al. 2013; Martínez et al. 2011). When using citric acid, the synthetic route involves complexation of metal ions by poly-functional carboxyl acid having one hydroxyl group (Sanchez-Martı´nez et al. 2013).

The decomposition of urea in aqueous solution is accompanied by slow and controlled supply of ammonia and carbon dioxide into solution. The smooth pH increase obtained by the degradation of urea in synchrony with the active release of OH^- and CO_3^{2-} ions, usually leads to the precipitation of metal hydrous oxide particles of controlled particle morphology since all microstructural parameters as particle shape and size, specific surface area and porosity are quite sensitive towards pH, metal ion concentration, temperature and aging time (Jan et al. 2006).

In this method, a tungsten salt soluble in water is widely used as a precursor. Synthesis variables such as the time employed in the formation of the WO_3 precursor in aqueous media and subsequent calcination at the appropriate temperature can be modified in order to obtain materials with different textural properties (Sa & Lo 2010).

2.3.1.4 Spray pyrolysis synthesis

Spray pyrolysis is an example of a breakdown method. The powder prepared by this method when compared to those of wet chemical ones are more crystalline, less aggregates with higher purity and have large surface areas. This method further provides a continuous preparation flow of NPs (Lee et al. 2012; Ghaffarian et al. 2011; Arutanti et al. 2014).

In this method, the starting material is first dissolved in a solvent. Droplets will then be produced from the solution through atomization process and later introduced to the furnace for solvent evaporation, diffusion of solute, drying and finally precipitation. The necessary treatment equipment for this method is summarized in **Figure 2.4** it includes an atomizer or nebulizer that converts the starting solution to droplets, a carrier gas(es), tubular furnace/reactor, and sampler or precipitator (Okuyama & Lenggoro 2003).

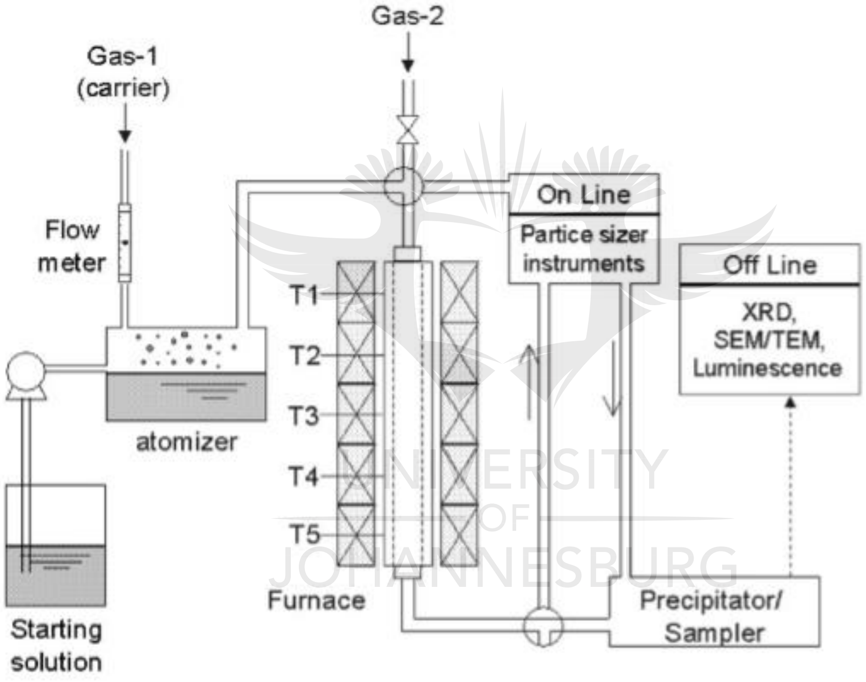

Figure 2.4: Representative spray pyrolysis system (Okuyama & Lenggoro 2003).

For instance, Ghaffarian et al. 2011 synthesised ZnO NPs using this method. The precursor solution was atomized under seven (7) bar of air. The produced droplets were then decomposed at 1000 ˚C in a reactor. The precipitate was then collected and dried at 100 ˚C. Any unreacted precursor material was removed by washing the precipitate with water.

2.3.2 Modification of WO_3

Bare WO_3 has poor light energy conversion efficiency than the most commonly used semiconductor (TiO_2). This is so because the conduction band level of WO_3 is more positive than that of TiO_2 (Chen et al. 2015; Liu et al. 2007). The limitations can be improved by doping with transition elements such as Cu, Cr, Ti, Fe, Al, Zr, Zn, Mn, Al including noble metals. Doping can also be achieved by depositing WO_3 on the surface of other semiconductors like TiO_2, SnO_2, AgBr, and ZnO_2 (Hameed et al. 2004; shokkumar, M., & Maruthamuthu, P., 1989; Ostachaviciute et al. 2010; Liu et al. 2007). Non-metal doping (nitrogen) of WO_3 have also been reported for valence band modification (Cole et al. 2006). Some examples of doping and the typical parameters investigated are given in **Table 2.3**. Doping or rather depositing WO_3 on the surface of ZnO, SnO_2 and TiO_2 nanoparticles can promote charge separation since the band gap of WO_3 is low and photogenerated carriers easily accumulate in its conductor or valence band (Liu et al. 2007; Ostachaviciute et al. 2010).

Table 2.3: Modified WO_3 and the typical parameters being investigated as well as the method used.

Photocatalyst	**Typical parameters of photocatalytic experiments**	**Method used for synthesis**	**Reference**
WO_3/TiO_2	photocatalytic degradation of RhB	facile sol–gel	(Bai et al. 2015)
Mo-doped WO_3	decomposition of the aqueous MB	hydrothermal method	(Song et al. 2010)
Se-WO_3	oxidation of organic pollutants	electrochemical deposition	(Ostachaviciute et al. 2010)
Ag_3PO_4–WO_3	reduction of Cr(VI) and degradation of orange II	deposition–precipitation process.	(Cai et al. 2015)

WO_3/ZnO	degradation and mineralization of chlorinated phenoxyacetic acid herbicides	hydrothermal– deposition	(Lam et al. 2015)

2.3.3 Properties of WO_3

Tungsten trioxide is an *n*-type semiconductor material with a relatively small indirect band gap of 2.2-3.2 eV. WO_3 has high chemical stability in both corrosion and photocorrosion and cannot be further oxidized (Ali Fakhria & Behrouzc 2015). Such stability allows WO_3 to possess many distinctive properties such as chromism (electrochromism, photochromism), photocatalysis, photoluminescence, (Abazari & Sanati 2013) and gas sensing (Susanti et al. 2012).

WO_3 has a melting point of 1473 °C and is soluble in alkalis and insoluble in water with a density of 7.16 g/cm^3. The nanoparticle of WO_3 as photo-electrochemical cells have several advantages due to their superior physical properties including:

1. Higher surface area to volume ratio, which increases the number of reaction sites for water photolysis;

2. Suppressed charge carrier recombination rates, since photogenerated holes are more likely to diffuse to the photoanode/electrolyte interfaces before recombination in nanomaterials with sizes smaller than their hole diffusion lengths (the hole diffusion length of WO_3 is ~150 nm);

3. Enhanced optical absorption, which results from increased optical path length by incident light scattering, caused by the change of refractive indices at the boundaries of grains of different orientations.

However, grain boundaries also act as transportation barriers to photogenerated electron-hole pairs and so it is essential to optimize the sizes of the nanomaterials by varying the synthesis parameters in order to obtain optimal photo-electrochemical performance (Kwong et al. 2013).

Application of voltage pulse in nanomaterial's of WO_3 results in electrochromism, which is the persistence and reversible changes in optical properties revealed in colour changes (Zhang et al. 2010; Zhang et al. 2011). The electrochromism in WO_3 films may be observed in electrochromism devices composed of the film sandwiched between a transparent electrode and an electrolyte and a counter electrode. Application of a negative voltage between the transparent and the counter electrodes causes a blue coloration of the initially transparent WO_3 film while inversion of the biasing voltage renders this film transparent again (bleaches the film). The coloration may be divided into two parts: an initial fast followed by a second slower one. The former has been attributed to the injection of electrons into the initially empty conduction band of the WO_3, the bottom of which is formed by the overlap of the d bands of the metallic ions. Due to the low mobility of *d* electrons and their localization near the metallic ions, they correlate; the electrostatic repulsions between them causing the splitting of this *d*-like band in two sub-bands. The electronic transitions between these two bands cause the initial fast part of the observed coloration (Kostis et al. 2013).

2.3.4 Application of WO_3

Transition metal oxide systems exhibit numerous exciting properties in the arena of superconductivity, colossal magnetoresistance effect, piezoelectricity, microelectronics, photonics and photocatalysis (Kumar & Mohanta 2011). As a result, their applications ranges from smart windows technology to dye-sensitized solar cells, (Zheng et al. 2010) from sensors to photo-electrochemical water splitting, from high Tc superconductivity to heterogeneous catalysis (Di Valentin et al. 2013).

Its technological applications include the construction of infrared switching devices, writing–reading erasing optical devices, gas sensors for the determination of hydrogen, ammonia and nitrogen and also used in temperature sensors and in detecting air humidity (Vijayakumar et al. 2015). WO_3 has been widely applied as a colloidal quantum dot light emitting device, (Wood et al. 2009) bulk-hetero-junction solar cells, (Simchi et al. 2014) optical modulation devices and large information display (Li et al. 2010).

Environmental applications may also benefit with the use of WO_3 in the photocatalytic reduction process of CO_2 into hydrocarbon fuels, (Chen et al. 2012) bacteria destruction,(Wang et al. 2009) and visible light photocatalyst to generate OH radicals in the wastewater treatment (Chen et al. 2012).

2.3.5 Toxicity of tungsten compounds

The study of the toxicity of tungsten and its compounds is still at infant stages even though there is emerging evidence of its health effects (Witten et al. 2012). Dissolution of metallic tungsten can have adverse effects on the environment including soil acidification and direct or indirect toxic effects on plants, soil microorganisms and invertebrates. Acidification often favours the formation of polytungstates which are considered to be antiviral, antitumoral and antimicrobial agents (Strigul et al. 2010). Thus, the toxicity of tungsten compounds depends on the chemical forms of the tungsten compounds and the exposure pathway (Strigul et al. 2005). This was supported by work done by Strigul et al. 2010 which found that sodium metatungstate was significantly more toxic than sodium tungstate.

Research has also shown that tungsten can replace molybdenum in both plants and microbial enzymes leading to the functional activity of the enzyme being reduced. This often results in alteration of the nitrogen cycle in which the molybdenum-containing enzymes plays a significant role in inhibiting both the nitrogenase and nitrate reductase activity in heterocystic cyanobacterium *Anabeana sphaerica* (Strigul et al. 2009).

The toxicological effects of tungsten on adult animals have been witnessed only at high tungsten compounds concentrations. Tungsten has been reported to demonstrate fetus toxicity and affects the early stages of fish development. The mechanisms of these effects remain unknown due scarcity of experimental data thus more research needs to be done in this direction (Strigul et al. 2009). At present, there are no drinking water standards or discharge limits in the South Africa. The Russian Federation regulates tungsten in drinking water (0.05 mg/L) and fishing lakes and rivers (0.0008 mg/L) (Koutsospyros et al. 2006).

2.4 Fate and behaviour of NPs

Several physicochemical properties might have an influence on the fate and transportation of engineered nanoparticles which will vary across the aquatic system and between materials. Aquatic chemistry dictates that interaction between natural water components and ENPs might result in the formation or a break-up of aggregates based on the surface properties of the nanoparticles. However, due to their large surface area, NPs are most likely to bind metal and other water-borne contaminants and presence of these other natural species can also change the surface charge on the NPs (Weinberg et al. 2011). **Table 2.4** shows a summary of commonly studied environmental processes that directly affect ENPs persistence.

Table 2.4: Potential Fate of nanoparticles in the aquatic system (Galyean et al. 2012; Weinberg et al. 2011).

Process	**Implications for Measurement**
Dissolution	Loss of particle state as it becomes dissolved
Deposition	Loss on sample container surface; change in phase during sample processing
Sedimentation	Moving out of suspension; relevant during coagulation treatment
Agglomeration	Target single or clumped particles; increase in surface area increases reactivity and sorption
Decomposition	Biodegradation or change of valence state
Coated	Natural polymers may embed the particles; released before analysis
Association	Sorption to suspended matter could increase their removal during treatment
Reaction	Affected by photolysis, biological, or chemical mechanisms

Dissolution is also related to NP shape and crystal structure; smaller NPs have higher dissolution rates compared to larger particles of the same composition. Depending on the shape and crystal structure, the free energy of the particle is distributed differently, affecting the dissolution and redox-reactions. **Figure 2.5** below illustrates the important physiochemical properties that need to be understood during the characterization (Luyts et al. 2013).

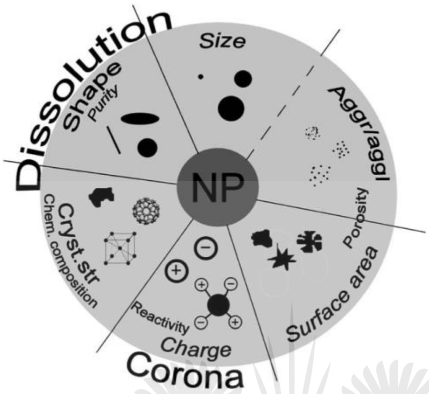

Figure 2.5: Important physio-chemical properties for NP characterization and their interrelations (Luyts et al. 2013).

2.5.1 Effect of abiotic factors on the fate and behaviour of NPs

Several studies have reported that dissolved natural organic matter (NOM), ionic strength, type of electrolyte, aggregation state, and pH can all impact the stability and dissolution of NPs in water (Bian et al. 2011).

2.4.1.1 pH

The pH of a solution is an important controlling parameter in the photocatalytic reduction of metal ions on semiconductor metal oxides. It is responsible for determining the surface charge properties of the photocatalyst and the adsorption behaviour towards pollutants (Yang et al. 2011). Change in pH values can result in a variation on the aggregation of ENPs. Investigations on the effects of pH on graphene oxide (GO) NP in natural and synthetic waters showed that the hydrodynamic diameter (D_h) was approximately 250 nm in the pH range of 4-10, however, increase sharply (>1000nm) in more acidic conditions, that is pH <4. The increase in the D_h was a result of reduced electrostatic repulsive forces between the (GO) NPs (Dwivedi et al. 2015). pH also can change the zeta potential of metal oxides and the changes are significant in the pH range of 6-8. Solutions of NP with negative zeta potential are unlikely to aggregate very rapidly due to the repulsion of their charges (Weinberg et al. 2011). The point of zero charge (PZC) for WO_3 has been reported to be around pH 2.5.The dissolution of this NPs is assisted by different ionic species depending on the position with reference to the PZC (Anik & Cansizoglu 2006; Anik 2006; Anik 2009).

In both before and after the PZC, WO_3 undergo dissolution. Under acidic conditions, the dissolution process is assisted by H^+ and in alkaline medium by OH^-. At the vicinity of the PZC dissolution is H_2O assisted. The dissolution of WO_3 follows the equations below:

$$WO_3(s) + H^+ \rightarrow WO_2OH^+(aq) \qquad \text{acidic medium}$$

$$WO_3(s) + H_2O \rightarrow H_2WO_4(aq) \qquad \text{point of zero charge}$$

$$WO_3\,(s) + OH^- \rightarrow WO_4^{2-}(aq) + H^+ \qquad \text{alkaline medium}$$

2.4.1.2 Type of electrolyte

In different electrolyte solutions, TiO_2 NPs have been reported to form aggregates. Divalent cations may cause aggregation at a wider range of pH compared to monovalent cations. This is due to the specific adsorption effect that prevents the surface charge acquiring a negative charge large enough to create a potential barrier large enough to stop aggregation. The stabilization effect of NOM overrides the divalent ions influence towards aggregation at low cation concentrations. At high concentrations, cations such as Ca^{2+} neutralizes the electrostatic stabilization thus inducing aggregation. This is not observed with Mg^{2+} though, suggesting the existence of Ca^{2+}-NOM interactions such as calcium bridges (Belen et al. 2013; Weinberg et al. 2011).

A similar observation was made by Peng et al. 2015 that ZnO NPs has a higher aggregation rates in presence of divalent ions compared monovalent ions. This is ascribed to the fact that high concentration of electrolyte or higher valent counter-ions causes reduction in energy barriers thus enhancing aggregation.

2.4.1.3 Ionic strength

The stability of metal oxide NPs in aqueous solution depends greatly on the ionic strength of the medium. The increase in ionic strength often results in a decrease in zeta potential. NPs interaction becomes repulsive at low ionic strength. The repulsive electric double layer decreases as the ionic strength increases resulting to net zero interaction forces thus high rate of agglomeration and sedimentation. This is due to high ionic strength compressing the electric double layer thus reducing the repulsive forces in the process (French et al. 2009; Bian et al. 2011).

2.4.1.4 Interaction with macromolecules

The chemistry between the different NP properties and also interfaces with their environment determine the biological activity and toxicity of NPs (Luyts et al. 2013). ENMs are mostly designed with macromolecular coatings such as polymers, and proteins for determination of their environmental fate and behaviour. Both coated and uncoated will also interact with natural macromolecules, such as natural organic matter (NOM) or humic substances, and proteins when introduced into a natural aqueous environment or up taken by an organism (Louie et al. 2016). Thus, these natural macromolecules will tend to determine the final size of the NPs (Belen et al. 2013). Depending on the surface charge, different kinds of proteins present in the dispersant, culture medium or biological fluid will adhere to the NP surface thereby blocking particular parts of the NP surface. As a consequence, the particle will interact differently with its surrounding milieu and maybe this will change its reactivity and aggregation properties (Luyts et al. 2013).

Metal oxides NPs adsorb to NOM thus reducing their aggregation in the natural aquatic environment (Weinberg et al. 2011). Various studies proposed that NOM provides steric repulsion forces that can possible prevents aggregation or produces disaggregation of NPs aggregates leading to a higher dispersion than expected (Belen et al. 2013; Bian et al. 2011).

2.4.1.4.1 Humic Acid

Humic acids (HA) are macromolecules with a molecular size ranging from 10 000 to 100 000 comprising of humic substances (HS). HA is dark brown to black in colour. HS are organic in nature and they are found in the terrestrial soil, natural water and in sediments. They are mainly products of decayed vegetation and natural residues. Commercial HA is mainly extracted from peat and coal. This constitutes of weak aliphatic carbon chains and aromatic organic acids. HAs are considered to be flexible linear polymers with random coils with cross-linked bonds (Robert E. Pettit n.d.; de Melo et al. 2015).

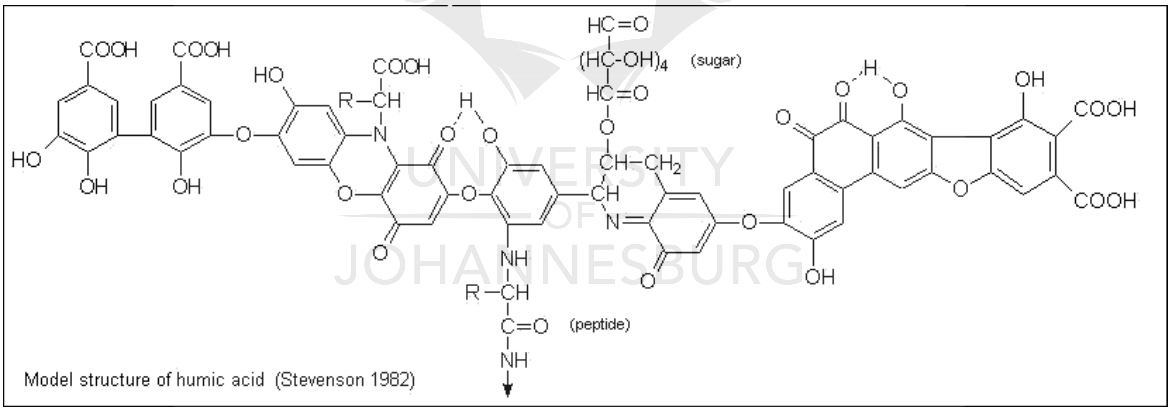

Model structure of humic acid (Stevenson 1982)

Figure 2.6: A structural illustration of humic acid.

2.4.1.4.2 Properties of HA

HA differs from the other HS such as fulvic acid and humins in that, it is soluble in alkaline media, partly soluble in water and insoluble in acidic medium with pH<2. This classification, however, could vary depending on the HA composition parameters such as pH and ionic strength. The functions of HA are attributed mainly to the presence of the phenol and carboxylic acids functional group which enables the deprotonation of the OH/OOH. Furthermore, HA forms salts with inorganic trace mineral elements which bind in such a way that they are easily utilized by various living organisms (de Melo et al. 2015).

2.4.2 Stability measurements of NPs

Accurate characterization of NPs at different stages is crucial in order to correlate properties of the NPs to their toxicity. The stability of NPs dispersions and their tendency to agglomerate can be due to steric, electrostatic and, van der Waals forces between particles using the Derjaguin-Landau-Verwey-Overbeek (DLVO) theory (Jingkun Jiang, Pratim Biswas, Gunter Oberdorster 2009; Bian et al. 2011). This theory accounts for two forces acting amongst particles, van der Waals Attraction (V_A) and electrostatic diffuse double-layer repulsions (V_R). The sum of these two forces will determine the overall interaction between particles be whether repulsive or attractive as per **equation 2.3**.

$$V_T = V_R + V_A \qquad \textbf{(2.3)}$$

$$V_R = \left[\frac{64 n_s k T G^2}{K}\right] e^{(-Kd)} \qquad \textbf{(2.4)}$$

Where:

$$G = \tanh\left(\frac{Ze\psi}{4kT}\right) \qquad \textbf{(2.4.1)}$$

$$n_S = N_A * c \qquad \textbf{(2.4.2)}$$

$$K = 2.32 * 10^9 \left(\sum c_i * z_i\right)^{1/2} \qquad \textbf{(2.4.3)}$$

$$V_A = \frac{-A_H}{12\pi d^2} \qquad \textbf{(2.5)}$$

where *k* is the Boltzmann constant, *T* is the absolute temperature, n_S is the number of molecules or ion pairs per volume which can be calculated with equation **(2.4.2)**, where *c* is ion molar concentration and N_A is the Avogadro’s number. The *G* parameter is computed per equation **(2.4.1)**, where *z* is the charge of the ions, ψ is the experimental zeta potential, and *e* is the electron charge. *K* is the inverse Debye length (K) which is calculated using equation **(2.4.3)**, where c_i is the ion molar concentration and z_i is the charge of the ion and A_H Hamaker constant in equation **2.5**. Equation **(2.4)** is only valid with Kd is much bigger than 1 (Stumm, Werner, and Morgan 2013; Romanello and Fidalgo de Cortalezzi 2013).

However, there are limitations to this theory in the sense that the actual measurements and the DLVO theory done in the presence of divalent ions seem to disagree to the failure of the diffuse double-layer theory at short distances from the surface. Furthermore, at distances below 5nm other forces like hydration, solvation and capillary effects might be operational (Stumm, Werner, and Morgan 2013). **Figure 2.7** summarises factors that pose challenges to the DLVO theory by modelling two solid spheres approaching each other in suspension. Furthermore, NPs challenges the limits of the DLVO theory mainly due to their small size, variable shapes, structures, composition and the potential presence of adsorbed or grafted organic macromolecules. Research has actually proven that this challenges when acting simultaneously will affect the behaviour of NPs in the environment (Hotze et al. 2010).

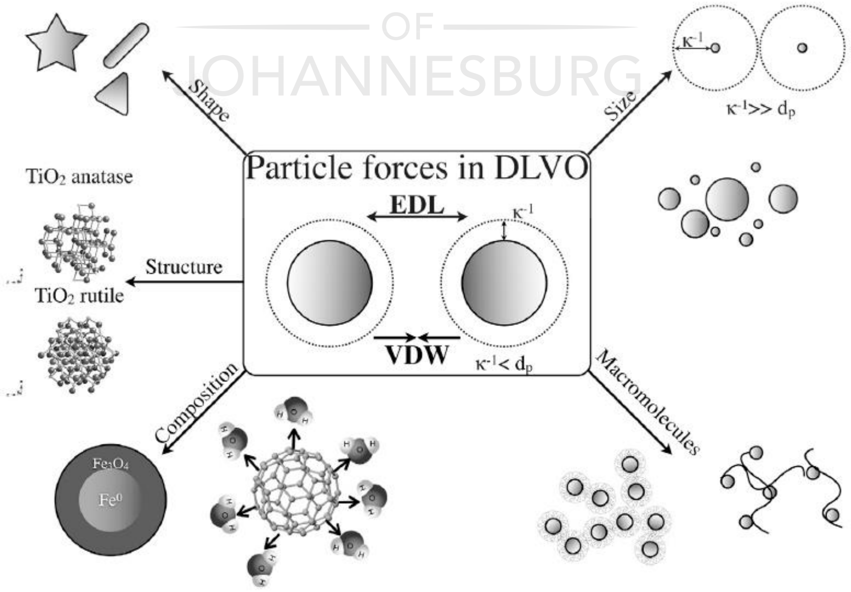

Figure 2.7: Factors Influencing two spheres in suspension under DLVO theory (Hotze et al. 2010)**.**

2.4.3 Possible reaction routes of NPs

When NPs interacts with organic or inorganic ligands, a chemical reaction such as redox, precipitation, adsorption, complexation, and photochemical reactions can take place on the surface of NPs**.** These reactions often result in morphological changes, and the likely formation of core–shell structures as illustrated in **Figure 2.8.** Metallic NPs are most likely to suffer redox reaction, for instance, Ag, Cu, and nZVI, and metal oxide NPs, such as iron oxides. The oxidation of Fe oxides such as magnetite may change the magnetic properties and, thus, the magnetic forces between particles, which influence the aggregation behaviour of the material thus decreasing the aggregation rates of magnetite NPs while enhancing their potential colloidal stability (Wagner et al. 2014)**.**

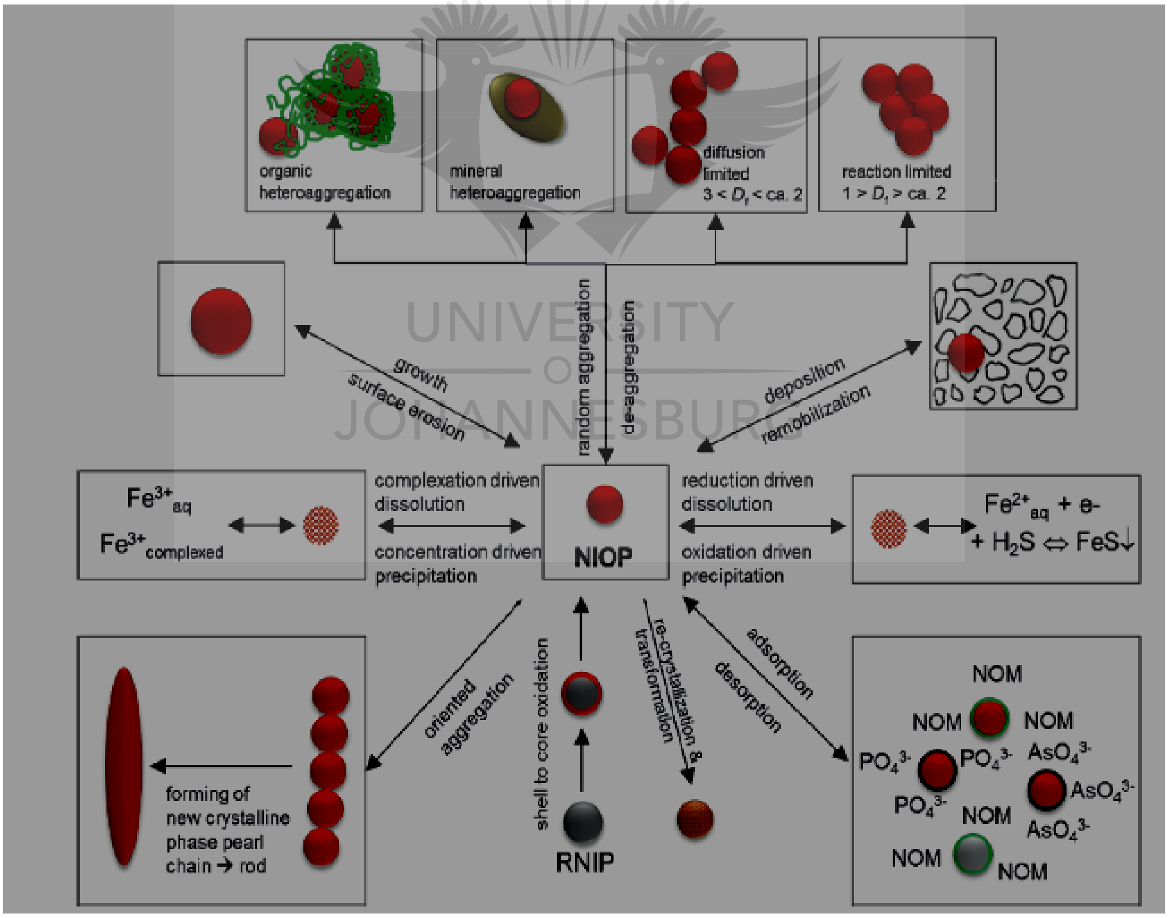

Figure 2.8: Possible reactions of nanoparticulate materials in natural aquatic media, with a nano iron oxide particle (NIOP) used as an example (Wagner et al. 2014)

Moreover, surface properties controlled by the solution chemistry mainly governs the formation and disaggregation of NPs aggregates which is an important surface-driven phenomenon encountered in the aquatic and terrestrial environments. Consequently, aggregation and/or disaggregation impact particle concentration, contaminant sorption/desorption reactions and contaminant and trace metal speciation, bioavailability and transport in aquatic and terrestrial environments (Baalousha 2009)**.**

Work done by Wagner et al. 2014, showed that incident light can induce photochemical reactions of NPs in surface environments. These may comprise the generation of free radicals, excitation of the photoactive material, and photodegradation. Carbon based NPs such as carbon nanotubes and fullerenes are oxidized under UV irradiation thus enhancing the production of reactive oxygen species, aiding in the degradation of organic contaminants. Ag NPs coated with polyvinylpyrrolidone, which is believed to bind strongly to NPs, are stable under irradiation with sunlight. NPs coated with gum arabic, which binds more weakly to NPs, aggregate through strong oscillating dipole–dipole interactions. Furthermore, the irradiation of NOM with sunlight can produce superoxide and hydrogen peroxide species that can reduce ionic silver to metallic silver nanoparticles or could potentially induce redox reactions on the particle surfaces, when NOM is sorbed on the particle.

2.5 Wastewater treatment plant (WWTP)

The South African water Act of 1956 declared that effluent be treated to acceptable standards before being returned to the original water (Morrison et al. 2001). Currently, the country has over 50 wastewater treatment plants distributed in eight (8) provinces (Chaúque 2014).

WWTP is defined as the engineered system used in the treatment of both domestic and industrial wastewater (Chong et al. 2010). On the other hand, wastewater is the combination of liquid and water-carried waste removed from the residence, commercial, industrial and institutional facilities with the addition of ground, storm and surface water disposed of into the sewage system. It constitutes mostly oxygen demanding waste, pathogens, organic matter, nutrients, and minerals and may contain some toxic compounds (Sonune & Ghate 2004). The composition of untreated domestic wastewater is summarized in **Table 2.5**. It is important to note though that these parameters can vary in different societies.

Table 2.5: Typical untreated raw wastewater profile (Metcalf & Eddy 2004).

Contaminants	**Unit**	**Concentration**		
		Low Strength	**Medium Strength**	**High Strength**
Total solids (TS)	mg/L	390	720	1230
Total dissolved solids (TDS)	mg/L	270	500	860
Fixed	mg/L	160	300	520
Volatile	mg/L	110	200	340
Total suspended solids (TSS)	mg/L	120	210	400
Fixed	mg/L	25	50	85
Volatile	mg/L	95	160	315
Settleable solids	mg/L	5	10	20
Biochemical oxygen demand, 5-d, 20ºC (BOD, 20ºC)	mg/L	110	190	35p
Total organic carbon (TOC)	mg/L	80	140	260
Chemical oxygen demand (COD)	mg/L	250	430	800
Nitrogen (total as N)	mg/L	20	40	70
Organic	mg/L	8	15	25
Free ammonia	mg/L	12	25	45
Nitrites	mg/L	0	0	0
Nitrates	mg/L	0	0	0
Phosphorus (total as P)	mg/L	4	7	12
Organic	mg/L	1	2	4
Inorganic	mg/L	3	5	8
Chlorides	mg/L	30	40	90
Sulphate	mg/L	20	30	50
Oil and grease	mg/L	50	90	100
Volatile organic compounds (VOCs)	µg/L	<100	100-400	>400
Total coliform	No./100 mL	10^{6}-10^{8}	10^{7}-10^{9}	10^{7}-10^{10}
Fecal coliform	No./100 mL	10^{3}-10^{5}	10^{4}-10^{6}	10^{5}-10^{8}
*Cryptosporidum*oocyts	No./100 mL	10^{-1}-10^{0}	10^{-1}-10^{1}	10^{-1}-10^{2}
Giardia lamblia cysts	No./100 mL	10^{-1}-10^{1}	10^{-1}-10^{2}	10^{-1}-10^{3}

Conventional wastewater treatment involves physical, mechanical, biological and chemical processes (Robert 2003). The different units and processes may be grouped together to form various treatment levels known as preliminary, primary, advanced primary and advanced (tertiary) treatment (Sonune & Ghate 2004; Metcalf & Eddy 2004). **Table 2.6** provides the descriptions on each of the treatment levels stated. The treatment technologies being used in this levels include adsorption, coagulation, sedimentation, filtration, chemical and membrane technology (Ghaly et al. 2014; Chong et al. 2010).

Table 2.6: Levels of wastewater treatment (Metcalf & Eddy 2004).

Treatment level	**Description**
Preliminary	Removal of wastewater constituents such as rags, sticks, floatables, grit, and grease that may cause maintenance or operational problems with the treatment operations, processes, and ancillary systems
Primary	Removal of a portion of the suspended solids and organic matter from the wastewater
Advanced primary	Enhanced removal of suspended solids and organic matter from the wastewater. Typically accomplished by chemical addition or filtration
Secondary	Removal of biodegradable organic matter (in solution or suspension) and suspended solids. Disinfection is also typically included in the definition of conventional secondary treatment
Secondary with nutrients removal	Removal of biodegradable organics, suspended solids, and nutrients (nitrogen, phosphorus, or both nitrogen and phosphorus)
Tertiary	Removal of residual suspended solids (after secondary treatment), usually by granular medium filtration or micro-screens. Disinfection is also typically a part of tertiary treatment. Nutrient removal is often included in this definition
Advanced	Removal of dissolved and suspended materials remaining after normal biological treatment when required for various water reuse applications

2.5.1 Operation of conventional WWTP

Biological WWTP is dependent on the presence and use of microorganisms to biodegrade contaminants from wastewater prior to discharge as treated effluent. Biological treatment can be divided into three (3) basic categories which are namely: aerobic, anaerobic and anoxic. The aerobic biological treatment is when microbes and oxygen come to contact with the wastewater in a reactor to optimise the growth and efficiency of biomass (Hero 2014).

The basic unit of operation of the activated sludge process is the floc. The floc is suspended in the aeration tank and consists of millions of aerobic micro-organisms (bacteria, fungi, yeast, protozoa, and worms), particles, coagulants and impurities that have come together and formed a mass. This mass is irregular in shape and helps to collect pollutants, both organic and inorganic, in the wastewater by adsorption, absorption or entrapment (Anon 1997). The treatment processes can be regrouped into primary, secondary and tertiary processes with the steps involved as shown in **Figure 2.9**. Microorganisms will biologically degrade organic contaminants and as soluble oxygen is constantly supplied. The wastewater and microorganisms are then separated through gravity in the secondary clarifier. The settled sludge is then returned back to the aeration basin while the clarified water is passed to the next vessel for further treatment (World Bank Water 2016; Ahansazan et al. 2014; Nazaroff n.d.).

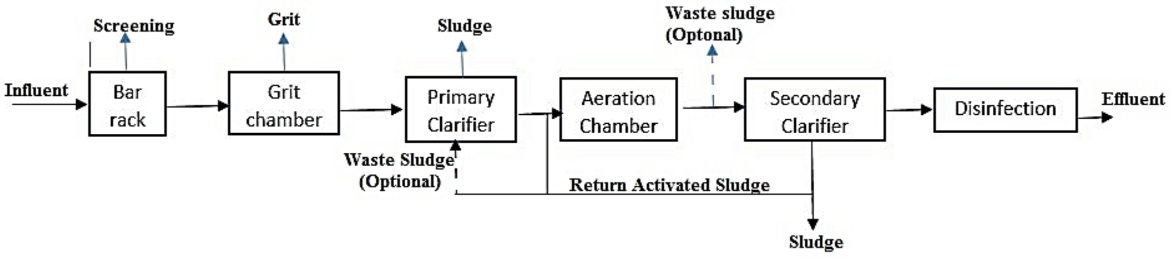

Figure 2.9: Typical flow diagram of an activated sludge process for wastewater treatment (Metcalf & Eddy 2004).

The main advantage of this process is the efficient removal of biological oxygen demand (BOD) and chemical oxygen demand (COD) (World Bank Water 2016). The biodegradable carbon is measured using as BOD which is a several days' measurement such as in 5, 7 and 10 days. However, the five-day biological oxygen demand (BOD_5) is the most commonly used due to time constraint and the necessity of the data during treatment monitoring BOD_5 is the measure of the amount of oxygen that the bacteria will consume over a five-day period while decomposing organic matter under aerobic conditions. BOD_5 sets a limitation for process monitoring due to delayed results availability thus there is now a move to replace BOD_5 as a measure of influent strength, with a short-term test (BOD_{ST}), which can be carried out over a timescale of 30 minutes to several hours (Davies 2005).

The main objective of the WWTP is to reduce the amount of BOD in the effluent before releasing to natural water. While COD is a measure of the total oxygen necessary to oxidize all organic materials into carbon dioxide and water. Both COD and BOD are the indications of pollution degree of water and are a comprehensive index of the relative content of organics (Northeast Georgia Regional Development centre, 2001). The values obtained for BOD_5 are always lower than those for COD since activated sludge bacteria cannot degrade some of the compounds oxidized chemically in the COD test. Some of the carbon removed during the BOD_5 test is not oxidized but ends up in new bacterial biomass. Therefore, the BOD_5 is only measuring the biodegradable carbon that is actually oxidized by the bacteria (Davies 2005).

The extent of oxidation can be affected by the digestion time, reagent strength and sample COD concentration as illustrated in equation **2.12** illustrate the general formula for determining COD. Organic matter if first oxidized using excess potassium dichromate and the excess later removed by titrating with ferrous ammonium sulphate (FAS) (Standard methods for the treatment of water and wastewater, 1999). The presence of chlorine ions in the sample may result in an increased consumption of dichromate as it will be oxidized during the process thus leading to an overestimate of COD values. Mercuric sulphate is then used as an inhibitor for this process due to its reaction with chlorine. The reactions taking place during the oxidation can be expressed by the following series of equations **2.6-2.11** (Environmental agency, 2007; Saral & Goncaloğlu 2008).

Oxidation reaction:

$$C_xH_yO_z + dCr_2O_7^{2-} + 2dH^+ \rightarrow xCO_2 + \frac{y+2d}{2}H_2O + 2dCr^{3+} \qquad \textbf{(2.6)}$$

Iron(II)/dichromate titration:

$6Fe^{2+} + Cr_2O_7^{2-} + 14H^+ \rightarrow 6Fe^{3+} + 2Cr^{3+} + 7H_2O$ **(2.7)**

Chloride interference reactions:

$Cr_2O_7^{2-} + 6Cl^- + 14H^+ \rightarrow 2Cr^{3+} + 3Cl_2 + 7H_2O$ **(2.8)**

$Hg^{2+} + 4Cl^- \rightarrow [HgCl_4]^{2-}$ **(2.9)**

$Cr^{3+} + 6Cl^- \rightarrow [CrCl_6]^{3-}$ **(2.10)**

$Ag^+ + Cl^- \rightarrow AgCl$ **(2.11)**

$$COD = \frac{(A\text{-}B)*M*8000}{mLSample} \qquad \textbf{(2.12)}$$

Where:

A = mL FAS used for blank,

B = mL FAS used for sample,

M = molarity of FAS, and

8000 = milliequivalent weight of oxygen × 1000 mL/L

2.5.1.1 Activated sludge performance characteristics

2.5.1.1.1 Food per microorganism ratio (F/M)

COD and BOD are used as the measure of organic matter available to the microbes and the volatile suspended solids as an indication of total microbes in the activated sludge (Robert 2003). The rate of biomass growth and the respiration rate increases with an increase in BOD loading. The increase in biomass corresponds to an increased removal of BOD. The F/M ratio can be calculated by dividing BOD with mixed liquor suspended solids (MLSS) following equation **2.13**:

$$\text{F/M}=\frac{\text{BOD (g/m}^3\text{)*Flow (m}^3\text{/d)}}{\text{MLSS (g/m}^3\text{)*Working volume (m}^3\text{)}} \qquad \textbf{(13)}$$

The F/M ratio increases with an increase of BOD removal, growth rate and respiration rate. The F/M values range from 0.5 - 1.0 however 0.2 - 0.5 is usually aimed for in a conventional treatment plant (Davies 2005).

2.5.1.1.2 Nutrients

The main substrate is carbon, however, nitrogen and phosphorus are also required for growth with the addition of the trace element such as sodium, iron, potassium and magnesium which are available in abundance in domestic wastewater (Robert 2003; Davies 2005). The optimum ratio of C:N:P in the mixed liquor is thought to be 100:5:1. The nutrient ratio has been reported to be 100:17:5 and 100:19:6 in settled domestic wastewater and it is close to the ideal values necessary for the growth of the activated sludge even though industrial wastewater can vary in combination. Wastewater from the brewing, pulp and paper industries is usually deficient in phosphorus and nitrogen thus a need to add in order to attain to the correct ratio necessary for microbial growth (Davies 2005; Ahansazan et al. 2014)

2.5.1.1.3 Temperature

The removal efficiency of BOD is increased up to 95% as the temperature increases from 0-30˚C (Robert 2003). This is evidence that temperature does affect the performance of a biological sludge system. At lower temperatures, there is reduced predation, increased solids production and poor flocculation (Wesley 2000; Robert 2003). The OECD guidelines stipulate a 20-25˚C working range (OECD 303A 2001)

2.5.1.1.4 pH

This indicates the how much acidity or alkalinity an aqueous medium is. The optimum wastewater pH ranges from 7-7.5 for activated sludge systems. Once the pH range is outside the range of 5-10 there may be interference with the biological processes. Moreover, there is a substantial effect on the removal of BOD between the pH range of 6-9 (Robert 2003; Anon 1997).

2.5.1.1.5 Mixed liquor suspended solids

Mixed liquor suspended solid is the concentration of suspended solids present in the aeration vessel during the activated sludge process which can either be raw or unsettled wastewater (Anon 1997). A significant amount of MLSS can sometimes be inorganic matter thus most engineers prefer deriving the weight of the organic matter in sludge. This is achieved by combusting the already dried solids at 500˚C to obtain volatile organic matter called the mixed liquor volatile solids. MLVSS approximates the total microorganism present in an activated sludge. For extended aeration, the value of MLSS ranges from 800 to 1500 mg/L. However, it can get up to about 8000 mg/L for low rated systems (Davies 2005). When MLSS is high, the system is prone to bulking and the system will become overloaded resulting in a decrease of dissolved oxygen thus treatment efficiency will also decrease (Ahansazan et al. 2014).

For MLSS determination, a well-mixed sample is filtered through a weighed standard glass fibre filter. The residue left on the filter is then dried at a temperature range of 103-105 ˚C to a constant weight. The increase in the filter weight represents the total suspended solids of the sample (Anon 2016).

2.5.1.1.6 Dissolved oxygen

The amount of oxygen present in the aeration vessel determine the respiration rate of the flocs and hence growth. When the DO concentration is above the 1.5-

2.0 mg/L range, it will not be limit the activity of bacteria flocs (Davies 2005). However, Low DO concentrations when prolonged can favour undesirable organisms such as the filamentous type of bacteria to grow. If the DO concentration rises too high, it can cause problems such as flock particles to float on the surface of the secondary clarifier. Therefore, it is crucial in maintaining proper levels of DO in the aeration chambers (Ahansazan et al. 2014).

2.7 Characterization Techniques

The detection and characterization of ENMs are not only important for the assessment of their potential risks but to guarantee an adequate and reliable labelling of food products containing ENMs (Gräf et al. 2014). To accomplish this, access to robust analytical methodologies is essential as not only the composition and concentration are to be determined but also the physical and chemical properties of the engineered nanoparticles as with their importance of measure, within the sample and the chemical characteristics of any capping/functional layer on the particle surface (Tiede et al. 2008). Properties to be considered during extensive characterization should include NP size, size distribution, shape, surface area, redox potential, purity and identity of contaminants, catalytic activity, and dissolution potential. The potential to generate reactive oxygen or nitrogen species, and agglomeration state (Weinberg, Galyean, and Leopold 2011). Such techniques should be sensitive enough to measure very low concentrations and be capable of minimizing sample disturbance to ensure that laboratory analysis reflects the unperturbed environmental state (Tiede et al. 2008).

A wide range of methods that can be used as a characterisation of NPs is available. Some of the techniques advantage and the information that can be derived from each technique is summarized in **Table 2.7**.

Table 2.7: Characterization techniques for NPs and their limitations (Louie, Tilton, and Lowry 2016; Gräf et al. 2014)

Method	**Properties /Information**	**Advantages**	**Disadvantages**	**Limitations**
Raman	Oxidation state, Structure, Sizing	Compatible with aqueous suspensions and wet NP samples.	Parameter effects	Surface enhancement is only for ENMs with strong localized surface plasm on resonance.
SEM	Sizing	High Resolution	High vacuum, Sample preparation contrasting charging effect.	Lower resolution than TEM.
TEM	Sizing, Shape, Visualization, Structure	High Resolution	Sample preparation, High vacuum, Contrasting.	Poor sensitivity to thin, low electron density organic coatings without staining.
UV/Vis Spectro-scopy	Concentration, some structure or size information can be derived.	*Insitu* measurements on liquid suspension.	Insensitive	Interference due to ENM aggregation.
DLS	Hydrodynamic layer thickness, Z-average	*Insitu* measurement, useful to follow aggregation process	Difficult to interpret results based on weighted sizes.	Reliance on subtraction of coated and uncoated particle sizes.
XPS	Sizing, Shape, Elemental composition, Oxidation state	Atomic composition of layer from 1-10 nm,	Possible sample damage	Detailed models required for accurate analysis of layer thickness on NPs

2.6.1 Powder X-ray diffraction spectroscopy (XRD)

Powder X-ray diffraction (XRD) is a popular analytical technique, which has been used for the analysis of both molecular and crystal structures, qualitative identification of various compounds, quantitative resolution of chemical species, measuring the degree of crystallinity, isomorphous substitutions, stacking faults, polymorphisms, phase transitions, particle sizes (Das et al. 2014; Kuzmin et al. 1998). The materials can be powders, single crystals, multilayer thin films, sheets, and fibres. In XRD, a monochromatic X-ray beam is focused on sample material to resolve structural information in the crystal lattice (Das et al. 2014). X-ray diffractometers can be classified into two groups:

(i) single crystal, usually applied for the determination of molecular structures mainly of new compounds and

(ii) the powder diffractometers usually applied for routine phase identification and quantification. The powder diffractometers can also be configured to enhance many applications including variable-temperature studies, texture and stress analysis, grazing incidence diffraction, and reflectometry (Chaúque 2014). If the incident X-rays of wavelength (λ) strike a crystal where all atoms are placed in a regular periodic array with interplanar spacing *d*, diffraction beam of sufficient intensity is detected only when the “Bragg law” is satisfied as per equation **2.14** (Jenkins 2000).

$$n\lambda = 2d\sin\theta \qquad \textbf{(2.14)}$$

Where n is called the order of reflection and is equal to the number of wavelengths in the path difference between diffracted X-rays from adjacent crystal planes as shown in **Figure 2.10**.

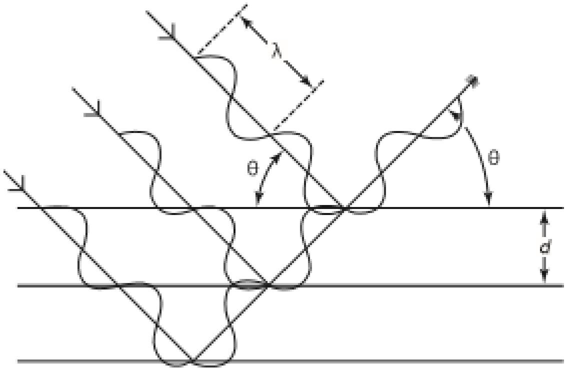

Figure 2.10: Scatter and diffraction from an ordered arrangement of atoms (Jenkins 2000).

The position of the peaks in an x-ray diffraction pattern is determined by the crystal geometry. The more symmetrical the material, the fewer the diffraction peaks. The intensities of these peaks I determined by the arrangement and the type of atoms within the crystal lattice. The radiation contains several wavelengths denoted Kα1, Kα2, and Kβ which are characteristic of the material producing the x-ray. The smaller the wavelength, the more energetic and penetrating the radiation (Formica 1997).

XRD can also be used to determine the nanocrystallite size in a nanocrystalline bulk materials, using the Scherrer equation, where the average crystalline size 'L' is:

$$L = \frac{K\lambda}{\beta \cos\theta} \qquad \textbf{(2.15)}$$

Where λ is the X-ray wavelength (nm), β is the peak width of the diffraction peak profile at half maximum height in radian and K is a constant related to crystalline shape (Monshi et al. 2012).

2.6.2 Transmission electron microscopy (TEM)

The transmission electron microscope is one of the most widely acclaimed instruments for measuring the dimensions of nanostructured objects in the nanometre and sub-nanometre ranges especially in the field of nanotechnology

(Zablotskii et al. 2013; Zhao & Yang 2010). This technique is mainly used for the determination of particle size and shape. TEM uses an electron beam which gets transmitted into an ultrathin specimen and interacts with the sample to form an image on a photographic plate or screen (Joshi et al. 2008). The use of electrons to illuminate the sample instead of light make TEM to have a higher resolution with a factor of about 1000 compare to light techniques (Lazar et al. 2012). The radiated electron beam consisting of uniform current density is focused into a plane of a thin specimen with the aid of magnetic lenses, some electrons penetrate and appear on the other side of the specimen (Tomlinson 2011) to form the image as it is magnified by the objective lens (Joshi et al. 2008) as illustrated in **Figure 2.11**. The image can be obtained by direct exposure of a photographic emulsion or an image plate inside a vacuum, or digitally via a fluorescent screen coupled by a fibre-optic plate to a charge-coupled device (CCD) camera (Reimer & Kohll 2008). This microscope depends on the transmission of the electron through the specimen so the specimen should be extremely thin (<150 nm thick). The electrons cannot pass through thick specimens since the interaction of electrons with the atoms and the local electrons inside the material is high (Abudayyeh 2012).

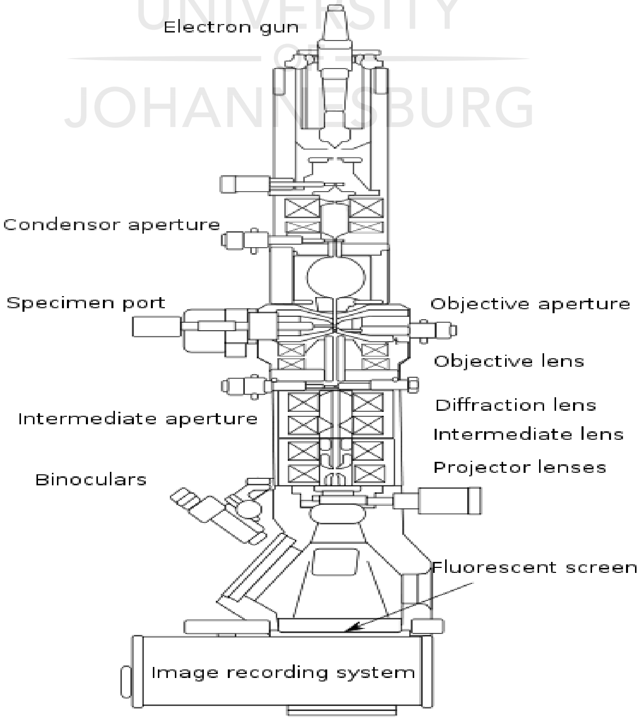

Figure 2.11: Schematic Diagram of TEM (Abudayyeh 2012).

There are essentially three types of lenses used to obtain the final image. These are condenser, objective, and projector lenses. The function of condenser lenses is to concentrate and focus the beam of electrons coming from the filament onto a sample to a uniformly illuminate it. The objective lens and its associated apertures are the heart of the TEM. These are used to form the initial enlarged image of the illuminated portion of the specimen in a plane that is suitable for further enlargement by the projector lens. When the electrons pass through the sample, some of them passes through the dense atoms and only a few are deflected. These scattered electrons generally make their way down in the column and contribute to the image. So, in order to eliminate these scattered electrons to form the image, an aperture is placed at the objective lens (Qadri 2014).

Transmission electron microscopy (TEM), coupled with energy dispersive spectroscopy (EDS), has been shown to be an effective, powerful tool for examining geochemical question on the individual particle scale. This technique is suited to provide information on the size, morphology, crystallinity, and elemental composition of single particles as well as on their physical and spatial associations (https://www-ssrl.slac.stanford.edu).

2.6.3 Scanning electron microscopy (SEM)

Scanning Electron Microscopy (SEM) is another technique other than TEM that is used for imaging the surface structure of semiconductors. SEM could also be used to identify the size of particles and examine the morphology of the surface, especially with samples which are reasonably thick. During imaging, SEM produces a high-energy electron beam that interacts with the surface of the sample which in turn emits secondary electrons. The emitted electrons are either backscattered and diffracted backscattered electrons, which are all captured by detectors and are transformed into a high depth of field image. This gives the image a 3-dimensional appearance despite being a two-dimensional image (Martin 2015).

During SEM analysis, the specimen in question should be conductive to enable the electron beam to scan the surface and provide a path for the electrons to ground for conventional imaging. For non-conductive specimen, they are commonly coated with a conductive material under low vacuum sputter coating or high vacuum evaporation. This is done to prevent the build-up of static electric charge on the specimen during the electron radiation process (Joshi et al. 2008)**.**

2.6.4 Raman spectroscopy

Raman spectroscopy is a characterization technique used to study vibrational, rotational, and other frequency modes in a system (Joshi et al. 2008). This technique relies on scatter light to gain information regarding molecular vibrations which in turn provides knowledge about the structure, symmetry, electronic environment and bonding of the molecule. When a molecule is exposed to light radiation, an inelastic and elastic scattering of light could possibly occur (Das & Agrawal 2011).

In elastic scattering, there is no change in the frequency of the photon while in inelastic scattering there is a shift in the photon frequency because of either excitation or deactivation of molecular vibrations leading to loss or gain energy by photons. There exist three types of phenomena as summarized in **Figure 2.12** by which interaction between light and molecules can occur (Joshi et al. 2008; Das & Agrawal 2011). The Raman spectra can be affected by high signal-to-noise ratio, instrument stability and sufficient resolution (Das & Agrawal 2011).

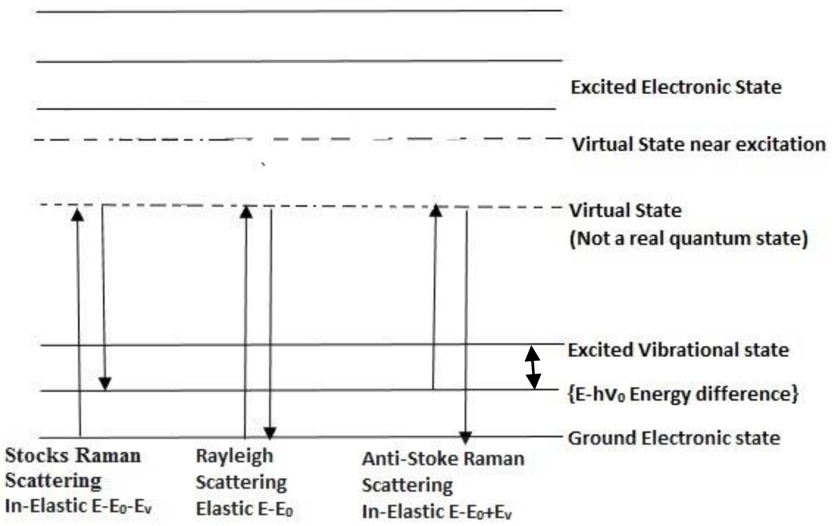

Figure 2.12: Mechanism of Raman scattering (Das & Agrawal 2011).

Both the Infrared and Raman spectroscopy provides information regarding the vibrations of molecules. The difference is in the origin of this techniques. IR involves absorption of electromagnetic radiation in the IR region while Raman is the scattering of electromagnetic radiation usually in the visible region (Warner & Butler 2003). Raman scattering is achieved by irradiating a sample with a light source at one specific wavelength. The monochromatic light source is usually in the form of a laser wavelength which cannot be absorbed by the matter. Light from the illuminated spot is collected with a lens and sent through a monochromator. Wavelengths close to the laser line, due to elastic Rayleigh scattering, are filtered out while the rest of the collected light is directed to a detector (Ferraro et al. 2003; Qadri 2014).

2.6.5 Fourier transform infrared spectroscopy (FTIR)

Infrared spectroscopy is often used for the detection and fingerprinting of covalent bonds which are useful characterisation technique and paramount in the analysis of impurities and contaminants on the surface of semiconductor photocatalysts. Photocatalysts are mainly crystalline with simple molecular structures, thus posing few IR-active bond yet organic contaminants or impurities are intrinsically more molecularly complex, resulting in ease of detection in IR spectroscopy (Martin 2015). Molecules are IR active when they possess change associated with the dipole moment (Haug et al. 2012).

FTIR is a more counter-intuitive technique, with a much faster sampling time and higher signal to noise ratio. During FTIR analysis, the polychromatic light source is illuminated on the source and the beam first passes through a Michelson interferometer, which is a beam splitting device resulting in a deliberate path length shift subsequently illuminating the detector after having hit the sample with a mixed interference beam of all wavelengths. Beam retardation is caused by a moving mirror within the interferometer, which has real units of length. Therefore, the detector produces an interferogram; a fixed set of retardation values and a corresponding set of intensities. The position and intensity of the absorption bands of a sample are exceptionally specific for a substance and can be used as a highly characteristic “fingerprint” for identification (Martin 2015; Haug et al. 2012).

2.6.6 Thermo-gravimetric analysis

Thermo Gravimetric Analysis is an essential technique in observing characteristic changes that a compound undergoes under varying temperature. It is of great importance when investigating phase changes and condensation reactions of polymers (Martin 2015).

Thermogravimetric Analysis (TGA) is a technique in which the mass of a substance is monitored as a function of temperature or time as the sample specimen is subjected to a controlled temperature program in a controlled atmosphere (Perkin Elmer 2010). TGA is used to monitor the mass of a solid or liquid with temperature, and with a high precision, measure mass difference due to evaporation or sublimation. This can then be plotted on a simple x-y curve; mass loss (as a percentage) versus temperature or time (Martin 2015).

According to Perkin Elmer (2010), a TGA constitutes of a sample pan supported in a precision balance residing in a furnace which is heated and cooled during the experiment. The mass of the sample is monitored during the experiment while a sample purge gas controls the sample environment. This gas may be inert or a reactive gas that flows over the sample and exits through an exhaust. The mass loss could due to either degradation and/or decomposition, vaporization of bulk liquids or liquids adsorbed by solids, sublimation, reduction of metal oxides to metals, desorption of gases while mass gain can be due to adsorption of gases as well as in reactions of solids with reactive gases such as oxygen, chlorine, and carbon monoxide (Vyazovkin 2016).

2.6.7 Diffuse reflectance spectroscopy in the UV-Vis-NIR region (DRS)

Optical spectroscopic investigation measurements of powders and solids are achieved by collecting the light reflected using DRS (Beale et al. n.d.). The light irradiated can be in the ultraviolet (UV), visible (Vis) and near infrared (NIR) region of the electromagnetic spectrum. During the irradiation process, electrons are transferred from low-energy to high energy atomic orbital or molecular orbital (Weckhuysen 2004). These transitions include transition metal ions d-d transition and ligand-to-metal or metal-to-ligand charge transfer transition and inorganic and organic molecules (mainly n-π* and π-π* transition). The DRS technique is based on the reflection of light by a powder sample which has an individual particle size in the range of 0.2-3 µm (Weckhuysen 2004). the ratio of the scattered light from the ideal non-absorbing reference sample is measured as a function of the wavelength λ. Scattered light from the sample is collected in an integrated sphere and detected. Diffuse reflection is best described by the radiation transfer equation **2.16**

$$\frac{-dI}{k\rho dS} = I - \frac{j}{k} \qquad \textbf{(2.16)}$$

Where (I) is the incident light intensity at a given wavelength, (dI/dS) the change of the intensity with the path length (dS), (ρ) density of the medium, (k) an attenuation coefficient corresponding with the total radiation loss due to absorption and scattering and (j) the scattering coefficient (Weckhuysen & Schoonheydt 1999). The reference material used during DRS studies can either MgO and $BaSO_4$ since they do not absorb radiation (Zanjanchi et al. 2006).

2.6.8 Dynamic light scattering analysis (DLS)

Particle size distribution and zeta potential measurements are of great importance in the study of colloidal chemistry. The determination of the size of the particle is mostly achieved by the use of the dynamic light scattering (DLS) principle (De Kanter et al. 2016). In this concept, the particles under study are kept in a suspension solution where they are in constant Brownian motion. Brownian motion is the random thermal diffusive motion of microscopic particles suspended in a liquid or gas (University of Florida, 2012). This motion is due to collisions with the surrounding liquid particles. Since particles are in a diffusive motion, smaller particles will move faster than larger particles. A monochromatic laser beam is then used to obtain the diffusion information of particles. The beam scattered by the particles will either undergo constructive or destructive interference relative to the particle position to each other (De Kanter et al. 2016). The decay of the autocorrelation of the measured intensity is correlated to the translational diffusion coefficient. The Stoke-Einstein equation is then used to calculate the hydrodynamic radius as shown in equation **2.17** (Clark et al. 1970; Kumari & Pathak 2014).

$$D_h = \frac{K_B T}{6\pi\eta D} \qquad \textbf{(2.17)}$$

Where, Dh is the hydrodynamic diameter, D is the translational diffusion coefficient, K_B is the Boltzmann's constant, T is the temperature and η the dynamic viscosity. The hydrodynamic radius depends on the initial size of the particle, its surface properties, electrolyte and the ionic strength of the solution (Clark et al. 1970).

2.6.9 Electrophoretic light scattering (ELS)

The zeta potential value obtained gives information relative to the stability of the colloids and the degree of repulsion that exists between adjacent particles of the same charge (De Kanter et al. 2016). Zeta potential is a potential at a notional boundary surrounding the electrical double layer within which the liquid moves together with particles (Luxbacher 2014). At the electrical double layer surrounding the particle, there are electrokinetic properties that are determined by an electrical charge distribution. When immersed in an electrolyte such as water, an ionic particle becomes surrounded by counter ions, with a charge opposite to that at the surface (Martin 2015).

A Colloid particle with a zeta potential of 0 mV (Isoelectric Point, IEP) will undergo rapid aggregation due to a decreased in electrostatic repulsion which and Van der Waals forces facilitate agglomeration while those with ~40 mV will exhibit good stability, and ≥60 mV exhibits excellent stability. Therefore, the increase in electrostatic repulsion constraints agglomeration and settling, a suspension of particles showing a high absolute value of zeta potential is more stable in comparison to suspensions exhibiting lower zeta potential absolute values (Hanaor et al. 2012; Martin 2015).

The zeta potential is determined by the measurement of an electrokinetic effect, observed when a solid and a liquid phase moves relatively to each other achieved using micro-electrophoresis in conjunction with electrophoretic light scattering. The particle-electrolyte colloid is placed in a specialised cuvette-type cell, an oscillating electric field is then applied, which causes the particles to move with a velocity proportional to their zeta potential. In order to measure this velocity, a laser beam is passed through the cell, and the Doppler shift frequency observed is proportional to the dispersed particle's mobility (Martin 2015). Once the electrophoretic mobility is determined by electrophoretic light scattering. The obtained EPMs can then be converted to zeta potential using Smoluchowski equation **(2.18)** (Lin et al. 2009; X. Zhu et al. 2014).

$$\mu = \frac{\varepsilon\zeta}{\eta} \qquad \textbf{(2.18)}$$

Where μ is the electrophoretic mobility, ε is the dielectric constant of the solution, η, ζ is the viscosity and the zeta potential respectively.

2.6.10 Surface area, pore size and pore volume determination

Gas adsorption measurements are widely used for determining the surface area, pore size and pore volume distribution in a solid material. This could be achieved by using the Brauner-Emmett-Teller (BET) theory regarded as the standard method for surface area measurements (Sing 2004; Sing 2001). The BET theory describes the physisorption of the gas molecules on a solid surface which results from the weak van der Waals forces. This theory was adapted from the Langmuir theory which describes the monolayer adsorption of a gas on a solid by simply extending the concept to allow multilayer adsorption calculated using equation **2.19** (Martin 2015).

$$\frac{1}{v_a\left[\left(P^0 \div P\right)-1\right]} = \frac{(c-1)}{v_m c}\left(\frac{p}{p^0}\right) + \frac{1}{v_m c} \qquad \textbf{(2.19)}$$

where v_a = volume of gas adsorbed at standard temperature and pressure (STP), p and p^0 = the partial vapour pressure and saturation pressure of the physisorbed gas (often N_2), c = BET constant and v_m = adsorbed gas quantity per volume to produce a monolayer.

The BET constant (c) is described by equation **2.19.1**;

$$c = e^{\frac{(E_1 - E_L)}{RT}} \qquad \textbf{(2.19.1)}$$

where E_1 = first layer's heat of adsorption and E_L = corresponding heat of adsorption for n layers > 1.

The BET specific surface area (S_{BET}) is then given by equation **(2.20);**

$$S_{BET} = a\left(\frac{v_m N_A s}{V}\right) \qquad \textbf{(2.20)}$$

where a = mass of the powdered adsorbent, N_A = Avogadro's number, S = adsorption cross section of the powder and V = molar volume gas (Martin 2015).

2.6.11 Inductively coupled plasma optical emission spectroscopy (ICP-OES)

Trace elements in both biological and environmental samples are determined by using ICP-OES is a technique used widely for the determination of trace elements in both biological and environmental samples due to its unique advantages; multi-elemental capability, wide linear dynamic range, high sensitivity and high sample-through put.(Wu et al. 2014; Yilmaz et al. 2014) The technique is founded upon the spontaneous emission of photons from atoms and ions that have been excited in a radio frequency discharge. Liquid and gas samples may be injected directly into the instrument, while solid samples require extraction or acid digestion so that the analytes will be present in a solution. The sample solution is converted to an aerosol and directed into the central channel of the plasma (Xiandeng & Jones 2000).

At its core the inductively coupled plasma (ICP) sustains a temperature of approximately 10,000K, thus evaporating the aerosol as soon as possible. Analyte elements are liberated as free atoms in the gaseous state. Furthermore, collisional excitation within the plasma imparts additional energy to the atoms, promoting them to excited states. When enough energy is available, the atoms are converted to ions and promote the ions to excited states. Both the atomic and ionic excited state species may then relax to the ground state via the emission of a photon. These photons have characteristic energies that are determined by the quantized energy level structure of the atoms or ions. Thus, the wavelength of the photons can be used to identify the elements from which they originated. The total number of photons is directly proportional to the concentration of the originating element in the sample (Xiandeng & Jones 2000).

2.7 References

Abazari, R. & Sanati, S., 2013. Room temperature synthesis of tungsten (VI) trioxide nanoparticles with one-pot multi-component reaction in emulsion nanoreactors stabilized by aerosol-OT. *Materials Letters*, 107, pp.329–332.

Abudayyeh, H.A., 2012. *Synthesis and analysis of ZnO nanowires*. Birzeit University. Available, @ https://www.researchgate.net/publication/263849645_Synthesis_and_Analysis_of_ZnO_Nanowires. Accessed 26 April 2016.

Acarbas, O., Suvacı, E. & Dogan, A., 2007. Preparation of nanosized tin oxide (SnO_2) powder by homogeneous precipitation. *Ceramics International*, 33, pp.537–542.

Ahansazan, B., Afrashteh, H., Ahansazan, N., & Ahansazan, Z., 2014. Activated Sludge Process Overview. *International Journal of Environmental Science and Development*, 5(1), pp.81–85.

Ali Fakhria & Behrouzc, S., 2015. Photocatalytic properties of tungsten trioxide (WO3) nanoparticles for degradation of Lidocaine under visible and sunlight irradiation. *Solar Energy*, 112, pp.163–168.

Anik, M., 2006. Effect of concentration gradient on the anodic behaviour of tungsten. *Corrosion Science*, 48(12), pp.4158–4173.

Anik, M., 2009. pH-dependent anodic reaction behaviour of tungsten in acidic phosphate solutions. *Electrochimica Acta*, 54(15), pp.3943–3951.

Anik, M. & Cansizoglu, T., 2006. Dissolution kinetics of WO_3 in acidic solutions. *Journal of Applied Electrochemistry*, 36, pp.603–608.

Anon, 2016. Mixed Liquor Volatile Suspended Solids (MLVSS) & (MLSS). *Wastewater Training and Consulting*.pages? is it a book

Aoki, N.Sato, A., Sasaki, H.,Litwinowicz, A., & Adschiri, T., 2016. Kinetics study to identify reaction-controlled conditions for supercritical hydrothermal nanoparticle synthesis with flow-type reactors. *The Journal of Supercritical Fluids*, 110, pp.161–166.

Arutanti, O., Ogi, T.,Nandiyanto, A., Iskandar, F.& Okuyama, K., 2014. Controllable Crystallite and Particle Sizes of WO 3 Particles Prepared by a Spray-Pyrolysis Method and Their Photocatalytic Activity. *Inorganic Materials: Synthesis and Processing*, 60(1), pp.41–49.

Baalousha, M., 2009. Aggregation and disaggregation of iron oxide nanoparticles: Influence of particle concentration, pH and natural organic matter. *Science of the Total Environment*, 407(6), pp.2093–2101.

Bai, S.,Liu, H., Sun, J., Tian, Y., Chen, S., Song, J., Luo, R, Li, D., Chen, A., & Liu, C., 2015. Improvement of TiO_2 photocatalytic properties under visible light by WO_3/TiO_2 and MoO_3/TiO_2 composites. *Applied Surface Science*, 338, pp.61–68.

Baserga, A.,Russo, V., Di Fonzo, F., Bailini, A., Cattaneo, D., Casari, C. S., Li Bassi, A., & Bottani, C., E., 2007. Nanostructured tungsten oxide with controlled properties: Synthesis and Raman characterization. *Thin Solid Films*, 515, pp.6465–6469.

Beale, A.M., Stavitski, E. & Weckhuysen, B.M., Characterization of Catalysts: Surface an In-situ methods. Encyclopedia of Life Support Systems @ https://www.eolss.net/Sample-Chapters/C06/E6-190-13-00.pdf. Accessed 13 March 2016.

Belen, M., Fidalgo, M.M. & Cortalezzi, D., 2013. An experimental study on the aggregation of TiO_2 nanoparticles under environmentally relevant conditions. *Water Research*, 47(12), pp.3887–3898.

Bian, S.W., Mudunkotuwa, I. A., Rupasinghe, T., & Grassian, V. H., 2011. Aggregation and dissolution of 4 nm ZnO nanoparticles in aqueous environments: Influence of pH, ionic strength, size, and adsorption of humic acid. *Langmuir*, 27(10), pp.6059–6068.

Brinker, C.J. & Scherer, G.W., 1990. *Sol-Gel Science:* The physics and chemistry of sol-gel processing, London: Academic Press, Inc.

Cai, L., Xiong, X., Liang, N., & Long, Q., 2015. Highly effective and stable Ag_3/PO_4-WO_3/MWCNTs photocatalysts for simultaneous Cr(VI) reduction and orange II degradation under visible light irradiation. *Applied Surface Science*, 353, pp.939–948.

Chaúque, E.F., 2014. Monitoring of Physiochemical Parameters and the Behaviour of Zinc Oxide Nanoparticles in a Simulated Wastewater Treatment Plant. M.Sc. The university of Johannesburg @ https://ujdigispace.uj.ac.za/handle/10210/11321. Accessed 26 February 2016.

Chen, Q.,Li, J., Li, X., Huang, K., Zhou, B., Cai, W., & Shangguan, W., 2012. Visible-Light Responsive Photocatalytic Fuel Cell Based on WO_3/W Photoanode and Cu_2O/Cu Photocathode for Simultaneous Wastewater Treatment and Electricity Generation. *Environmental Science and Technology*, 46, pp.11451–11458.

Chen, S., Hu, Y., Jiang, X., Meng, S., & Fu, X., 2015. Fabrication and characterization of novel Z-scheme photocatalyst WO_3/g-C_3N_4 with high ef fi cient visible light photocatalytic activity. *Materials Chemistry and Physics*, 149–150, pp.512–521.

Chen, X., Zhou, Y., Liu, Q., Li, Z., Liu, J, & Zou, Z., 2012. Ultrathin, single-crystal WO_3 nanosheets by two-dimensional oriented attachment toward enhanced photocatalystic reduction of CO_2 into hydrocarbon fuels under visible light. *ACS Applied Materials and Interfaces*, 4(7), pp.3372–3377.

Clark,A, N., H. Lunacek, J. & B. Benedek, G., 1970. A Study of Brownian Motion Using Light Scattering. *American Journal of Physics*, 38, pp.575–585.

Chong, M.N., Jin, B., Chow, C., W K., & Saint, C., 2010. Recent developments in photocatalytic water treatment technology: A review. *Water Research*, 44(10), pp.2997–3027.

Cole, B., Marsen, B. & Miller, E., 2006. Influence of Nitrogen Doping on Tungsten Oxide Thin Films for Photoelectrochemical Water Splitting. *MRS Proceedings*, 974. doi:10.1557/PROC-0974-CC09-04.

Danks, A.E., Hall, S.R. & Schnepp, Z., 2016. The evolution of “sol-gel” chemistry as a technique for material synthesis. *Materials Horizons, 3, pp.91-112.*

Das, R., Ali, E., Bee, S., & Hamid, A., 2014. Current Appplication of X-ray Powder Diffraction- A Review. *Rev.V Adv. Mater. Sci.*, 38, pp.95–109.

Das, R.S. & Agrawal, Y.K., 2011. Vibrational Spectroscopy Raman spectroscopy : Recent advancements, techniques and applications. *Vibrational Spectroscopy*, 57(2), pp.163–176.

Davies, P.S., 2005. *The Biological Basis of Wastewater Treatment*. *Strathkelvin Instruments Ltd* @ http://www.strathkelvin.com. Accessed 04 May 2016.

De Kanter, M., Meyer-Kirschner, J., Viell, J., Mitsos, A., Kather, M., Pich, A., & Janzen, C., 2016. Enabling the measurement of particle sizes in stirred colloidal suspensions by embedding dynamic light scattering into an automated probe head. *Measurement*, 80, pp.92–98. Available at: http://dx.doi.org/10.1016/j.

Di Valentin, C., Wang, F. & Pacchioni, G., 2013. Tungsten Oxide in Catalysis and Photocatalysis: Hints from DFT. *Topics in Catalysis*, 56(15–17), pp.1404–1419.

Dimitriev, Y., Iordanova, R., Mancheva, M., & Klissurski, D., 2005. Preparation of Nanocrystalline WO_3 and MoO_3 by Different Sol-Gel Methods. Available @ http://www.sibran.ru/upload/iblock/3f6/3f6ab19e40ad21e6343e883cd9544d15.pdf , pp.185–189. Accessed 24 March 2016.

Dwivedi, A.D., Shashi P. D., Mika Si., Young N. K., Changha L., & Rajender S. V., 2015. Fate of engineered nanoparticles: Implications in the environment. *Coordination Chemistry Reviews*, 287, pp.64–78.

Environmental Agency, 2007. *The determination of chemical oxygen demand in waters and effluents*, @ https://www.gov.uk/government/uploads/system/uploads/attachment_data/file/316793/COD-215nov.pdf. Accessed 23 May 2016.

Environmental Protection Agency, 1997. *Wastewater Treatment Manual: Primary, Secondary and Tertiary Treatment*, Wexford, Ireland. pp 13-24.

Ferraro, J.R., Nakamoto, K. & Brown, C.W., 2003. *Introductory Raman*

Spectroscopy Second edition. Academic Press. pp 1-94.

French, R.A., Astrid R. J., Bojeong K., Sara L. I., Lee P., & Philippe C. B., 2009. Influence of ionic strength, pH, and cation valence on aggregation kinetics of titanium dioxide nanoparticles. *Environmental Science and Technology*, 43(5), pp.1354–1359.

Galyean, A., Howard S. W.,Holbrook, D. H., & Michael L., 2012. *Characterization of Engineered Nanoparticles in Natural Waters*. *Analysis and Risk of Nanomaterials in Environmental and Food Samples, 59, pp.169-195*

Ghaffarian, H.R., Saiedi, M. & Sayyadnejad, M. Al, 2011. Synthesis of ZnO Nanoparticles by Spray Pyrolysis Method. *Iran. J. Chem. Chem. Eng.*, 30(1), pp.1–6.

Ghaly, A.E., Ananthashankar, R., Alhattab, M., & Ramakrishnan, V. V., 2014. Production , Characterization and Treatment of Textile Effluents : A Critical Review. *Chemical Engineering & Process Technology*, 5(1), pp.1–19.

Gomez, C., Martínez, D.S. & Torres-martínez, L.M., 2013. Facile synthesis of -WO_3 powders via precipitation in ethanol solution and evaluation of their photocatalytic activities. *Journal of Photochemistry and Photobiology A: Chemistry*, 262, pp.28–33.

Hai-Ning Cui, 2011. *Preparation and characterization of optical multilayered coatings for smart windows application* @ http://www.repositorium.sdum.uminho.pt/bitstream/1822/3341/5/Chapter7-WO_3.pdf. Accessed 25 January 2017.

Hameed, A., Gondal, M.A. & Yamani, Z.H., 2004. Effect of transition metal doping on photocatalytic activity of WO_3 for water splitting under laser illumination : role of 3d-orbitals. *Catalysis Communications*, 5, pp.715–719.

Hanaor, D., Michelazzi, M., Leonelli, C.,& Sorrell, C. C., 2012. The effects of carboxylic acids on the aqueous dispersion and electrophoretic deposition of ZrO_2. *Journal of the European Ceramic Society*, 32(1), pp.235–244.

Hussainova, I., 2014, *Techniques for synthesis of nanomaterials* @

https://www.ttu.ee/public/m/Mehaanikateaduskond/Instituudid/Materjalitehnika_instituut/MTX9100/Lecture11_Synthesis.pdf. Accessed 22 April 2016.

Haug, A., Hiesgen, R., Schulze, M., & Friedrich, K A., 2012. Fourier Transform Infrared Spectroscopy. In *PEM Fuel Cell Diagnostic Tools*. London: Taylor & Francis Group, LLC, pp. 369–378.

Hayashi, H. & Hakuta, Y., 2010. Hydrothermal Synthesis of metal oxide nanoparticles in supercritical water. *Materials*, 3(7), pp.3794–3817.

Hero, N., 2014. *Wastewater Treatment in Harbours*. Institute of Superior Technico, Lisbon @ https://fenix.tecnico.ulisboa.pt/downloadFile/395146463089/Final%20thesis-Neva%20Hero.pdf. Accessed 24 March 2016.

Hotze, E.M., Phenrat, T. & Lowry, G. V, 2010. Nanoparticle aggregation: challenges to understanding transport and reactivity in the environment. *Journal of Environmental Quality*, 39, pp.1909–1924.

Jan, Š., Václav, S., Snejana B., & Lorant S., 2006. Synthesis of spherical metal oxide particles using homogeneous precipitation of aqueous solutions of metal sulfates with urea. *Powder Technology*, 169, pp.33–40.

Jenkins, R., 2000. X-ray Techniques : Overview. *Encyclopedia of Analytical Chemistry*, pp.13269–13288.

Jingkun J., Pratim B., Oberdorster, G., 2009. Characterization of size , surface charge , and agglomeration state of nanoparticle dispersions for toxicological studies. *J Nanopart Res*, 11, pp.77–89.

Joshi, M., Bhattacharyya, A. & Ali, S.W., 2008. Characterization techniques for nanotechnology applications in textiles. *Indian Journal of fibre and textile Research*, 33, pp.304–317.

Kant, R., Kumar, D. & Ghose, R., 2016. Synthesis of nanocrystalline ZnO – NiO mixed metal oxide powder by homogeneous precipitation method. *Ceramics International*, 42(3), pp.4090–4098.

Khanjani, S. & Morsali, A., 2010. Synthesis and characterization of lanthanum oxide nanoparticles from thermolysis of nanostructured supramolecular compound. *Journal of Molecular Liquids*, 153(2–3), pp.129–132.

Kostis, I., Vasilopoulou, M., Soultati, A., Argitis, P., Konofaos, N., Douvas, A. M., Vourdas, N., Papadimitropoulos, G., & Davazoglou, D., 2013. Highly porous tungsten oxides for electrochromic applications. *Microelectronic Engineering*, 111, pp.149–153.

Koutsospyros, A., Braida, W., Christodoulatos, C., Dermatas, D., & Strigul, N., 2006. A review of tungsten: From environmental obscurity to scrutiny. *Journal of Hazardous Materials*, 136, pp.1–19.

Kumar, V.B. & Mohanta, D., 2011. Formation of nanoscale tungsten oxide structures and colouration characteristics. *Bulletin of Materials Science*, 34(3), pp.435–442.

Kumari, N. & Pathak, P.N., 2014. Dynamic light scattering studies on the aggregation behaviour of tributyl phosphate and straight chain dialkyl amides during thorium extraction. *Journal of Industrial and Engineering Chemistry*, 20(4), pp.1382–1387.

Kuzmin, A., Purans, J., Cazzanelli, E., Vinegoni, C., & Mariotto, G., 1998. X-ray Diffraction , Extended X-ray Absorption Fine Structure and Raman Spectroscopic Studies of WO_3 Powders and (1-x) $WO_{3-y}xReO_2$ Mixtures. *Journal of Applied Physics*, 84(10), pp.5515–5524.

Kwong, W.L., Nakaruk, A., Koshy, P., &. Sorrell, C. C., 2013. Photoelectrochemical properties of WO_3 nanoparticulate thin films prepared by carboxylic acid-assisted electrodeposition. *Thin Solid Films*, 544, pp.191–196.

Lam, S.M., Jin C. S., Ahmad Z. A., & Abdul R. M., 2015. Sunlight responsive WO_3/ZnO nanorods for photocatalytic degradation and mineralization of chlorinated phenoxyacetic acid herbicides in water. *Journal of Colloid and Interface Science*, 450, pp.34–44.

Lazar, S, Botton, G A., Wu, M., Tichelaar, F D., Zandbergen, H W., 2012.

Transmission Electron Microscopy Analysis of NAnoparticles. *nanoComposix*, http://50.87.149.212/sites/default/files/nanoComposix Guidelines for TEM Analysis.pdf. Accessed 04 February 2017.

Lee, S.D., Sang-Hun N., Myoung-Hwa K., & Jin-Hyo B., 2012. Synthesis and Photocatalytic Property of ZnO nanoparticles Prepared by Spray-Pyrolysis Method. *Physics Procedia*, 32, pp.320–326.

Li, J. et al., 2010. Synthesis of monoclinic WO_3 nanosphere hydrogen gasochromic film via a sol-gel approach using PS-b-PAA diblock copolymer as template. *Solid State Sciences*, 12(8), pp.1393–1398.

Lin, D., Liu, N., Yang, K., Zhu, L., Xu, Y., & Xing, B., 2009. The effect of ionic strength and pH on the stability of tannic acid-facilitated carbon nanotube suspensions. *Carbon*, 47, pp.2875–2882.

Liu, H. Tianyou P., Dingning K., Zhenghe P., & Chunhua Y., 2007. Preparation and photocatalytic activity of dysprosium doped tungsten trioxide nanoparticles. *Materials Chemistry and Physics*, 104(2–3), pp.377–383.

Louie, S.M., Tilton, R.D. & Lowry, G. V., 2016. Critical Review: Impacts of Macromolecular Coatings on Critical Physicochemical Processes Controlling Environmental Fate of Nanomaterials. *Environ. Sci.: Nano*.

Luévano-hipólito, E., Martínez-de C. A., Yu, Q. L., & Brouwers, H. J. Hl., 2014. Precipitation synthesis of WO_3 for NO_x removal using PEG as template. *Ceramics International*, 40, pp.12123–12128.

Luxbacher, T., 2014. *The Zeta Potential for Solid Surface Analysis: A practical guide to streaming potential measurement* 1 st., Austria: Anton Paar GmbH.

Luyts, K. Napierska, D., Nemery, B., & Hoet, P. M. H., 2013. How physico-chemical characteristics of nanoparticles cause their toxicity: complex and unresolved interrelations. *Environmental Science-Processes & Impacts*, 15(1), pp.23–38.

Martin, D.J., 2015. *Investigation into High Efficiency Visible Light Photocatalysts for Water Reduction and Oxidation*, London: Spriger Internation Publishing.

Martínez, D.S., Cruz, A.M. & Cuéllar, E.L., 2011. Photocatalytic properties of WO_3 nanoparticles obtained by precipitation in presence of urea as complexing agent. *Applied Catalysis A: General*, 398, pp.179–186.

de Melo, B.A.G., Motta, F.L. & Santana, M.H.A., 2015. Humic acids: Structural properties and multiple functionalities for novel technological developments. *Materials Science and Engineering C*, 62, pp.967–974.

Metcalf & Eddy, 2004. Wastewater Engineering Treatment and Reuse. *New York. McGraw-Hill Companies, Inc*, (4 edition).

Monshi, A., Foroughi, M.R. & Monshi, M.R., 2012. Modified Scherrer Equation to Estimate More Accurately Nano-Crystallite Size Using XRD. *World Journal of Nano Science and Engineering*, 2(September), pp.154–160.

Morrison, G. Fatoki, O. S., Persson, L., & Ekberg, A., 2001. Assessment of the impact of point source pollution from the Keiskammahoek Sewage Treatment Plant on the Keiskamma River - pH, electrical conductivity, oxygen-demanding substance (COD) and nutrients. *Water SA*, 27(4), pp.475–480.

Mu, W., Xiang X., Xingliang L., Rui Z., Qianhong Y., Kai L., Hongyuan W., & Yuan J., 2015. Solid-state synthesis of hexagonal tungsten trioxide nanorods. *Materials Letters*, 138, pp.107–109.

Nazaroff, A.C., Wastewater Treatment Plant (WWTP) – System Overview primary treatment secondary treatment Primary. , pp.1–22. @ http://www.hanovernh.org.pages/hanoverNH_publicworks/waterrecl/Index. Accessed 21 April 2016.

Nogueira, H.I.S., Cavaleiro, A.M. V & Trindade, T., 2004. Synthesis and characterization of tungsten trioxide powders prepared from tungstic acids. *Materials Research Bulletin*, 39, pp.683–693.

Northeast Georgia Regional Development centre, 2001. Watershed Protection Plan Development Guidebook. , pp.1–11.

Oberdörster, G. Andrew M., Ken D., Vincent C., Julie F., Kevin A., & Janet C., 2005. Principles for characterizing the potential human health effects from exposure to nanomaterials : elements of a screening strategy. *Particle and Fibre Toxicology*, 35(2:B), pp.1–35.

Organization for Economic Co-operation and Development 303A, 2001. Aerobic Sewage Treatment – activated sludge units. Guidelines for the testing of chemicals. @ http://www.oecd.org/chemicalsafety/testing/34898616.pdf. Accessed 15 April 2016.

Okuyama, K. & Lenggoro, W.W., 2003. Preparation of nanoparticles via spray route. *Chemical Engineering Science*, 58(3–6), pp.537–547.

Ostachaviciute, S., Baltrušaitis, J. & Valatka, E., 2010. Photoactive WO_3 and Se-WO3 thin films for photoelectrochemical oxidation of organic compounds. *Journal of Applied Electrochemistry*, 40(7), pp.1337–1347.

Perkin Elmer, 2010. *Thermogravimetric Analysis (TGA) A Beginner ' s Guide*, @ www.perkinelmer.com/CMSResources/Images/44-74556GDE_TGABeginnersGuide.pdf. Accessed 14 February 2017.

Qadri, M.U., 2014. *Tungsten oxide nanostructures and thin films for optical gas sensors*. UNIVERSITAT ROVIRA I VIRGILI. Available @ http://www.tesisenred.net/bitstream/handle/10803/279291/Thesis.pdf?sequence=2. Accessed 28 October 2016.

Ranville, Manuel D. Montaño & James, G.V.L., 2014. *Detection and Characterization of Engineered Nanomaterials in the Environment : Current State-of-the-Art and Future Directions*, United State Environmental Protection Agency, pp. 1-186

Reimer, L. & Kohll, H., 2008. *Transmission Electron Microscopy: Physics of Image Formation* Firth Edit., New York: Springer Science.

Robert E. Pettit, Organic mater, Humus, Humate, Humic acid, Fulvic acid and Humin: Their importance in soil fertility and plant health. @ http://www.humates.com/pdf/ORGANICMATTERPettit.pdf Accessed March 15, 2017.

Romanello, M.B. & Fidalgo de Cortalezzi, M.M., 2013. An experimental study on the aggregation of TiO_2 nanoparticles under environmentally relevant conditions. *Water Research*, 47(12), pp.3887–3898.

Sa, D. & Lo, E., 2010. Synthesis and characterization of WO_3 nanoparticles prepared by the precipitation method: Evaluation of photocatalytic activity under vis-irradiation. *Solid State Sciences*, 12, pp.88–94.

Sanchez-Martı´nez, D., Cruz, A.M. la & Llar, E.L.-C., 2013. Synthesis of WO_3 nanoparticles by citric acid-assisted precipitation and evaluation of their photocatalytic properties. *Material Research Bulletin*, 48, pp.691–697.

Saral, A. & Goncaloğlu, B.I., 2008. Determination of real COD in highly chlorinated wastewaters. *Clean*, 36(12), pp.996–1000.

Saravanan, P., Gopalan, R. & Chandrasekaran, V., 2008. Synthesis and characterisation of nanomaterials. *Defence Science Journal*, 58(4), pp.504–516.

Shah, M. & Muzyyan, N., 2009. A Novel Approach for the Synthesis of Tungsten Trioxide Nanostructures. *Journal of King Abdulaziz University-Science*, 21(1), pp.109–115.

Simchi, H. et al., 2014. Structural, optical, and surface properties of WO_3 thin films for solar cells. *Journal of Alloys and Compounds*, 617, pp.609–615.

Simonsen, M.E. & Søgaard, E.G., 2010. Sol – gel reactions of titanium alkoxides and water: influence of pH and alkoxy group on cluster formation and properties of the resulting products. *J Sol-Gel Sci Technol*, 53, pp.485–497.

Sing, K., 2001. The use of nitrogen adsorption for the characterisation of porous materials. *Colloids and Surfaces A: Physicochemical and Engineering Aspects*, 187–188, pp.3–9.

Sing, K.S.W., 2004. Characterization of porous materials: Past, present and future. *Colloids and Surfaces A: Physicochemical and Engineering Aspects*, 241(1–3), pp.3–7.

Song, X.C. et al., 2010. Preparation and photocatalytic activity of Mo-doped WO_3 nanowires. *Journal of Nanoparticle Research*, 12(8), pp.2813–2819.

Sonune, A. & Ghate, R., 2004. Developments in wastewater treatment methods. *Desalination*, 167, pp.55–63.

Standard Methods for the examination of water and wastewater, 1999. *5220 Chemical Oxygen Demand*, American Public Health Association, American Water Works Association, Water Environment Federation. 22nd edition.

Strigul, N.,Koutsospyros, A., Arienti, P., Christodoulatos, C., Dermatas, D., & Braida, W., 2005. Effects of tungsten on environmental systems. *Chemosphere*, 61(2), pp.248–258.

Strigul, N., Koutsospyros, A. & Christodoulatos, C., 2009. Tungsten in the former Soviet Union: Review of environmental regulations and related research. *Land Contamination and Reclamation*, 17(1), pp.189–215.

Strigul, N., Koutsospyros, A. & Christodoulatos, C., 2010. Tungsten speciation and toxicity: Acute toxicity of mono- and poly-tungstates to fish. *Ecotoxicology and Environmental Safety*, 73(2), pp.164–171. Available at: http://dx.doi.org/10.1016/j.ecoenv.2009.08.016.

Stumm, Werner, and Morgan, J.J., 2013. *Environmental Science and Technology : A Wiley-Interscience Series of Texts and Monographs : Aquatic Chemistry : Chemical Equilibria and Rates in Natural Waters.* 3rd editio., Somerset, NJ, USA: John Wiley & Sons.

Susanti, D., Stefanus H., Nisfu, H., Nugroho, E., Purwaningsih, H., Kusuma, G., & Shih, S., 2012. Comparison of the morphology and structure of WO_3 nanomaterials synthesized by a sol-gel method followed by calcination or hydrothermal treatment. *Frontiers of Chemical Science and Engineering*, 6(4), pp.371–380.

Sykes Robert, 2003. *The Civil Engineering Handbook* Second Edi. W. F. Chen & J. Y. R. Liew, eds., New York: CRC Press.

Tiede, K., Alistair B. A. B., Steven P. T., John L., Helen D., & Karen T., . 2008. Detection and characterization of engineered nanoparticles in food and the environment. *Food Additives & Contaminants*, 25(7), pp.795–821.

Tomlinson, A.A.G., 2011. Nanoscale Microscopies. *Nanoporous materials: advanced techniques for characterization, modeling, and processing*. CRC Press ; London

Tseng, T.K., Yi S. L., Yi J. C., & Hsin C., 2010. A review of photocatalysts prepared by sol-gel method for VOCs removal. *International Journal of Molecular Sciences*, 11(6), pp.2336–2361.

University of Florida, 2012. *Dynamic Light Scattering*, @ http://www.phys.ufl.edu/courses/phy4803L/group_IV/light_scattering/dls.pdf. accessed 24 April 2016.

Vamvasakis, I., Georgaki, I., Vernardou, D., Kenanakis, G., & Katsarakis, N., 2015. Synthesis of WO_3 catalytic powders: evaluation of photocatalytic activity under NUV/visible light irradiation and alkaline reaction pH. *Journal of Sol-Gel Science and Technology*, 76(1), pp.120–128.

Vijayakumar, P., Senthil P. M., Sumita M., & Ramasamy, P., 2015. Synthesis and characterizations of large surface tungsten oxide nanoparticles as a novel counter electrode for dye-sensitized solar cell. *Journal of Sol-Gel Science and Technology*, 75(3), pp.487–494.

Vyazovkin, S., 2016. Thermogravimetric Analysis. Available at: https://www.researchgate.net/publication/278307222_Thermogravimetric_Analysis. Accessed 14 February 2017.

Wagner, S.,Gondikas, A., Neubauer, E., Hofmann, T., Von Der K. F.., 2014. Spot the difference: Engineered and natural nanoparticles in the environment-release, behaviour, and fate. *Angewandte Chemie - International Edition*, 53(46), pp.12398–12419.

Wang, P., Huang, B., Qin, X., Zhang, X., Dai, Y., & Whangbo, M. H., 2009. $Ag/AgBr/WO_3.H_2O$: Visible-Light Photocatalyst for Bacteria Destruction. *Inorganic Chemistry*, 48, pp.10697–10702.

Warner, S.D. & Butler, I.S., 2003. Raman and FT-Raman Spectroscopy. *Comprehensive Coordination Chemistry II*, 2, pp.103–112.

Weckhuysen, B.M., 2004. CHAPTER 12 Ultraviolet-Visible Spectroscopy. *In-situ Spectroscopy of Catalysts*, pp.255–270.

Weckhuysen, B.M. & Schoonheydt, R. a., 1999. Recent progress in diffuse reflectance spectroscopy of supported metal oxide catalysts. *Catalysis Today*, 49, pp.441–451.

Weinberg, H., Galyean, A. & Leopold, M., 2011. Evaluating engineered nanoparticles in natural waters. *TrAC - Trends in Analytical Chemistry*, 30(1), pp.72–83. Available at: http://dx.doi.org/10.1016/j.trac.2010.09.006.

Wesley, W., 2000. Literature Review of Temperature Effects in Biological Wastewater Treatment. , pp.1–7.

Wicaksana, Y., Liu, S., Scott, J.,& Amal, R., 2014. Tungsten trioxide as a visible light photocatalyst for volatile organic carbon removal. *Molecules*, 19(11), pp.17747–17762.

Witten, M.L., Sheppard, P.R. & Witten, B.L., 2012. Tungsten toxicity. *Chemico-Biological Interactions*, 196(3), pp.87–88. Available at: http://dx.doi.org/10.1016/j.cbi.2011.12.002.

Wood, V., Panzer, M. J., Halpert, J. E., Caruge, J. M., Bawendi, M. G., & Bulovi, V., 2009. Selection of Metal Oxide Charge Transport Layers for Colloidal Quantum Dot LEDs. *ACS NANO*, 3(11), pp. 3581-3586.

World Bank Water, 2016. Activated Sludge Treatment Process. *The World Bank Group*. @ http://water.worldbank.org/shw-resource-guide/infrastructure/menu-technical-options/activated-sludge. Accessed 20 February 2016.

Wu, L., Bi, J., Li, Z., Wang, X., & Fu, X.i, 2008. Rapid preparation of Bi_2WO_6 photocatalyst with nanosheet morphology via microwave-assisted solvothermal synthesis. *Catalysis Today*, 131(1–4), pp.15–20.

Wu, X., Jiang, X., Chen, Q., Tian, Y., & Hou, X., 2014. Spark ablation-inductively coupled plasma optical emission for elemental depth profiling and imaging. *Microchemical Journal*, 116, pp.157–162.

Xiandeng, H. & Jones, B., 2000. *Inductively Coupled Plasma–Optical Emission*

Spectrometry R.A. Meyers, Chichester: John Wiley& Sons Ltd, Chichester.

Ashokkumar, M., & Maruthamuthu, P., 1989. Preparation and characterization of doped WO_3 photocatalyst powders. , 24, pp.2135–2139.

Yang, Q.L.,Kang, S. Z., Chen, H., Bu, W., & Mu, J., 2011. $La_2Ti_2O_7$: An efficient and stable photocatalyst for the photoreduction of Cr(VI) ions in water. *Desalination*, 266(1–3), pp.149–153.

Yilmaz, V.,Arslan, Z., Hazer, O., & Yilmaz, H.e, 2014. Selective solid phase extraction of copper using a new Cu(II)-imprinted polymer and determination by inductively coupled plasma optical emission spectroscopy (ICP-OES). *Microchemical Journal*, 114, pp.65–72.

Zablotskii, A. V., Avilov, A. S., Bodunov, D. S., Kuzin, A. A., Kuzin, A., Kuz, A. A., & Todua, P A., 2013. A Method for estimating the stability of the scale of a transmission electron microscope. *Measurement Techniques, 56(5), pp.14–16.*

Zanjanchi, M.A., Noei, H. & Moghimi, M., 2006. Rapid determination of aluminum by UV-vis diffuse reflectance spectroscopy with application of suitable adsorbents. *Talanta*, 70(5), pp.933–939.

Zhang, J., Zhang, J., Wang, X. L., Xia, X. H., Gu, C. D., & Tu, J. P., 2011. Electrochromic behaviour of WO_3 nanotree films prepared by hydrothermal oxidation. *Solar Energy Materials and Solar Cells*, 95(8), pp.2107–2112.

Zhang, J., Wang, X. L., Xia, X. H., Gu, C. D., Zhao, Z. J., & Tu, J. P., 2010. Enhanced electrochromic performance of macroporous WO3 films formed by anodic oxidation of DC-sputtered tungsten layers. *Electrochimica Acta*, 55(23), pp.6953–6958.

Zhang, M., Sheng, G., Fu, J., An, T., Wang, X., & Hu, X., 2005. Novel preparation of nanosized ZnO–SnO_2 with high photocatalytic activity by homogeneous co-precipitation method. *Materials Letters*, 59, pp.3641–3644.

Zhao, F. & Yang, Y., 2010. Use of Monodisperse Gold Nanoparticles for Transmission Electron Microscope High Magnification Calibration. *Colloid*

Journal, 72(3), pp.346–352.

Zheng, H., Ou, J. Z., Strano, M. S., Kaner, Richard B., & Mitchell, A., 2011. Nanostructured Tungsten Oxide – Properties , Synthesis , and Applications. *Adv. Funct. Mater.*, 21, pp.2175–2196.

Zheng, H., Tachibana, Y. & Kalantar-Zadeh, K., 2010. Dye-sensitized solar cells based on WO_3. *Langmuir*, 26(24), pp.19148–19152.

Zhu, X., Chen, H., Li, W., He, Y., Brookes, P. C., & Xu, J., 2014. Aggregation kinetics of natural soil nanoparticles in different electrolytes. *European Journal of Soil Science*, 65(2), pp.206–217.

CHAPTER 3
EXPERIMENTAL PROCEDURE

3.1 Materials and reagents

Tungstic acid (99%, Sigma-Aldrich Co.), hydrochloric acid (32%, Sigma-Aldrich Co.), anhydrous sodium hydroxide pellets (≥98%, Associated Chemical Enterprise), humic acid (Sigma-Aldrich Co.), absolute ethanol (99.5%, Associated Chemical Enterprise), magnesium chloride, sodium chloride, calcium chloride (MERCK), meat extract (Sigma-Aldrich Co), magnesium sulphate heptahydrate (99.0%, Merck), urea crystals (99.0%, Merck), di-potassium hydrogen phosphate trihydrate (99.0%, Merck) and peptone from meat enzymatic digest (Sigma-Aldrich Co) were used as received.

3.2 Methodology

3.2.1 Synthesis of WO_3 nanoparticles

Synthesis of WO_3 nanoparticles was achieved by following the standard method reported by Simelane at al.,2017. Tungstic acid (4.0 g) was dried in the oven for two hours at 80˚C to remove any moisture present and crushed before annealing at 600˚C for 5 hours in air to obtain *m*-WO_3 nanoparticles.

3.2.2 WO_3 nanoparticles characterization

The polymorph of WO_3 synthesized was elucidated by using a Philips X'Pert instrument at 40 mA, 40 kV with CuKα radiation at 0.1541 nm wavelength. A monochromatic beam in 2θ was used within the scan range of 10-80˚ and a step size and time of 0.0170 and 175.26s were used respectively. A divergence slit size of 0.2500˚ was used and specimen length was 10.00 mm. The average crystallite size (L) of the nanoparticles was computed using equation **(2.15)**:

Transmission Electron Microscopy (TEM): The morphology was investigated using transmission electron microscopy (JOEL-TEM 2010) at an acceleration voltage of 200 kV. The nanoparticles were analyzed on a carbon-coated copper grid.

The Brunauer-Emmett-Teller (BET): The surface area of the nanoparticles was determined by nitrogen adsorption in a Micrometric ASAP 2020 surface area and pore analyzer. The samples were degassed at 150˚C for 5 hours prior to analysis. Isotherm evaluation was performed at ~77K and pore volume analysis was determined at (P/P_o) of ~0.98. UV-Vis spectrometer (Shimadzu UV-2450) operated in diffuse reflectance mode (DRS) was used to measure the absorbance spectra after which Kubelka-Munk transformation was applied. Barium Sulphate ($BaSO_4$) was used as a reference. The band gap of the nanomaterial was extrapolated from $(\alpha h\nu)^2$ against hν as represented in equation **(3.1)**:

$$\alpha h\nu = A(h\nu - E_g)^{n/2} \qquad \textbf{(3.1)}$$

where α, $h\nu$, A, and E_g are the absorption coefficient, the energy of the incident photon, a constant, and energy bandgap, respectively (Pang et al. 2012). The term n is dependent on the on the transition type of the semiconductor when the transition is direct n equals to 1, while an indirect transition n equals 4 (Zhang et al. 2014).

Raman measurements were performed with a Raman spectrophotometer (Raman Micro 200, Perkin Elmer) using the 514.5 nm wavelength of an Ar^+ laser. Spectra was collected by employing 1800 lines/mm with a holographic notch filter and cooled TCD. Allowed spectral resolution of 3 cm^{-1} was used. Power on the samples was below 0.5 mW to minimize local heating. The Fourier transformed Infrared (FTIR) spectra of H_2WO_4 and WO_3 was captured using the Perkin Elmer processing precisely spectrum 100 FTIR spectrophotometer with a spectral resolution of 4 cm^{-1}. The analysis was conducted at room temperature against an air background. The samples were pressed into a KBr pellet and scanned between 4000-400 wavenumbers (cm^{-1}) to obtain the spectra.

Thermal analysis was also conducted for the stability and thermal properties of both the precursor and the product. This was achieved by employing the Perkin Elmer TGA-4000 with the heating rate set at 10 ˚C/min starting from 30-800 ˚C under nitrogen gas. A sample of 10.0 mg in weight was used. The thermograph derivatives were obtained using OriginPro 8 software. Hydrodynamic diameter (size) measurements were achieved by dynamic light scattering (DLS) and zeta potential by electrophoretic light scattering (ELS) by means of a Zetasizer Nano ZS (Malvern).

3.2.3 Stability studies in environmentally relevant conditions

3.2.3.1 Zeta potential and hydrodynamic diameter measurements

The hydrodynamic diameter and zeta potential of WO_3 was determined by suspending nanoparticle into 30 mg/L in deionized (DI) water. The pH of the suspensions was then adjusted to the appropriate values in the range of 2-10 using 6 M NaOH and 6M HCl.

3.2.3.2 Effects of ionic strength and cations

The effect of ionic strength was conducted at pH 5 at room temperature. At pH 5, the nanoparticles were efficient enough to demonstrate substantial agglomeration without compelling the compression of the electric double layer in the DI suspension which is also in the range of surface water pH. A range of 0.2-10 mM ionic strength of monovalent cation (NaCl), and divalent cations ($MgCl_2$ and $CaCl_2$) were prepared. Aliquots of 100 mL from each solution were taken and adjusted to the appropriate pH using HCl.

3.3 Study of humic acid effect on nanoparticles

3.3.1 Humic acid preparation

A 50 mg/L stock solution of HA was prepared by dissolving 50 mg in 1 L deionized water and further adjusting the pH to 5. The prepared solution was covered with aluminum foil to avoid exposure to light. The solution was then stirred for 24 hours to ensure homogeneity and stability. The solution was filtered with 0.22 µm filter membrane to remove undissolved matter. A series of working solutions ranging from 1 to 10 mg/L were prepared by diluting the stock solution.

3.3.2 Influence of humic acid on nanoparticles stability

The effect of humic acid was studied by comparing the effect of monovalent to divalent cations. Different suspensions containing 1 to 10 ppm humic acid were prepared and their pH adjusted to pH 5. The suspensions were then vortexed for 15 minutes for dispersion of the nanoparticle. A disposable polystyrene cuvette was used as a sample holder during analysis. Zeta potentials and electrophoretic mobility (EPM) measurements were taken immediately with the size measurements performed after an hour with all readings taken in triplicates.

3.4 Fate and behaviour WO_3 nanoparticles

3.4.1 Influent and activated sludge

The raw wastewater was sampled from Daspoort wastewater treatment works in Pretoria (Gauteng, South Africa), which is mainly a domestic sewage treatment plant. Sampling point was just after the primary treatment and it was performed every seven days with the secondary influent refrigerated at 4˚C.

A synthetic domestic wastewater was used as influent prepared with peptone (160 mg), meat extract (110 mg), urea (30 mg), anhydrous dipotassium hydrogen phosphate (28 mg), sodium chloride (7 mg), calcium chloride dehydrates (4 mg), magnesium sulphate heptahydrate (2 mg) and 5 mg of humic acid per litre of water

(OECD guidelines, 2001). However, it was first mixed with the raw wastewater to ensure that the activated sludge is acclimatised to the synthetic influent. The raw wastewater was reduced gradually such that on sludge retention time (SRT) 4, the treatment plant operated on 100% synthetic influent.

Return activated sludge with a sludge retention time of 6-10 days was also withdrawn from the above-mentioned treatment works and kept similarly to the influent. It was used as an inoculum for the lab scale simulated wastewater treatment plant (SWPT) as per the OECD 303A guidelines. For the inoculation of the SWTP, 10 L of the activated sludge was aerated using compressed air for a duration of 48 hours. In the first 24 h the supernatant was decanted and influent (raw wastewater) was added. At the end of the aeration process, the supernatant was decanted, stored and mix with fresh influent for the first two (2) days of SRT 1. The aerated sludge was partitioned and added into the two bioreactors.

3.4.2 Lab scale activated sludge SWTP (OECD 303A)

The OECD guidelines 303A were used to assemble a treatment system used to study the fate and behaviour of WO_3 nanoparticles which resembled a simulated wastewater treatment plant (SWTP) with synthetic domestic effluent. The SWTP comprised of a test and control units as demonstrated in **figure 3.1**. The aerobic units consisted of an aeration chamber (3 L) and a settler (1.5 L) which were run uninterruptedly in parallel under similar conditions with a mean hydraulic retention time (HRT) of 6 h with a flow rate of 0.5 L/h and mean SRT of 7 days until a steady state was reached.

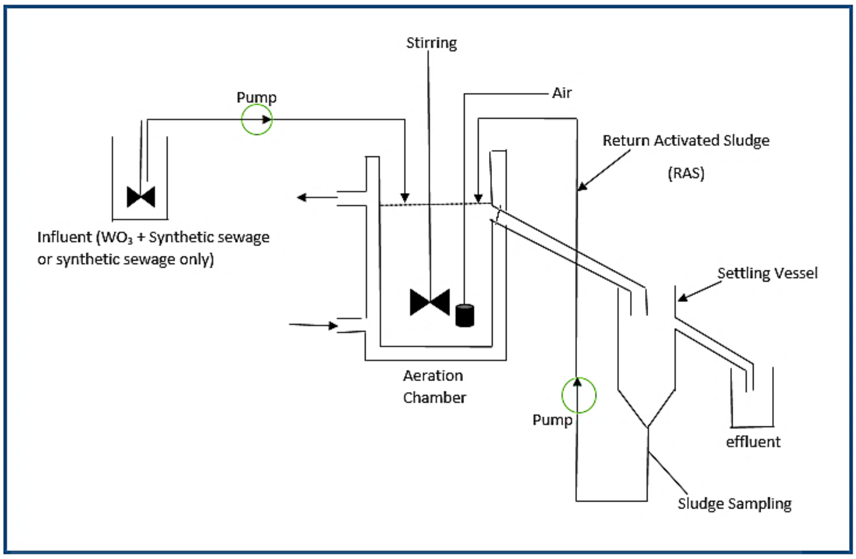

Figure 3.1: A schematic representation of the SWTP.

The influent held in 20 L holding tank was continuously pumped into the aeration chambers using 120S/DV Watson-Marlow peristaltic pumps which were under constant staring (RW 20 digital stirrers, IKA) to enhance homogeneity of the suspension and mixing of the floc with the influent. Influent in the holding tanks was continuously stirred to keep its contents in suspension and it was changed every 24 h. Aeration of both units was achieved using a perforated tube and compressed air to maintain dissolved oxygen above 2 mgL^{-1} delivered at a flow rate of 250 mL/min. Return activated sludge was achieved by using the 323S peristaltic pumps (Watson-Marlow) which recycled sludge from the clarifiers to the aeration vessels continuously.

3.4.3 Preparation of *m*-WO_3 NPs suspensions

The different concentrations of WO_3 suspensions (5, 10, 15 and 20 mg/L) were prepared by dispersing 0.1000, 0.2000, 0.3000 and 0.4000 g of dry *m*-WO_3 nanoparticles into a 20 L of synthetic domestic influent. The weighed nanoparticles were first dispersed in 1L influent and sonicated at 20 KHz for 30 minutes (model 2000U, Ultrasonic Power Corp.). this was done to break aggregates before introducing the set concentrations to the holding tanks. The use of suspensions enabled a homogeneous application of the nanomaterials to the test units. Once the suspensions were successfully prepared, the hydrodynamic sizes and the zeta potential of the agglomerates were measured using the Malvern zetasizer NanoZS.

3.4.4 Acclimatization of the activated sludge

In ensuring that the microorganisms in the sludge are fully acclimatized to the SWTP, raw wastewater was used to run the plant while increasing the synthetic influent. In SRT 1, 100% influent was mixed with the kept supernatant in the first 2 days and the raw wastewater was used in the reminder of the days. However, the aim was to run the treatment plant with 100% synthetic influent thus the ratio of the raw wastewater was gradually reduced in the next SRT’s as shown in **Table 3.1**.

Table 3.1 Influent composition for acclimatization of microorganisms

SRT	Days	Influent composition
1	0-7	100% secondary influent
2	8-14	50% 2˚ influent + 50% synthetic domestic effluent
3	15-21	30% 2˚ influent + 70% synthetic domestic effluent
4	22-49	100% synthetic domestic effluent

3.4.5 Monitoring of the simulated treatment plant

The treatment system efficiency was monitored through several chemical and physical tests which were conducted in both the aeration chambers and effluent. The tests conducted in the aeration chambers included MLVSS, MLSS and the monitoring of abiotic factors; temperature and dissolved oxygen (DO) using Starter DO 300D. The monitored abiotic factors are responsible for the well-being of the microorganisms in the activated sludge. The total plate count (TPC) method was used to determine the survival of the microorganisms in aeration chambers upon introduction of the *m*-WO_3 NPs. The agar for the TPC test was prepared following the manufacturer's instructions.

In both influent and effluent, the tests performed included chemical oxygen demand (COD), five-day biological oxygen demand (BOD_5), total dissolved solids (TDS), conductivity and pH. The TDS, conductivity, and pH were measured using Starter conductivity 300˚C and Starter pH 300, OHAUS. The total suspended solids (TSS) were also part of the analysis conducted on the effluents. A COD kit (1.14541.0001, Merck) equivalent to a German standard DIN EN ISO 7393 and a BOD kit (1.00687.0001, Merck) conforming to the European standard EN 1899 210 mgL^{-1} were used for the analysis of COD and BOD_5 respectively, using a Spectroquant Pharo 300 and samples were filtered prior to preparation using a 0.45 µm filter.

For analysis of the suspended solids, a glass microfibre filter with 0.6 µm pore size was used to filter 250 mL sample. They were then dried in the oven for 5 hours at 103-105˚C. However, for the MLVSS analysis, the already dried samples were then burnt at 550˚C for 15 to 20 minutes.(Greenberg et al. 1992)

3.4.6 Analysis of Activated sludge for WO_3 and W

The waste sludge was dried in the oven at 50 ˚C for 24 hours and pulverized prior to qualitative analyses. The polymorph of the *m*-WO_3 nanoparticles in the sludge was characterized using powdered X-ray diffraction as outlined in **section 3.2.2**. Elemental analysis was conducted using energy dispersive X-ray spectroscopy and SEM mapping (TESCAN Vega TC) using VEGA 3 TESCAN software under nitrogen gas on the sludge to ascertain the distribution of the tungsten element.

Furthermore, inductively coupled plasma optical emission spectrometer (ICP-OES) (iCAP 6500 Duo, Thermo Scientific) was used to quantify the amount of tungsten in both the sludge and the effluent by analyzing the already digested samples (0.25g sludge and 5 mL effluent) with aqua regia (3 mL HCl and 2 mL HNO_3).

3.5 References

Greenberg, A., Clesceri, L. & Eaton, A., 1992. Standard Methods for the Examination of Water and Wastewater 18th ed., Washington: American Public Health Association. @ https://www.mwa.co.th/download/file_upload/SMWW_4000-6000.pdf Accessed February 21, 2017.

Organization for Economic Co-operation and Development 303A, 2001. Aerobic Sewage Treatment – activated sludge units. Guidelines for the testing of chemicals. @ http://www.oecd.org/chemicalsafety/testing/34898616.pdf. Accessed 15 April 2016).

Pang, H. F., Xiang, X., Li, Z., Fu, Y., & Zu, X. 2012. Hydrothermal synthesis and optical properties of hexagonal tungsten oxide nanocrystals assisted by ammonium tartrate. *Physica Status Solidi (a), 209(3), pp.537–544.*

Simelane, S., Ngila, J. C. & Dlamini, L. N., 2017. The Effect of Humic Acid on the Stability and Aggregation Kinetics of WO_3 Nanoparticles. *in Press Particulate Science and Technology. doi:10.1080/02726351.2017.1302536.* Accessed 24 March 2017.

Zhang, L.J., Li, S., Liu, B. K., Wang, D. J., & Xie, T. F., 2014. Highly efficient CdS/WO_3 photocatalysts: Z-scheme photocatalytic mechanism for their enhanced photocatalytic H_2 evolution under visible light. *ACS Catalysis, 4(10), pp.3724–3729.*

CHAPTER 4
THE EFFECT OF HUMIC ACID ON THE STABILITY AND AGGREGATION KINETICS OF WO_3 NANOPARTICLES *

** Part of the work presented in this chapter has been reported and published in Particulate Science and Technology (2017)*

4.1 Introduction

Stability and dissolution of NPs in natural waters are influenced by dissolved natural organic matter (NOM), ionic strength, type of electrolyte, aggregation state, and pH (Bian et al. 2011). Much work has been focused on Fe_2O_3, ZnO, Al_2O_3 and TiO_2 in understanding their behaviour in surface water, due to their extensive use (Baalousha 2009; Brunetti et al. 2015; Pakrashi et al. 2012; Chekli et al. 2014). However, interest in WO_3 has gained momentum because of its small band gap, allowing its applications in the visible spectrum. Thus, this dissertation seeks to report the effects of NOM, ionic strength, and valence of ions on the stability aggregation kinetics of WO_3 in water.

Divalent cations may cause aggregation at a wider range of pH compared to monovalent cations. This is due to the specific adsorption effect that prevents the surface charge acquiring a negative charge large enough to create a potential barrier large enough to minimize aggregation. The stabilization effect of natural organic matter (NOM) overrides the divalent ions influence towards aggregation at low cation concentrations. At high concentrations, cations such as Ca^{2+} neutralizes the electrostatic stabilization thus inducing aggregation. This is not observed with Mg^{2+} though, suggesting the existence of Ca^{2+}-NOM interactions such as calcium bridges (Belen et al. 2013; Weinberg et al. 2011).

NOM is mostly found in natural waters with its concentration ranging from a few mg/L to hundreds of mg/L (Wall & Choppin 2003). Humic acid (HA) is one example of NOM which constitutes heterogeneous chemicals and functional groups due to the various sources from where they are obtained which are mostly phenols and carboxylic functional groups which enable the protonation of OH/OOH (Li et al.

2015; de Melo et al. 2015). Therefore, NOM has been found to increase the negativity of NPs zeta potential thus reducing the aggregation of the NPs (Bian et al. 2011; Zhang et al. 2009).

4.2 Characterization of WO_3 nanoparticles

4.2.1 Powder x-ray diffraction spectroscopy

The PXRD patterns of the precursor tungstic acid (H_2WO_4) **(a)** and those of m-WO_3 nanoparticles **(b)** is as shown in **Figure 4.1**. The nanoparticles were crystalline with indices corresponding to (002), (020), (200), (120), (112), (022), (202), (122), (222), (004), (040), (140), (024), (204), (240), and (420) respectively (Vamvasakis et al. 2015). These were confirmed by ICDD:04-007-1277, space group $P2_1/n$ with lattice constants a=7.291 Å, b=7.539 Å, c=7.688 Å and β=90.91. The precursor, tungstic acid PXRD patterns were also obtained to ascertain the resultant polymorph of WO_3 after calcination. The tungstic acid hydrate indexed to space group *Pmnb* according to ICDD: 00-018-1418 had a peak appearing around 16˚ amongst others which appears in H_2WO_4 patterns yet absent in WO_3 pattern. The observed *m*-WO_3 peaks were sharp and intense thus indicating the crystallinity of the nanoparticles. The calculated crystallite size was 15±0.5 nm.

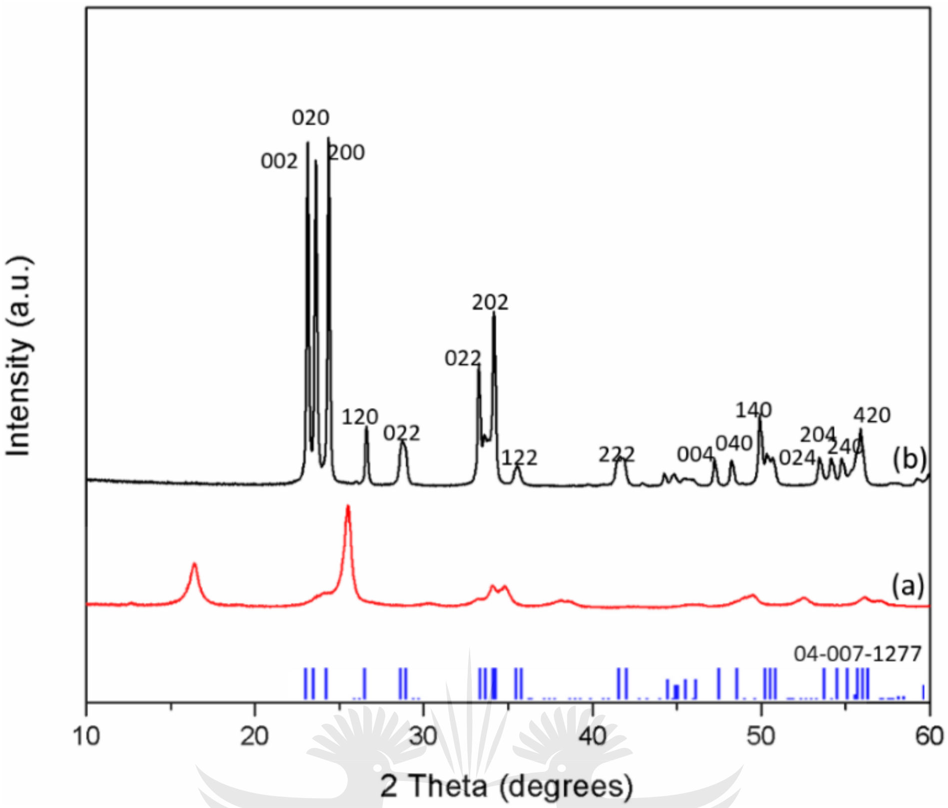

Figure 4.1 PXRD patterns of (a) H_2WO_4 and (b) WO_3

4.2.2 Raman spectroscopy

The Raman bands of the precursor and the obtained product as depicted in **Figure 4.2 (a, b)** distinctly confirm the transformation of tungstic acid to *m*-WO_3 The observed bands of *m*-WO_3 were sharp and well defined positioned at 806, 717, 326, 269 and 135 cm^{-1} which are assigned to *m*-phase of WO_3 (Daniel et al. 1987; Fenglin Liu, Xianjie Chen, Qinghua Xia, Lihong Tian 2015). This result supports the XRD determination of the polymorph of the synthesised materials. The band at 135 cm^{-1} corresponded to lattice vibrational modes of W-W while the peaks at 717 and 806 cm^{-1} were ascribed to the stretching modes of the W–O–W. The strong peak and weak band observed at 269 and 326 cm^{-1} respectively were attributed to the bending modes of O-W-O. The peak position in at 945 cm^{-1} in the precursor could be ascribed to W=O which completely disappears after calcination at 600 ˚C (Daniel et al. 1987).

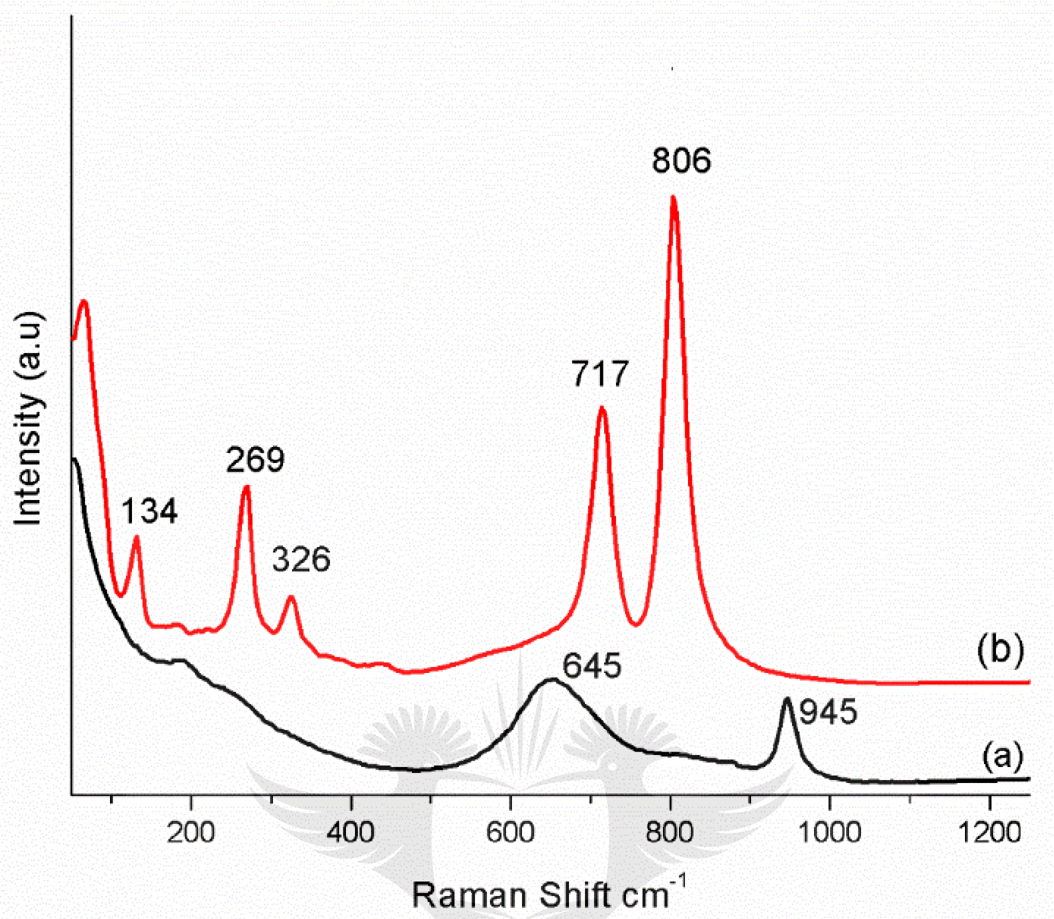

Figure 4.2: Raman bands of (a) H_2WO_4 and (b) *m*-WO_3

4.2.3 Fourier transformed infrared spectroscopy

Figure 4.3, shows the FTIR spectra of H_2WO_4 and *m*-WO_3 which reveals the transformation of the precursor to the product. The spectrum of H_2WO_4 shows five IR bands at 3409, 1637, 1386, 944 and 711 cm^{-1}. A broadband and a sharp intense peak at 3409 and 1637 cm^{-1} respectively are associated with the υ(O-H) stretching modes which are due to adsorption of water molecules and δ(H-O-H) bending vibration modes in H_2WO_4. The intensity of this OH bands is greatly reduced in the WO_3 spectra and they are shifted to 3424 and 1637 cm^{-1}. These two bands are greatly reduced in the WO_3 spectra. The disappearance of the 944 cm^{-1} shoulder peak is attributed to the absence of the W=O in the *m*-WO_3 octahedral structure. (Gotić et al. 2000; Daniel et al. 1987; Pang et al. 2012) The peak observed in *m*-WO_3 and H_2WO_4 at 1384 and 1386 is ascribed to v(O-H) in the W-OH.(Ghosh et al. 2015)

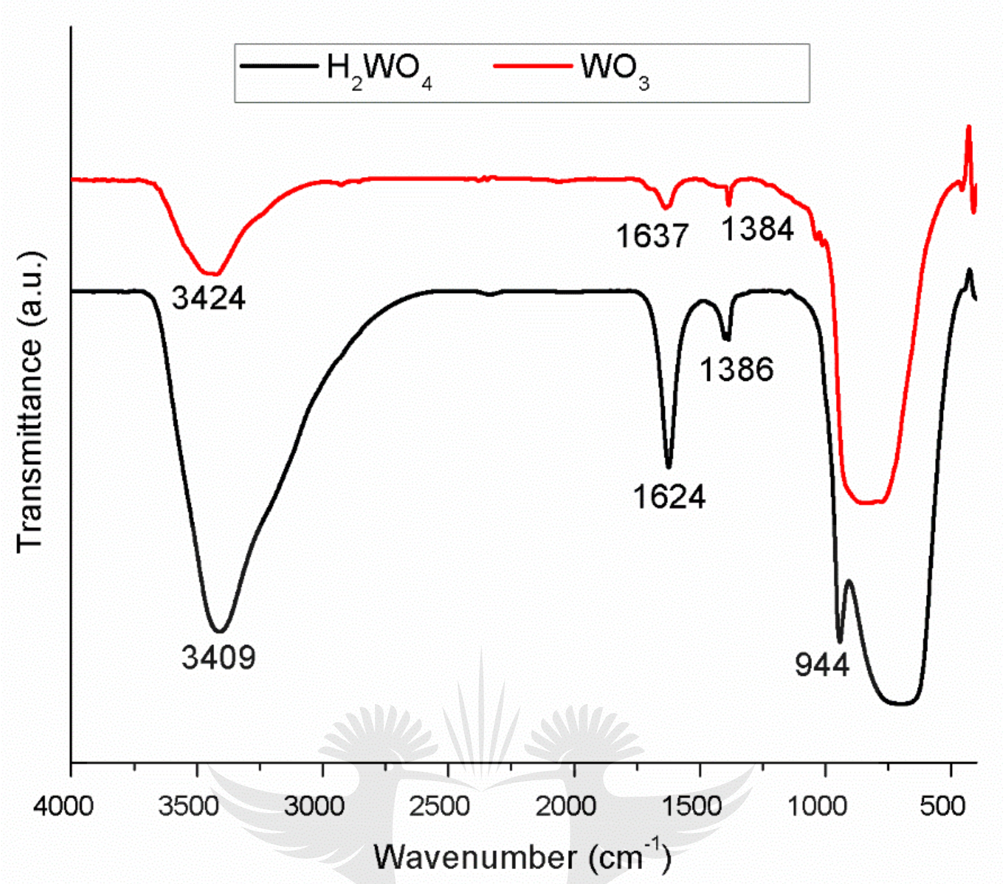

Figure 4.3: FTIR spectra of H_2WO_4 and *m*-WO_3

4.2.4 Thermo-gravimetric analysis

The significant change in the structural and physical difference of H_2WO_4 and *m*-WO_3 was determined using thermal analysis. **Figure 4.4** depicts the TGA curves and its derivatives for H_2WO_4 and WO_3. The percentage weight loss in tungstic acid was 5.66% which is equivalent to 3.14 mmol of water at a temperature ranging from 80˚C to 280˚C with the maximum at 225˚C as illustrated by the derivative of the weight percentage graph. This weight loss is due to chemically bonded water.(Huang et al. 2011) The recorded weight loss is different from the expected theoretical value of 7.20% which is based on water lose.(Gotić et al. 2000) This observation is aligned with the FTIR spectra of *m*-WO_3 which shows the presence of OH bands. WO_3 had a weight loss of 0.4% corresponding to 0.19 mmol water which occurred from 150˚C while the weight derivative did not have a minimum due to the continuous weight loss as the temperature increases. When comparing the amount of water lost in millimoles, it is evident that H_2WO_4 was successfully transformed to *m*-WO_3.

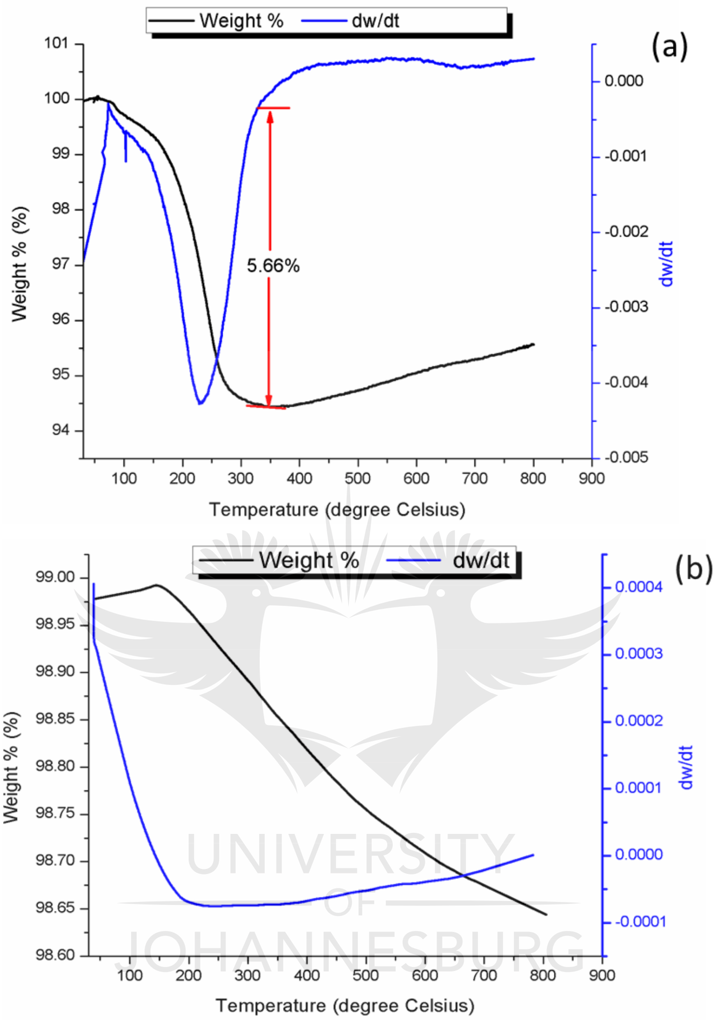

Figure 4.4: TGA curve and derivatives of (a) H_2WO_4 and (b) *m*-WO_3

4.2.5 Surface area, pore size, and pore volume

Surface area and pore volume measurements were determined to be 3.544 m^2g^{-1} and 0.008507 cm^3/g respectively with the pore size ranging between 3-13 nm with the average being 9.60 nm as demonstrated in **Figure 4.5(a)**. The observed surface area is comparable to the 3.32 m^2g^{-1} reported for commercial *m*-WO_3 attributed to agglomeration of nanoparticles which was confirmed by the hysteresis loop (Martínez et al. 2011; Gomez et al. 2013). The N_2 adsorption-desorption isotherms depicted in **Figure 4.5(b)** revealed that the nanoparticles were mesoporous with type IV isotherm characteristics. The observed hysteresis loops were of H1 type suggesting that samples were constituted of agglomerates porous (Sing 1982).

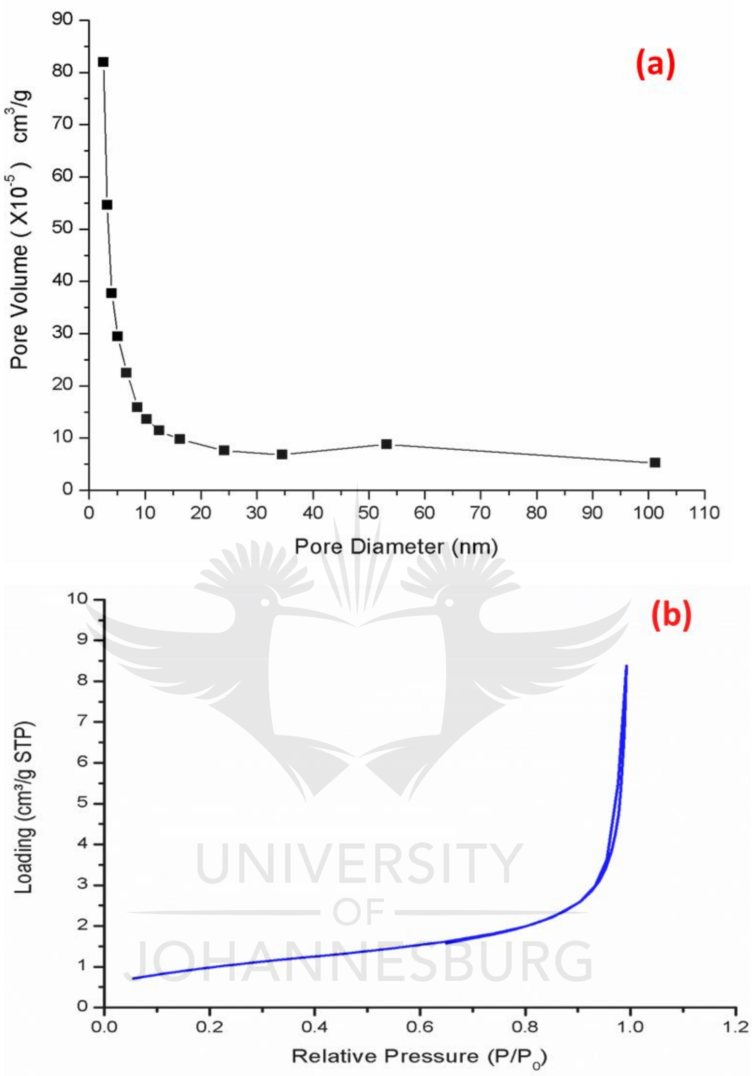

Figure 4.5: (a) Pore size distribution curves and (b) Nitrogen adsorption isotherms measured at ~77K for *m*-WO_3

Determination of the particle size (assuming spherical particles) was carried out using the measured BET surface area following equation **(4.1)**:

$$d = \frac{6000}{SA\rho} \qquad \textbf{(4.1)}$$

where d is the particle size in nm, SA is the experimentally measured specific surface area (m^2 g^{-1}), and ρ is the *m*-WO_3 density (Marei et al. 2016). The calculated particle size was 236.5 nm, which was in agreement with the TEM data as the minimum measure particle was 36.47 nm with the maximum size (agglomerates) being 255.0 nm.

4.2.6 Morphological and elemental studies

The optical properties of the synthesized nanoparticles were determined at ambient temperature to obtain the spectrum portrayed in **Figure 4.6**. The bandgap was then determined by an extrapolation of the linear region to the point where $E_g = h\nu$ as illustrated in the insert. The bandgap of *m*-WO_3 was found to be 2.71 eV which agrees with literature. This infers that the synthesized WO_3 is capable of absorbing radiation in the visible region of 472 nm which corresponds to the absorption edge of the material. This observation is due to an electronic transition from O^{2-} to W^{6+} by charge transfer process from the valence band (mainly 2p orbitals of the oxygen anions) to the conduction band (mainly 5d orbitals of the tungsten cations) in WO_3 (Martin, C. et al. 1997; Luévano-hipólito et al. 2014).

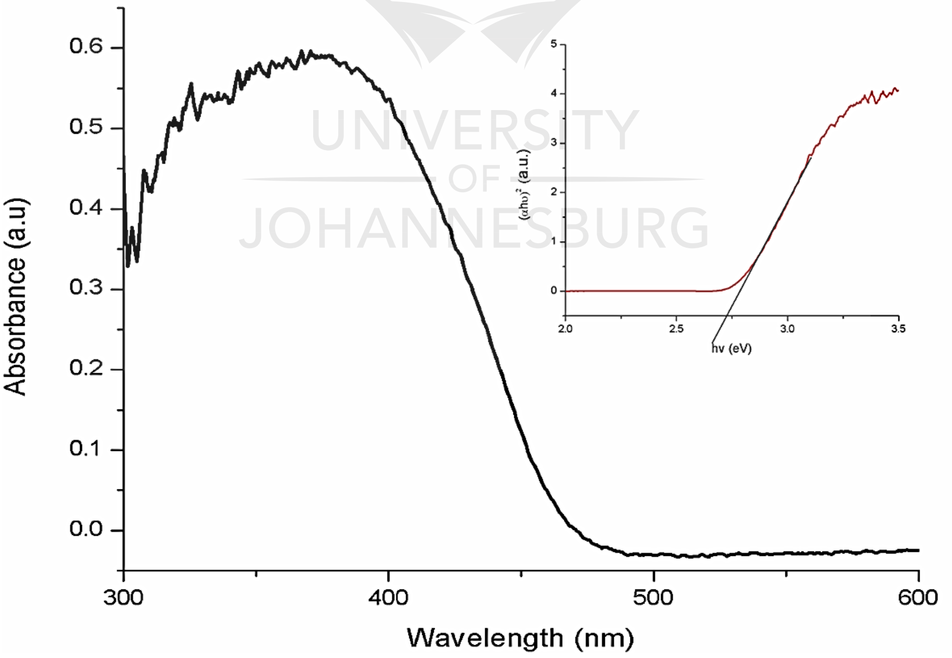

Figure 4.6: UV-Vis absorption spectra of *m*-WO_3. The insert is a plot of $(\alpha h\nu)^2$ versus photon energy

TEM images revealed that the nanoparticles were agglomerated, which was confirmed using SEM. It further, showed that the synthesised material constituted of various shapes such as platelets, ovoid, hexagonal and cubic as depicted in **appendix 1** with a mean size distribution diameter of 156.07 nm as illustrated in **Figure 4.7(a)**. This observation agrees with the particle size obtained using the BET results as illustrated in the histogram in **Figure 4.7(c)**. The size distribution ranged from 36 nm to 255 nm. SEM further showed the presence of fluffy materials as demonstrated in **Figure 4.7(b)**.

Figure 4.8 is an EDX spectrum of the prepared nanoparticles showing the detected elements being W and O. the average percentages were 54.1, 24 and 22 respectively. The observed C peak is due to the coating used during sample preparation.

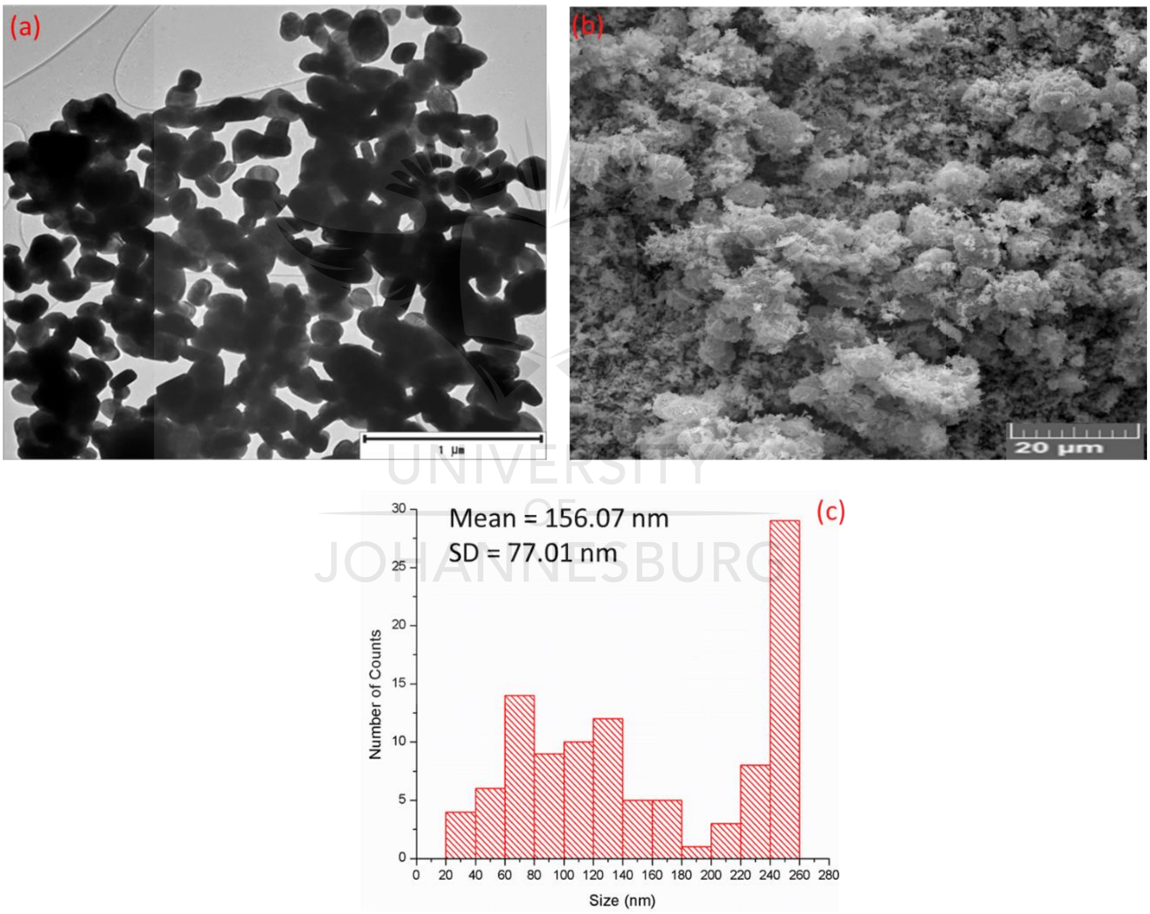

Figure 4.7: (a) Image of *m*-WO_3 from TEM (b) SEM image of the particles and (c) histograms depicting the size on nanoparticles

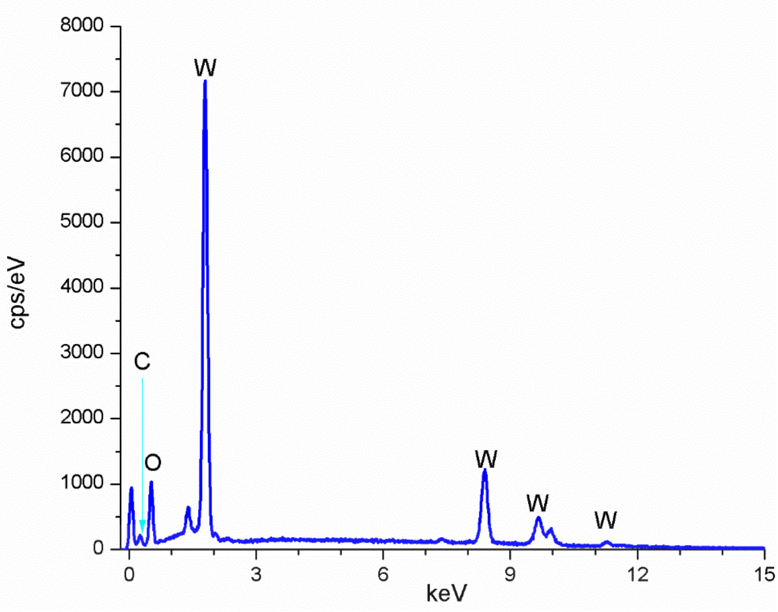

Figure 4.8: EDX spectrum of *m*-WO_3 nanocomposites

4.2.7 Zeta potential measurements

Zeta potential is one of the parameters that is used to indicate the stability of nanoparticles in suspensions. Application of the Smoluchowski equation on the EPM gave zeta potential as depicted **Figure 4.9**.

As the pH increased from pH 2 to pH 10, a steady but gradual change of the zeta potential from positive to negative in the DI water suspensions was observed. The pzc for the nanoparticles was determined as shown in **Figure 9(a).** The pzc was found to be at pH 2.5 which agrees with what is reported in the literature.

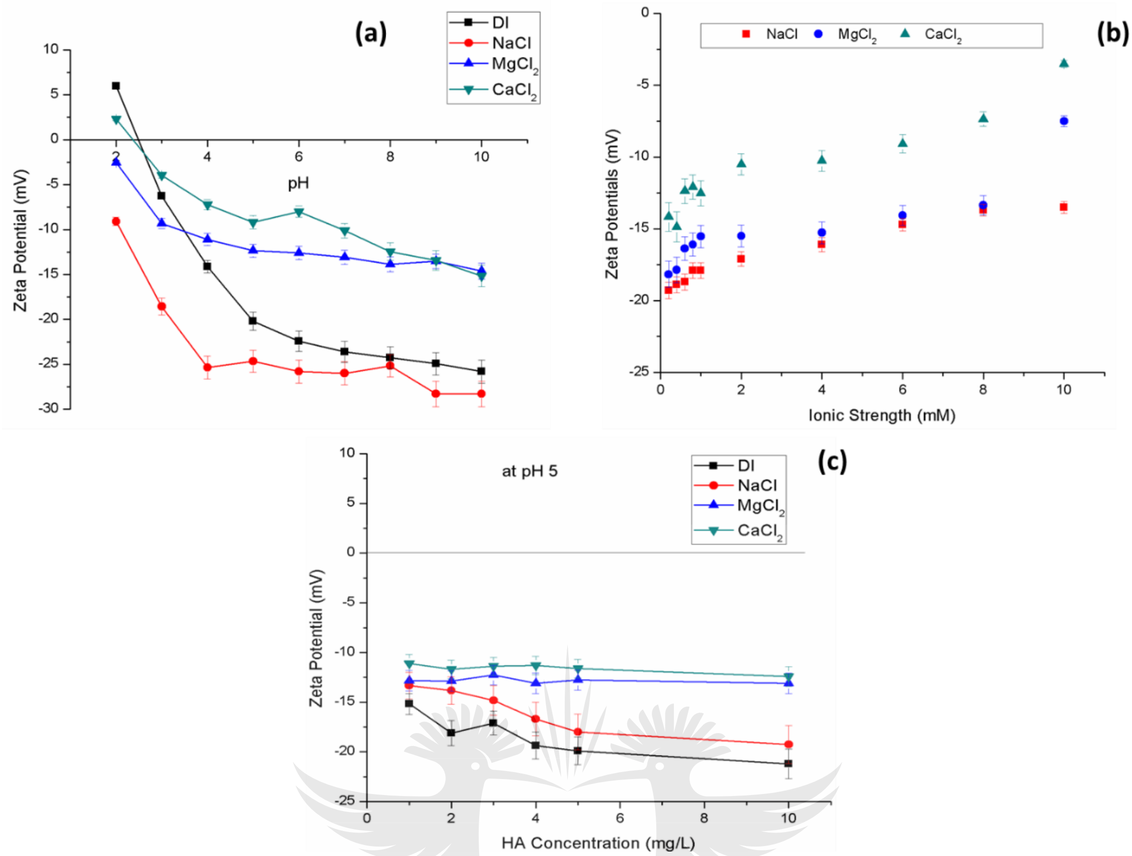

Figure 4.9: Zeta potential in different solutions (a) function of pH, (b) in different humic acid concentrations with 0.9 mM and (c) in different ionic strength.

The zeta potential was further measured in the various ionic strength of the different electrolytes. This was done to ascertain the effect of increasing ionic strength and to determine how different cations will influence the zeta potential of the nanoparticles. In all the suspensions, the zeta potential was all negative as demonstrated in **Figure 4.9(b)** in the presence of the different ionic strengths. This was in line with the determination made in DI water suspension where a zeta potential of -20.2 mV was measured at pH 5. $CaCl_2$ showed to greatly reduce the negative potential compared to NaCl and $MgCl_2$ as a zeta potential of -3.5 mV was measured at the highest ionic strength of 10.0 mM. In all the different electrolytes, an increase in ionic strength decreased the negativity of the zeta potential. This shows that Mg^{2+} and Ca^{2+} were able to suppress the electric double layer of the nanoparticle. Increasing the ionic strength of divalent ions enhance the dominance of attractive to forces aggregation of the nanoparticle.

The pzc in the presence of 0.9 mM $CaCl_2$ was found to be at pH 2.3 which shows a shift to a lower pH value when compared to that in DI Suspension. The pzc could not be determined in the NaCl and $MgCl_2$ solutions, as the nanoparticles were positively charged in DI water suspensions at pH range below 2.5. The chloride ions which are negatively charged were attracted to the positively charged nanoparticles thus creating a weakly negatively charged surface (pre-pzc).

NOM is abundantly found in subsurface and groundwater where they can adsorb to the surface of nanoparticles. The zeta potential of *m*-WO_3 became more negative as the concentration of humic acid was increased in DI water suspension at pH 5 as shown in **Figure 4.9(c)**. The negative charge of nanoparticles can be attributed to the ionization of the carboxylic acids groups present in humic acid (Gotić, M. et al., 2000).

4.2.8 Mean diameter and agglomeration rates

For determination of the agglomeration rates, the samples were allowed to equilibrate for 120 seconds after the measurement has been started. Seven measurements were taken each set with 3 runs set so be done over 30 seconds each. The rate of agglomeration was determined as the slope of the of the mean diameter against time plot as demonstrated in **Figure 4.10**.

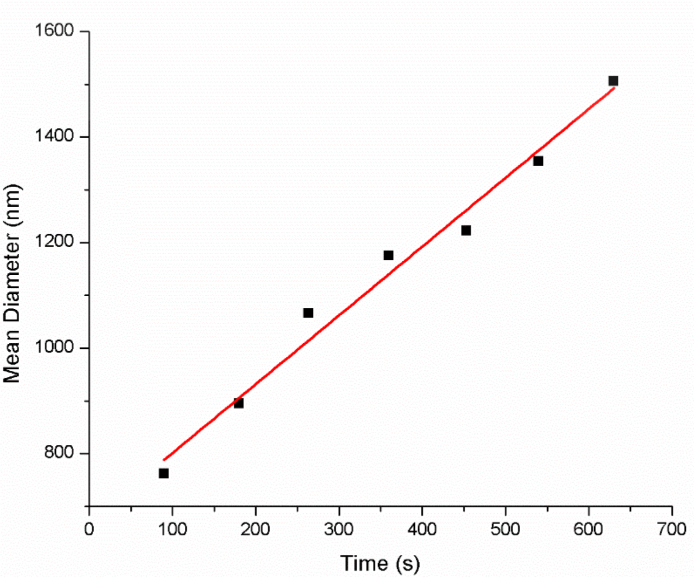

Figure 4.10: Mean diameter against time plot

The rate of agglomeration followed a similar pattern as it was below 0.5 nm/s in pH greater than 7. As the ionic strength increased with the different electrolytes, the rate of agglomeration increased. The increase in the agglomeration rate resulted in bigger hydrodynamic diameters being observed. This was due to the dominance of the attraction forces over the electrostatic repulsion forces. At pH 5, the hydrodynamic diameter in DI suspension was 1800 nm with the rate of agglomeration being 1.2 nm/s as demonstrated in **Figure 4.11(a)**.

The hydrodynamic size of the nanoparticles was determined in DI water suspension at different pH range for different electrolytes suspension. The nanoparticles had the highest hydrodynamic size around the pzc. The size decreased towards less acidic conditions. The data is in accordance with the zeta potential measurements which shows an increase in negative charge, inferring to the stability and hence dispersion of the nanoparticles.

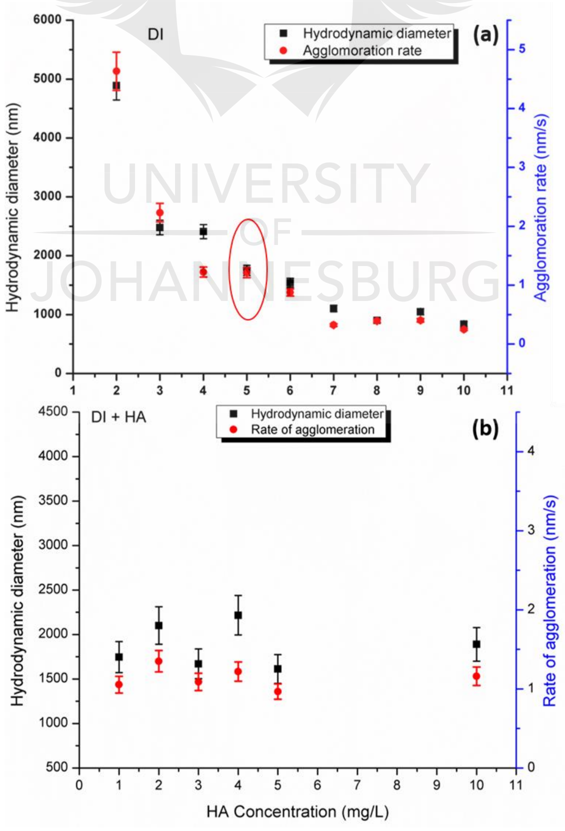

Figure 4.11: Mean hydrodynamic diameter and agglomeration rate (a) function of pH in DI water suspension (b) Humic acid concentration at pH 5

In the presence of humic acid, the hydrodynamic diameter was around 2000 nm with the agglomeration rate at 1.0 nm/s as in **Figure 4.11(b)** in DI suspension. A 0.2 nm/s decrease in the rate of agglomeration suggesting an increased stability of the nanoparticles compared to DI water suspension at pH 5. Since the nanoparticles were negative, particle-particle repulsion forces were dominant thus making the particles stable.

4.3 Effect of ionic strength on the kinetics *m*-WO_3 NPs

Ionic strength is among the factors that govern agglomeration of nanoparticles in suspensions due to its influence on the magnitude of the electric double layer (EDL). The thicker the EDL, the more dispersed the particles due to increased particle–particle repulsions. Thus, increase in ionic strength suppresses the EDL resulting in agglomeration of particles in solution. However, the charge of the ions present was primarily responsible for the reduction of EDL (Ghosh S.S. et al. 2015).

The interaction energy calculated following the DLVO theory (equation **2.3 - 2.5**) showed that's the total energy is repulsive in the NaCl solution suspensions in the whole range of the ionic strength. The calculation was done for three concentration, low (0.2 mM), medium (1.0 mM) and high (10.0 mM) to understand the behaviour of the interaction energy with an increase of ionic strength. **Figure 4.12** shows the hydrodynamic diameter, rates of agglomeration and the interaction energy plots in various ionic strengths.

At low concentration of NaCl, the electrostatic repulsive forces were dominant and van der Waals attractions were negligible (**Figure 4.12**), which lead to a substantial energy barrier preventing the aggregation of nanoparticles. However, the electrostatic energy barrier decreased as the electrolyte concentration increased while the electrostatic repulsive force decreased, as a result, the hydrodynamic size increases. This observation was comparable to the size observed at pH 5 in DI suspension where a mean diameter of 1750 nm.

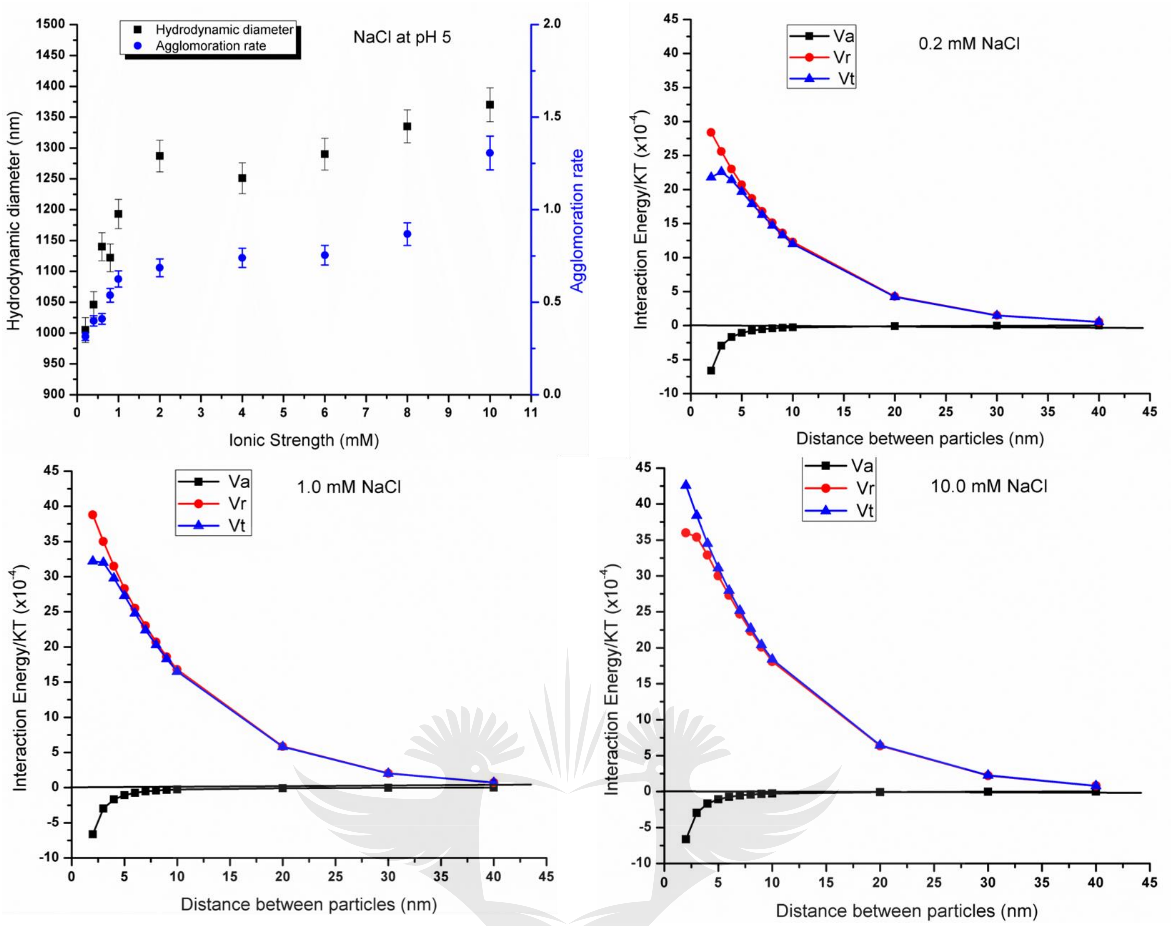

Figure 4.12: Mean hydrodynamic diameter and rate of agglomeration and interaction energy plots at 0.2, 1.0 and 10.0 mM NaCl.

$MgCl_2$ and $CaCl_2$ showed to significantly compress the double electric layer of the surface of the nanoparticles. The overall interaction energy in the two suspensions showed to be attractive as shown in **Figure 4.13** and **4.14**.

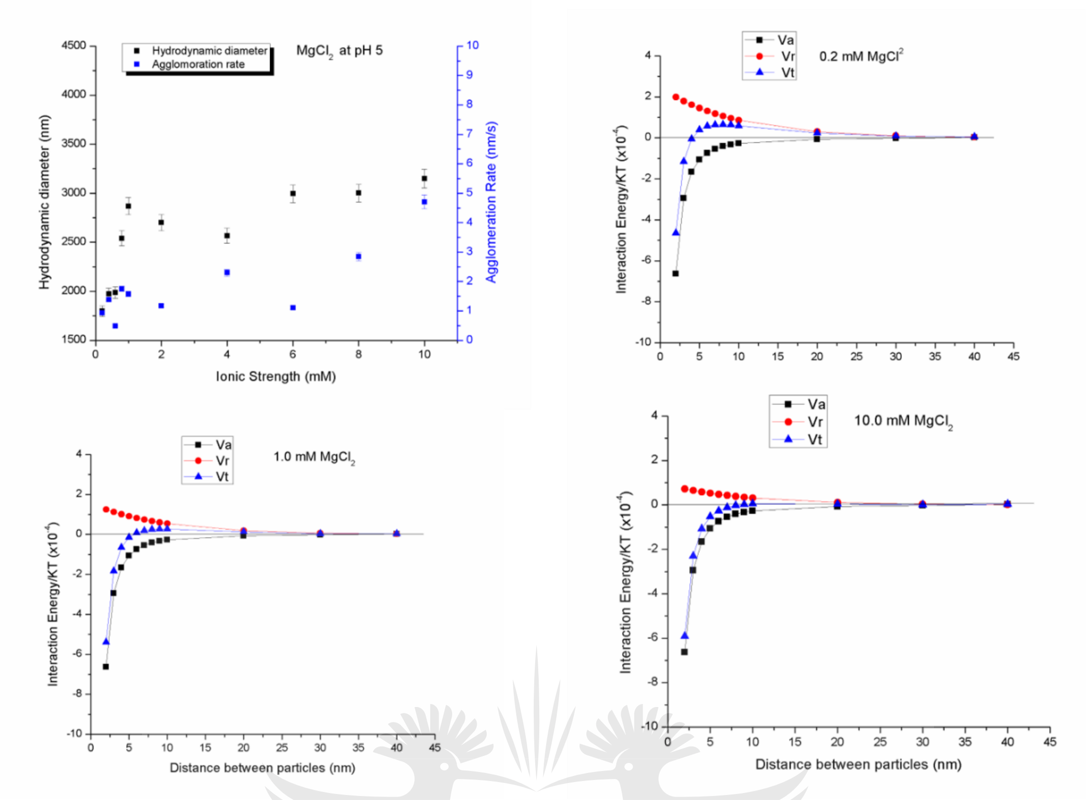

Figure 4.13: Mean diameter and rate of agglomeration and (b) interaction energy plots at 0.2, 1.0 and 10.0 mM $MgCl_2$

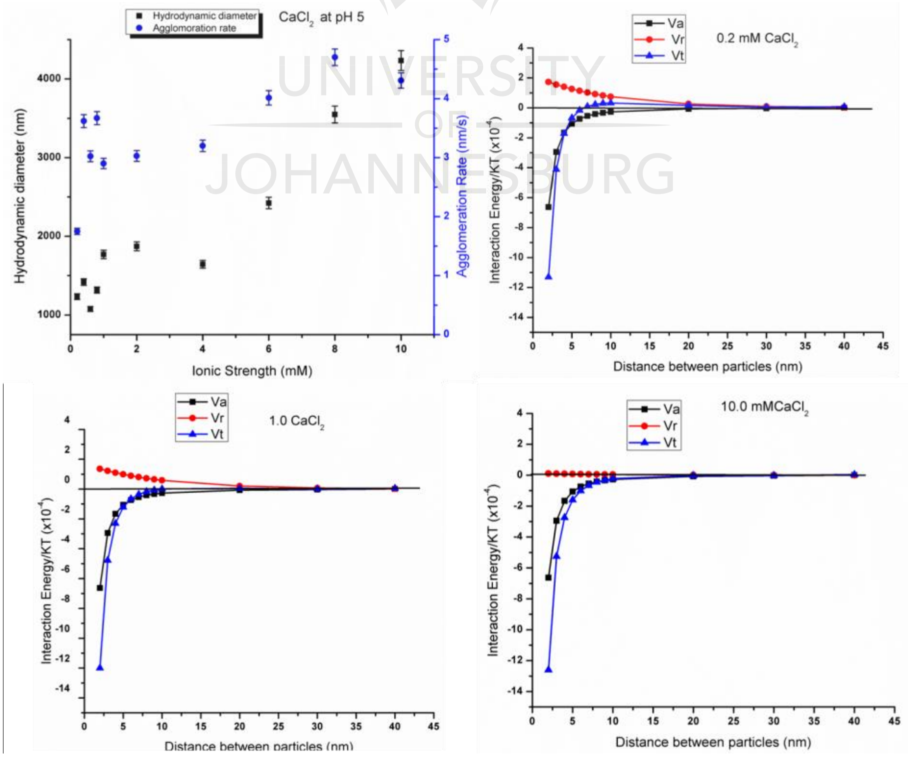

Figure 4.14: Mean diameter and rate of agglomeration and (b) interaction energy plots at 0.2, 1.0 and 10.0 mM $CaCl_2$

The dominance of attractive forces results in agglomerated nanoparticle hence high hydrodynamic diameters are observed in the $MgCl_2$ and $CaCl_2$ suspensions. The observed agglomerate size was double that measured in NaCl, in $MgCl_2$ and almost triple in $CaCl_2$. The rate of agglomeration was also high in both electrolytes suggesting neutralization of the EDL and further reveals that's both Mg^{2+} and Ca^{2+} neutralizes the electric double layer more that the monovalent cation Na^+. The overall interaction energy was generally attractive in both electrolytes. At high ionic strength, Ca^{2+} showed that it compresses the electric double layer to lower energies that the attraction forces which were acting on the particles below 5 nm distance between particles.

The hydrodynamic diameter as a result of Mg^{2+} and Ca^{2+} was found to be generally larger than the one observed at the same pH in DI suspension. Such an increase in the hydrodynamic size can be attributed to the significant compression of the EDL by the divalent ions, by effectively neutralizing the negative surface charge. However, the Mg^{2+} was less effective in neutralizing the EDL as the observed agglomerates were lower compared to Ca^{2+}. This observation was due to the difference in ionic radius difference of the two cations, as Mg^{2+} is smaller than Ca^{2+}. Therefore, as the size of the cations increased their effect on the neutralization of the EDL increased suggesting that both the charge of the cation and size were important in determining their effect on nanoparticles. The observation made on the ionic strength in this study concur with the conclusions made by Romanello, M. B., 2013 that the 0.9 mM concentration of the different salts is high enough to allow agglomeration of nanoparticles yet low enough not to compress the EDL. Thus, the ionic strength (0.9 mM) was then used for the study the stability of *m*-WO_3 in humic acid.

4.4 Effects of valency

The hydrodynamic diameter was observable higher around the point of zero charge. When the mean diameter of the nanoparticle dispersed in DI was compared to that in NaCl, a decrease in size was observed. This shows a relationship between the zeta potential of the material and the mean size. This decrease in size is because of existence of an electrostatic interaction between the chloride ions and the *m*-WO_3 nanoparticles which encouraged the dispersion of the nanoparticles thus smaller sizes observed. Beyond the PZC the nanoparticles were the nanoparticles behave similarly in both DI and NaCl suspension.

The interaction energies were calculated at the extreme pH ranges that are at pH 2 and 10. **Figure 4.15** shows that repulsion forces (V_R) (electrostatic diffuse double-layer repulsions) were dominant in NaCl suspension resulting in a dispersion of nanoparticles hence reduced rates of agglomeration when compared to the DI suspension.

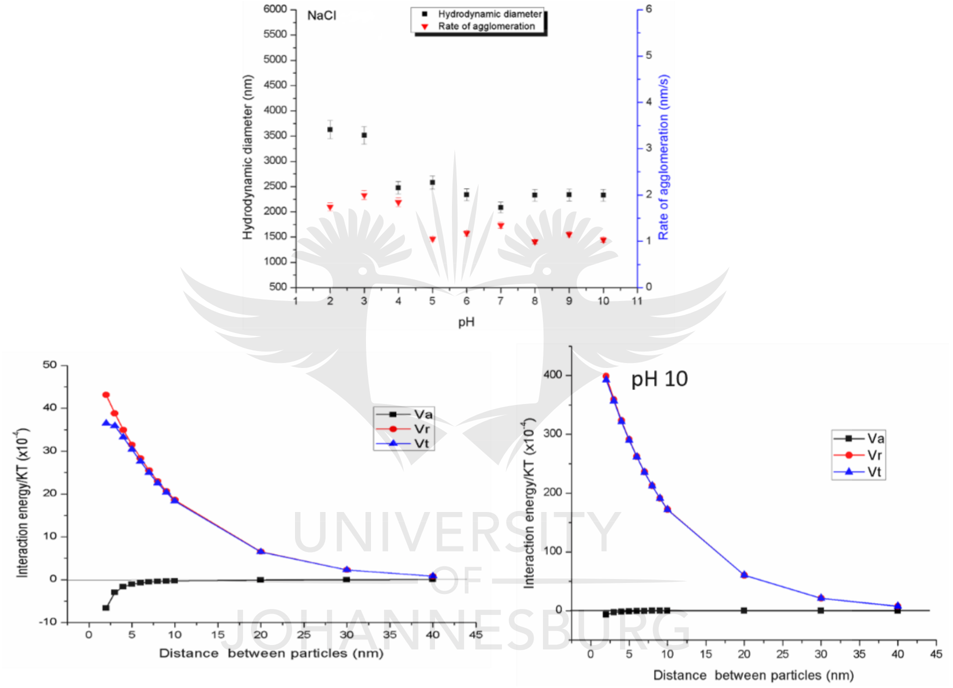

Figure 4.15: (a)Hydrodynamic diameter and rate of agglomeration and (b) interaction energy plots at pH 2, and pH 10 for NaCl

In the divalent cations, both the rate of agglomeration and the mean diameter increased. The highest hydrodynamic diameter continued to be observed around the PZC. The compression of the EDL was clearly demonstrated in the $CaCl_2$ suspension as the hydrodynamic diameter went as far as close to 5000 nm as portrayed in **Figure 4.17(a)**. Both **Figure 4.16** and **4.17** demonstrates the observed mean sizes in the different pH ranges as influenced by $MgCl_2$ and $CaCl_2$ respectively and the calculated interaction energies. The nanoparticles formed smaller agglomerates at pH ranges past the PZC which were bigger though than those in NaCl. This implies that the divalent cations were successful in the compressing the EDL by electrostatic interaction between the negatively charged WO_3 nanoparticles and the cations.

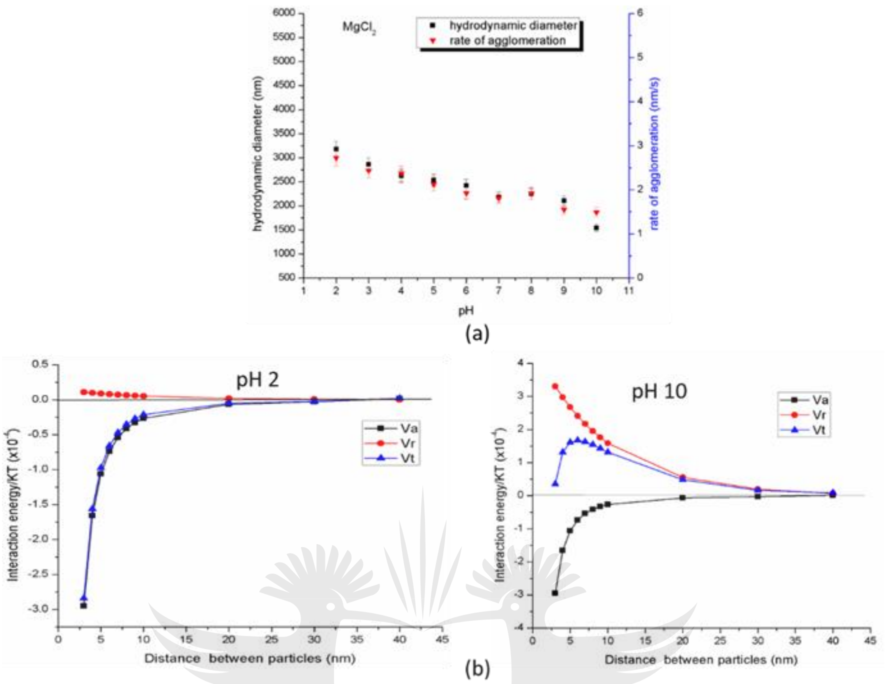

Figure 4.16: (a)Hydrodynamic diameter and rate of agglomeration and (b) interaction energy plots at pH 2, and pH 10 for $MgCl_2$

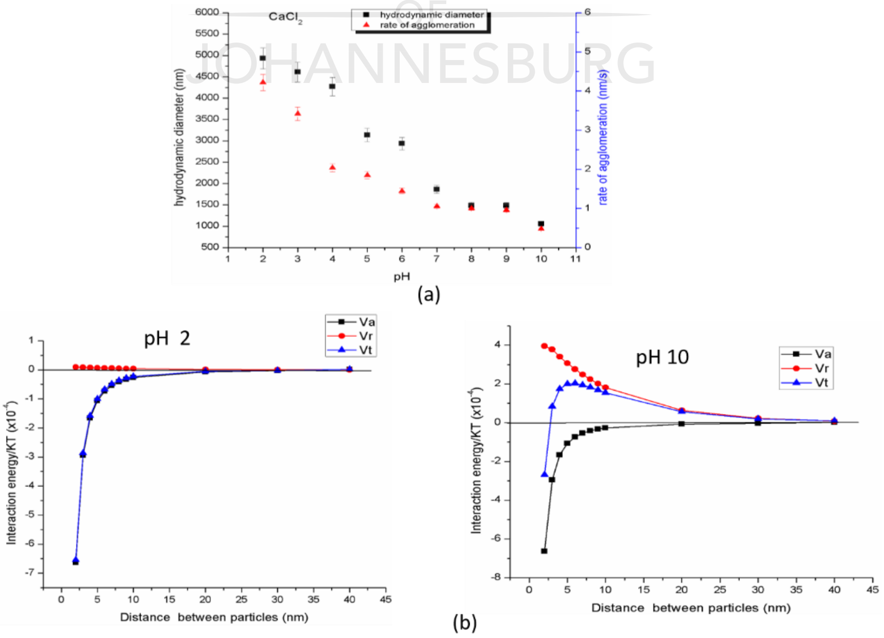

Figure 4.17: (a)Hydrodynamic diameter and rate of agglomeration and (b) interaction energy plots at pH 2, and pH 10 for $CaCl_2$

The DLVO theory calculations as illustrated in **Figure 4.16(b)** and **4.17(b)** shows that the overall interaction energy is attractive. This implies dominance of the van der Waals Attraction (V_A) forces hence supporting the observation of increased rate of agglomeration and hydrodynamic sizes. This observation implies that in the presence of divalent cation WO_3 nanoparticles will tend to form agglomerates. The smaller hydrodynamic diameter observed in $MgCl_2$ compared to those in $CaCl_2$ is mainly due to Mg^{2+} being smaller than Ca^{2+} hence having a reduced potential towards fully compressing the EDL.

4.5 Agglomeration studies in the presence of humic acid

The presence of cation ions (Mg^{2+} and Ca^{2+}) decreased the negative charge of the nanoparticle compared to that of the humic acid and water. The decrease in zeta potential can be assigned to the formation of humic acid-divalent cation bridges as divalent cations are more effective in forming pseudo-micelles. Such interactions are achieved by the electrostatic interaction of the cation with the phenolic and carboxylic groups (de Melo et al. 2015). The interaction results in the neutralization of the humic acid charge. NaCl behaved more similarly to DI suspension, demonstrating that monovalent ions are not efficient in neutralizing the EDL. This data was supported by the observation made on the hydrodynamic diameter in the presence of humic acid in different electrolytes. The effect on the hydrodynamic diameter in the presence of humic acid with increasing cation charge and size is depicted in **Figure 4.18**. The hydrodynamic diameter doubled from 1750 nm in NaCl to 3500 nm in the presence of $CaCl_2$.

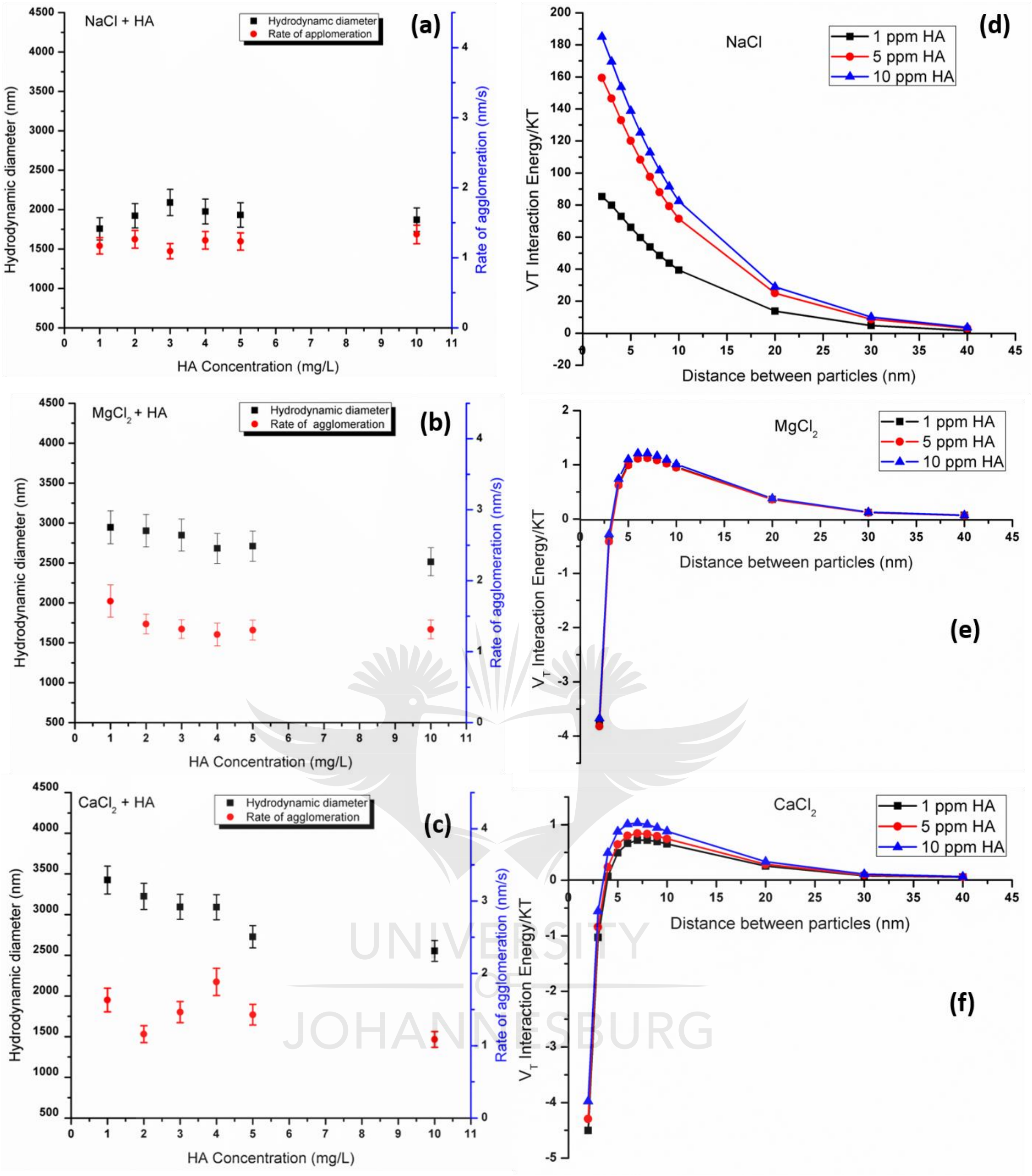

Figure 4.18:(a-c) Hydrodynamic diameter and rate of agglomeration and (d-e) V_T interaction energy plots in different concentrations of humic acid with various electrolytes

In the presence of divalent cations, the mean size decreased with an increase in humic acid concentrations. It was revealed that higher concentrations of humic acid enhanced dispersion and stability of the nanoparticles. The formation of larger agglomerate in the presence of divalent ions even at higher concentrations of humic acid infers that the nanoparticles are mostly likely to be found in sediments rather than in surface water. Moreover, monovalent cations have no significance in the destabilization of nanoparticles in the presence of humic acid suggesting that nanoparticles could migrate for longer distances in surface waters. Increased humic acid concentrations result in an increase in electrostatic diffuse double-layer repulsions forces and hence V_T be repulsive.

Calculations of the interaction energies showed that the overall energy V_T was dominated by, van der Waals Attraction (V_A) forces in both $MgCl_2$ and $CaCl_2$ as illustrated in **Figure 4.18 (d)** to **(e)**. This shows that divalent cation assists WO_3 nanoparticles to agglomerate even in the presence of humic substances. This was in agreement with the observation made with an increased hydrodynamic diameter.

4.6 References

Baalousha, M., 2009. Aggregation and disaggregation of iron oxide nanoparticles: Influence of particle concentration, pH and natural organic matter. *Science of the Total Environment*, 407(6), pp.2093–2101.

Belen, M., Fidalgo, M.M. & Cortalezzi, D., 2013. An experimental study on the aggregation of TiO 2 nanoparticles under environmentally relevant conditions. *Water Research*, 47(12), pp.3887–3898.

Bian, S.W., Mudunkotuwa, I. A., Rupasinghe, T., & Grassian, V. H l., 2011. Aggregation and dissolution of 4 nm ZnO nanoparticles in aqueous environments: Influence of pH, ionic strength, size, and adsorption of humic acid. *Langmuir*, 27(10), pp.6059–6068.

Brunetti, G., Donner, E., Laera, G., Sekine, R., Scheckel, K. G., Khaksar, M., Vasilev, K., De Mastro, G., & Lombi, El., 2015. Fate of zinc and silver engineered nanoparticles in sewerage networks. *Water research*, 77, pp.72–84.

Chekli, L., Zhao, Y. X., Tijing, L. D., Phuntsho, S., Donner, E., Lombi, E., Gao, B. Y., & Shon, H. K., 2014. Aggregation behaviour of engineered nanoparticles in natural waters: Characterising aggregate structure using on-line laser light scattering. *Journal of Hazardous Materials*, 284, pp.190–200.

Daniel, M.F., Desbat, B., Lassegues, J. C., Gerand, B., & Figlarz, M., 1987. Infrared and Raman study of WO_3 tungsten trioxides and WO_3, xH_2O tungsten trioxide tydrates. *Journal of Solid State Chemistry*, 67(2), pp.235–247.

Fenglin Liu, Xianjie Chen, Qinghua Xia, Lihong Tian, X.C., 2015. Ultrathin tungsten oxide nanowires: oleylamine assisted nonhydrolytic growth, oxygen vacancies and good photocatalytic properties. *RSC Adv.*, (5), pp.77423–77428.

Ghosh, S., Acharyya, S. S., Kumar, M., & Bal, R., 2015. One-pot preparation of nanocrystalline Ag–WO_3 catalyst for the selective oxidation of styrene. *RSC*

Adv., 5, pp.37610–37616.

Gomez, C., Martínez, D.S. & Torres-martínez, L.M., 2013. Facile synthesis of -WO_3 powders via precipitation in ethanol solution and evaluation of their photocatalytic activities. *Journal of Photochemistry and Photobiology A: Chemistry*, 262, pp.28–33.

Gotić, M., Ivanda, M., Popović, S., & Musić, S., 2000. Synthesis of tungsten trioxide hydrates and their structural properties. *Materials Science and Engineering B: Solid-State Materials for Advanced Technology*, 77(2), pp.193–201.

Huang, J., Xu, X., Gu, C., Yang, M., Yang, M., &L iu, J., 2011. Large-scale synthesis of hydrated tungsten oxide 3D architectures by a simple chemical solution route and their gas-sensing properties. *Journal of Materials Chemistry*, 21(35), pp.13283–13289.

Li, Y.,Yang, C., Guo, X., Dang, Z., Li, X., & Zhang, Q., 2015. Effects of humic acids on the aggregation and sorption of nano-TiO_2. *Chemosphere*, 119, pp.171–176.

Luévano-hipólito, E., Cruz, A M., Yu, Q L., Brouwers, H. J. H., 2014. Precipitation synthesis of WO_3 for NO_x removal using PEG as template. *Ceramics International*, 40, pp.12123–12128.

Mahlalela, L.C., Ngila, J.C. & Dlamini, L.N., 2016. Characterization and stability of TiO_2 nanoparticles in industrial dye stuff effluent. *Journal of dispersion science and technology*, 38(4), pp.584-593

Marei, N.N., Nassar, N.N. & Vitale, G., 2016. The effect of the nanosize on surface properties of NiO nanoparticles for the adsorption of Quinolin-65. *Physical chemistry chemical physics : PCCP*, 18(9), pp.6839–49.

Martin, C., Martin, I., Rives,V., Solana, G., Loddo, V., Palmisano, L., Sclafani, A., ., 1997. Physicochemical characterization of WO_3/ZrO_2 and WO_3/Nb_2O_5 catalysts and their photoactivity for 4-nitrophenol photooxidation in aqueous dispersion. *Journal of Materials Science*, 32, pp.6039–6047.

Martínez, D.S., Cruz, A.M. & Cuéllar, E.L., 2011. Photocatalytic properties of WO3 nanoparticles obtained by precipitation in presence of urea as complexing agent. *Applied Catalysis A: General*, 398, pp.179–186.

de Melo, B.A.G., Motta, F.L. & Santana, M.H.A., 2015. Humic acids: Structural properties and multiple functionalities for novel technological developments. *Materials Science and Engineering C*, 62, pp.967–974.

Pakrashi, S., Dalai, S., Sneha, B., Chandrasekaran, N., & Mukherjee, Al., 2012. A temporal study on fate of Al_2O_3 nanoparticles in a fresh water microcosm at environmentally relevant low concentrations. *Ecotoxicology and Environmental Safety*, 84, pp.70–77.

Pang, H.F., Xiang, X., Li, Z., Fu, Y., & Zu, X., 2012. Hydrothermal synthesis and optical properties of hexagonal tungsten oxide nanocrystals assisted by ammonium tartrate. *Physica Status Solidi (a)*, 209(3), pp.537–544.

Sing, K.S.W., 1982. Reporting Physisorption data for gas/solid Special Reference to the Determination of Surface Area and Porosity. *Pure & Appl. Chem.*, 54(11), pp.2201–2218.

Vamvasakis, I., Georgaki, I., Vernardou, D., Kenanakis, G.,& Katsarakis, N., 2015. Synthesis of WO_3 catalytic powders: evaluation of photocatalytic activity under NUV/visible light irradiation and alkaline reaction pH. *Journal of Sol-Gel Science and Technology*, 76(1), pp.120–128.

Wall, N.A. & Choppin, G.R., 2003. Humic acids coagulation: Influence of divalent cations. *Applied Geochemistry*, 18(10), pp.1573–1582.

Weinberg, H., Galyean, A. & Leopold, M., 2011. Evaluating engineered nanoparticles in natural waters. *TrAC - Trends in Analytical Chemistry*, 30(1), pp.72–83.

Zhang, Y., Zhang, Y., Chen, Y., Westerhoff, P., & Crittenden, J., 2009. Impact of natural organic matter and divalent cations on the stability of aqueous nanoparticles. *Water Research*, 43(17), pp.4249–4257.

Zhu, M., Wang, H., Keller, A. A., Wang, T., & Li, F., 2014. The effect of humic acid on the aggregation of titanium dioxide nanoparticles under different pH and ionic strengths. *Science of the Total Environment*, 487(1), pp.375–380.

CHAPTER 5

THE FATE, BEHAVIOUR, AND EFFECT OF WO_3 NANOPARTICLES ON THE FUNCTIONALITY OF AN AEROBIC TREATMENT UNIT *

** Part of the work presented in this chapter has been submitted for publication in a peer-reviewed journal.*

5.1 Introduction

Natural organic matter (NOM) a constituent of wastewater and other biomass have been reported to adsorb on the nanoparticles surfaces thus enhancing their stability (Zhang et al. 2009). Humic acid, an example of NOM has been reported to stabilize nanoparticles even at every low concentration and it also plays a pivotal role in the fate and transportation of pollutants (Zhu et al. 2014; Li et al. 2015). Thus, understanding the impact of humic acid on the stability of *m*-WO_3 nanoparticles in a WWTP is crucial. Increased attention have been given to understanding the fate and behaviour of nanoparticles due to their potential environmental application.

Monoclinic tungsten trioxide is a promising photocatalyst for the degradation of organic pollutants especially dyes and it is the most stable phase of *m*-WO_3 at room temperature (Zheng et al. 2011). Hence it is most likely to be applied in the wastewater treatment processes. However, it is of vital importance that its fate and behaviour be fully understood to avoid exposure to the environment. The Organisation for Economic Co-operation and Development (OECD) 303A (2001) guidelines has been formulated to provide the minimum test protocol for the identification of hazard nanoparticles (Burkart et al. 2015). Thus, in this work, we seek to understand how WO_3 nanoparticles will affect the functionality of the biological wastewater treatment plant assembled following the OECD guidelines by monitoring COD, BOD_5, TDS, and conductivity while determining the fate and behaviour of the nanoparticles.

5.2 Stability of *m*-WO_3 NPs in synthetic domestic sewage

The prepared *m*-WO_3 nanoparticle suspension was sampled and had their stability tested. This was achieved using dynamic and electrophoretic light scattering. The prepared suspension had an average zeta potential of -11.7±0.3 mV with an average hydrodynamic diameter of 1.898±0.0686 µm at a pH range between 7 to 8. The suspensions were also analysed for a period of 36 hours to a week to determine their stability against time. The results are depicted in **Figure 5.1** which shows that with time, the negativity of the zeta potential increase thus resulting in decrease hydrodynamic size due to increased repulsion forces between nanoparticles induced by the humic acid. Thus, the humic acid present in the influent managed to keep the agglomeration of the nanoparticles at a minimum as reported by Simelane et al., (2017).

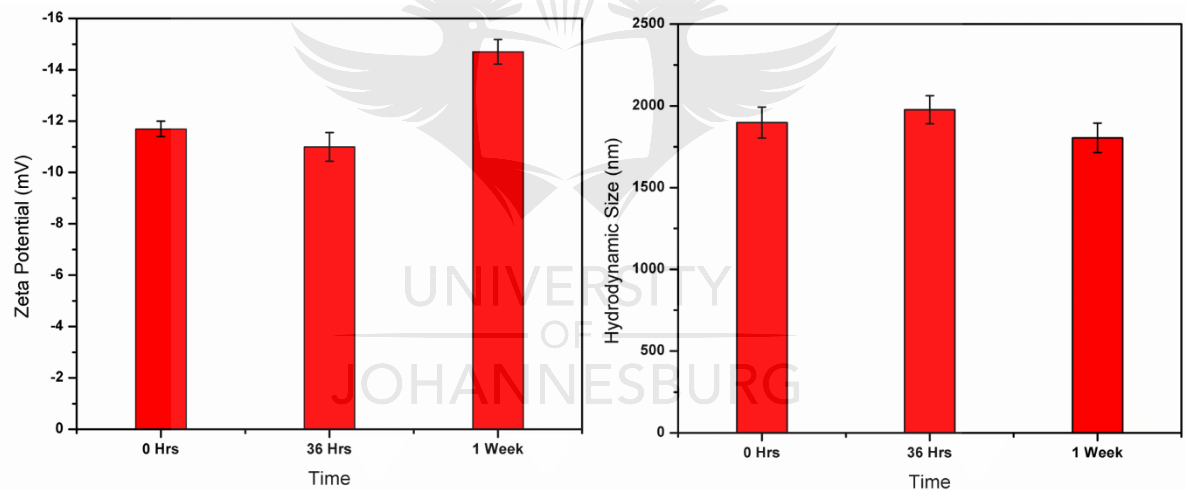

Figure 5.1: Dynamic and electrophoretic light scattering measurements of zeta potential (left) and size(right) of *m*-WO_3 suspension in synthetic influent.

5.3 Acclimatization of the Activated sludge in the SWTP

Upon inoculation of the treatment system, COD was used to monitor the functionality of the WWTP. In both the test and reference unit, COD removal showed an increase from 68% to more than the required 80%. **Figure 5.2** illustrates SRT 2 and SRT 3 had a good removal efficiency suggesting that the microorganisms responded well to the changes in the constituents of the influent from 50:50 raw sewage and synthetic sewage to 30:70. However, upon introduction of the 100% synthetic influent, the removal was reduced to below the required 80%. The dip is mainly due to the microorganisms acclimatizing on the 100% synthetic influent being fed to them. This resulted in reduced contact time between the biodegradable materials and the microorganisms in the sludge hence reduced the efficiency of the treatment system. A steady state was observed between day 28 and 49 with the average removal efficiency of COD for the control set at 86.5 % and that of the test at 87.5%. The presence of humic acid in the synthetic effluent had no effect on the COD removal efficiency as acclimatization of the flocs occurred successfully. This could be attributed to the fact that humic acid is a major constituent of domestic wastewater thus the inoculum was already acclimatized to it from the wastewater treatment plant obtained (Chaúque et al. 2014).

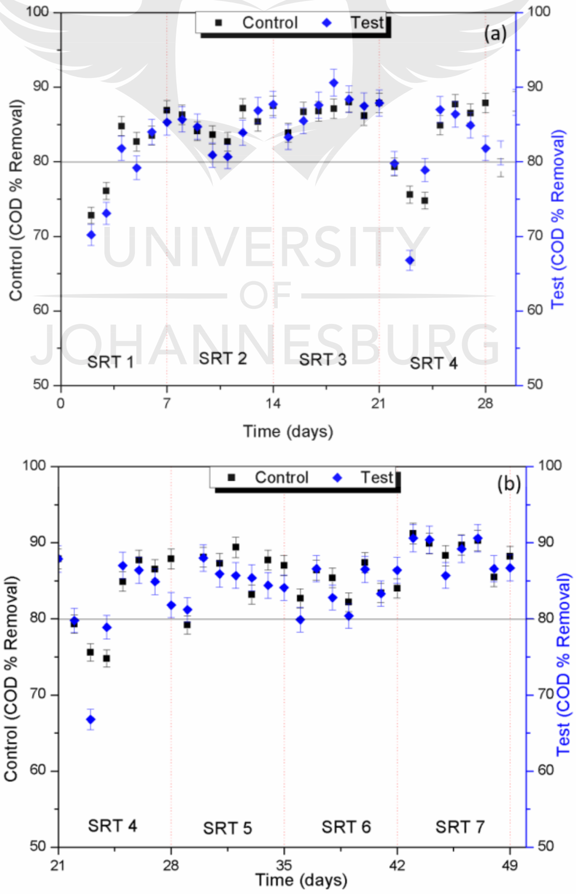

Figure 5.2: Chemical oxygen demand (COD) removal efficiency in the simulated wastewater treatment plant during acclimatization and steady state.

Moreover, the temperature in the aeration chambers was maintained at an average of 23˚C for both test and control unit which was within the OECD guidelines working range of 20-25˚C (OECD 303A guidelines, 2001). Dissolved oxygen was kept above 2 mgL^{-1} for the optimum survival of the flocs. The DO concentration maintained such that it was neither too high or too low. A low concentration of DO in the aeration chamber results in the outgrowth of filamentous bacteria which are not essential for the activated sludge process, yet at high concentrations results in improper settling of the flocks in the clarifiers (Ahansazan et al. 2014).

5.4 Analyses of WO_3 in sludge

The EDS analysis of the dried sludge for both the control and test units is as demonstrated in **Figure 5.3**. Several primary elements were present including carbon, oxygen, magnesium, calcium and iron which are present in both tests units, which arise from the activated sludge and the chemicals used during the treatment process. The resulting tungsten peaks appeared in the test sludge showing evidence of the spiked nanoparticles. The observation of the tungsten peak was then confirmed using elemental mapping as depicted in **Figure 5.4**. The SEM mapping micrographs revealed that the tungsten, as well as the other elements, were evenly distributed.

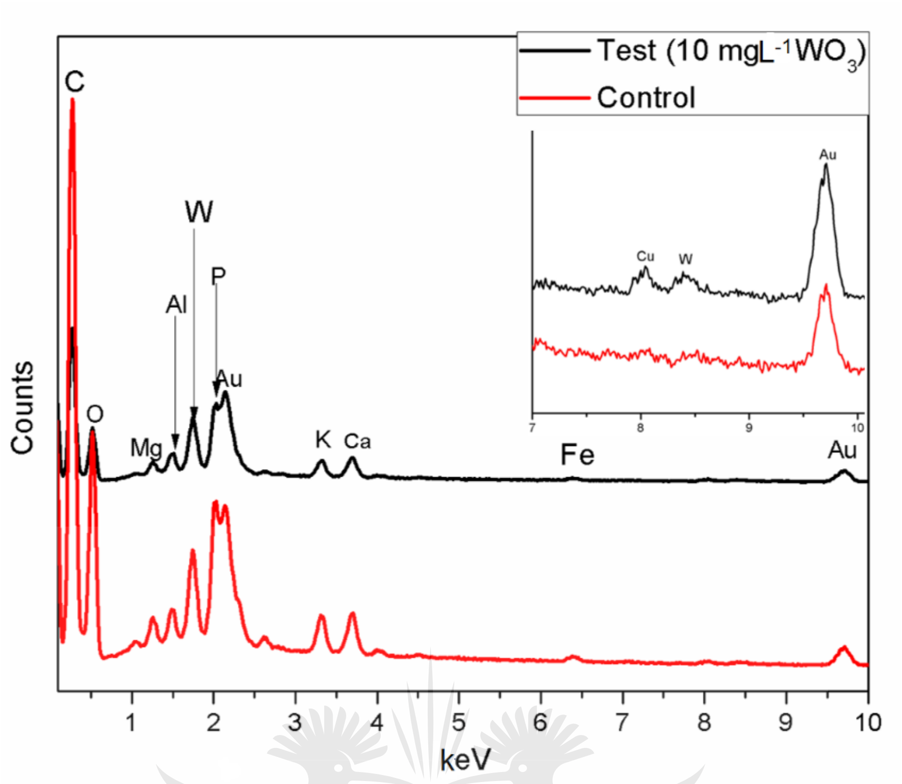

Figure 5.3: EDS analysis of the activated sludge in the control and *m*-WO_3 spiked test units.

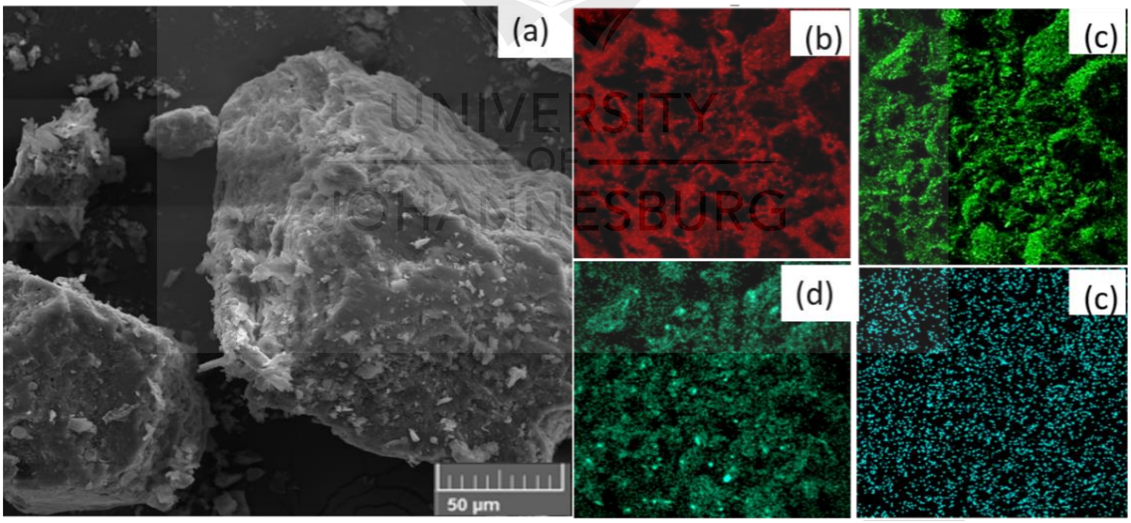

Figure 5.4: (a) SEM image of dried the sludge during the addition of 15 mgL^{-1} *m*-WO_3 with the respective inserts of (b) carbon, (c) oxygen, (d) silicon and (e) tungsten after SEM mapping of the image.

The sludge originating from the control test depicted in the PXRD patterns in **Figure 5.5**, revealed the absence of tungsten, but peaks associated to carbon (002) and SiO2. Peaks attributed to SiO_2 with a hexagonal crystal structure referenced to ICDD card no. 01-087-2096 with (011), (314) and (143) indices. The presence of the SiO_2 is supported by several authors who reported it to be found in sludge ash including other metal oxides such as TiO_2, Al_2O_3, and Fe_2O_3 (Lynn et al. 2015; Magdziarz et al. 2016).

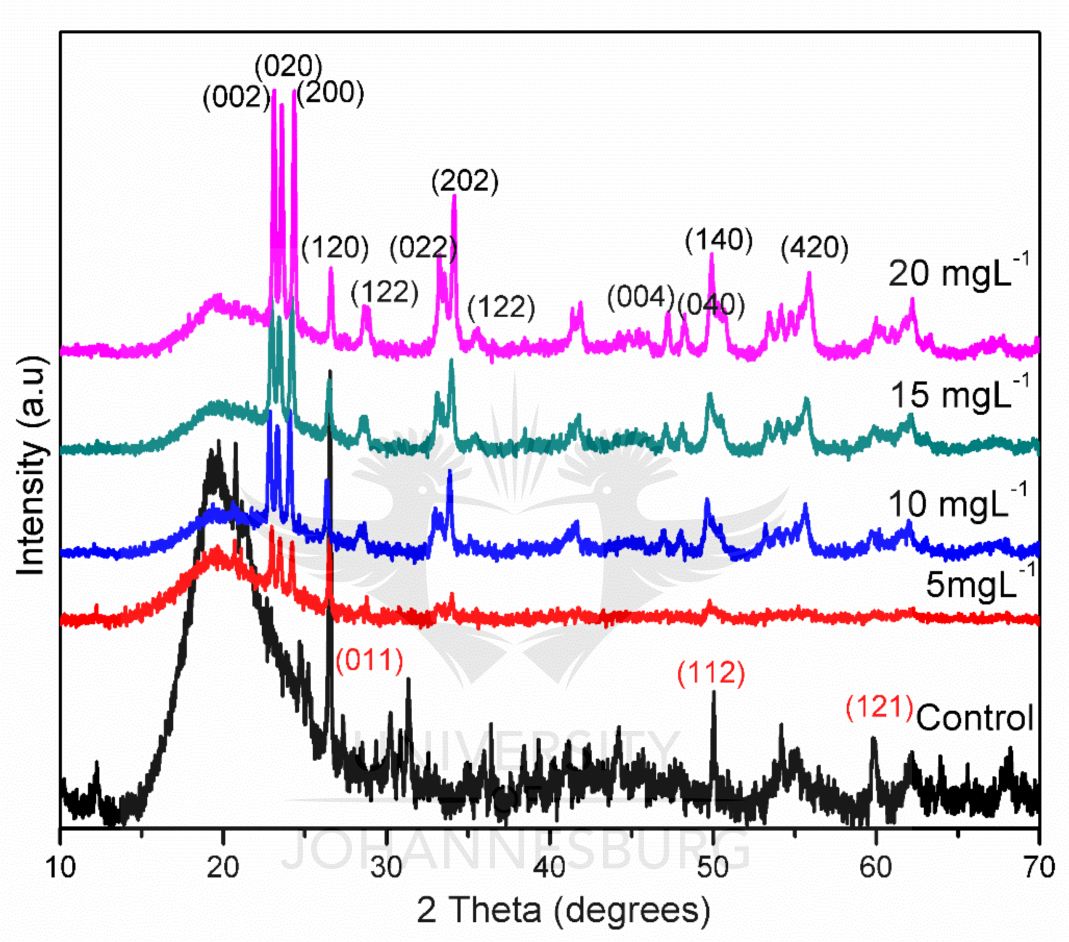

Figure 5.5: **P**XRD patterns of the dried sludge exposed to wastewater spiked with different concentrations of *m*-WO_3 NPs

Furthermore, PXRD patterns of the sludge between day 49 and 56 with 5 mgL^{-1} *m*-WO_3 nanoparticles spiked into influent Showed *m*-WO_3 peaks with low intensity. Moreover, addition of 10 mgL^{-1} of *m*-WO_3 NPs in the influent wastewater, the presence of *m*-WO_3 in the sludge was detected with the observation of (002), (020), (200), (120), (112), (022), (202), (122), (004), (040), (140), and (420) indices respectively with the peaks intensity increasing as spiked concentrations increased to 20 mgL^{-1} as illustrated in **Figure 5.5**.

These patterns confirmed the existence of the monoclinic polymorph of *m*-WO_3 in the sludge referenced to ICDD: 04-015-0122. This is evident that the activity of the activated sludge did not alter the nature of the polymorph of WO_3 as sharp peaks appeared in the PXRD patterns which are indicative of the crystallinity of the *m*-WO_3 in sludge. A similar observation was made by Chauque at al. (2016), who reported that the Activated sludge had no effect on the crystallinity of ZnO nanoparticles. The crystal size was computed using Scherrer's formula and the XRD data:

The obtained crystalline size was 15±0.15 nm of *m*-WO_3 in sludge which is comparable to that of the pristine *m*-WO_3 spiked into the influent.The presence of the *m*-WO_3 NPs in the sludge was further confirmed in TEM. The morphology of the NPs observed closely resembled that of the pristine WO_3 shown in **Appendix A** as both spherical and irregular shapes were observed as illustrated in **Figure 5.6** confirming that the activated sludge had no effect on the morphology of the NPs.

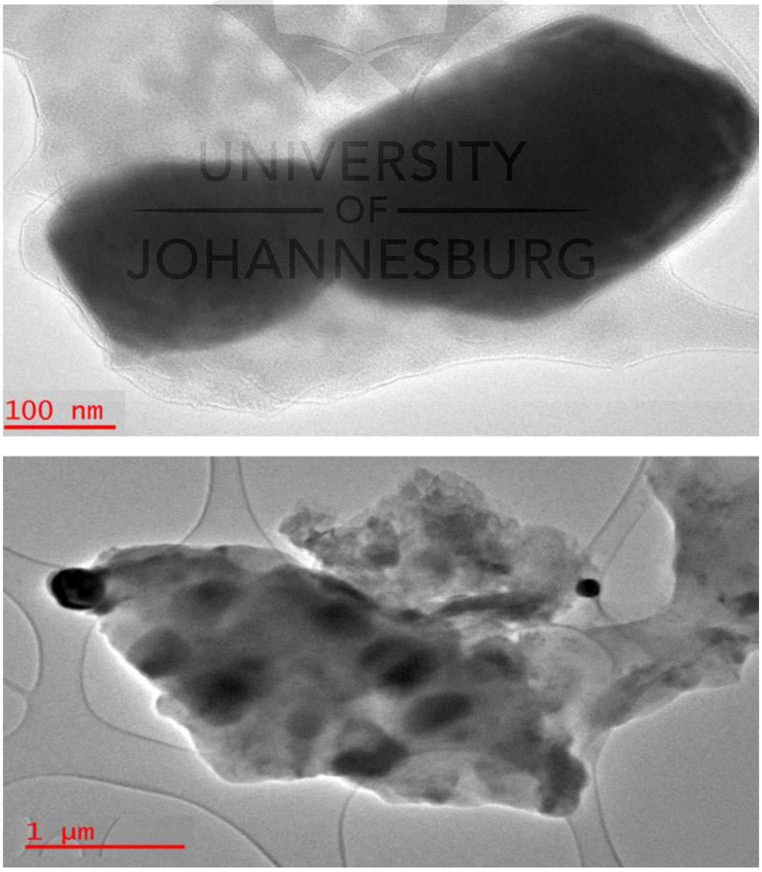

Figure 5.6: TEM images of the test unit dried sludge

5.5 The impact of *m*-WO_3 NPs on treatment plant functionality

The effect of the WO_3 nanoparticles was monitored by assessing both COD and BOD_5 removal efficiency in the SWTP. Upon successful acclimatization, gradual addition of *m*-WO_3 was added beginning with 5 mgL^{-1} to the synthetic influent and pumped into the test aeration unit. The COD removal efficiency was still comparable to the reference unit as both showed to be above 80%. A similar observation was made in SRT 9 where 10 mgL^{-1} NPs was added and the removal efficiency was greater than 80% by 2% as depicted in **Figure 5.7** demonstrating that the NPs had no effect on the functionality of the treatment plant. The OECD guidelines (2001) stipulates that a removal efficiency >80% shows adequate biodegradation of organic matter. The COD removal further decreased by 8% when 15 mgL^{-1} was added. Precipitously, the COD fell to 62% when 20 mgL^{-1} was added to the synthetic influent. The effluent COD values observed in SRT 10 and 11 do not meet South African regulations for discharge into the main streams which require a maximum of 75 mgL^{-1} (Department of water affairs 2010).

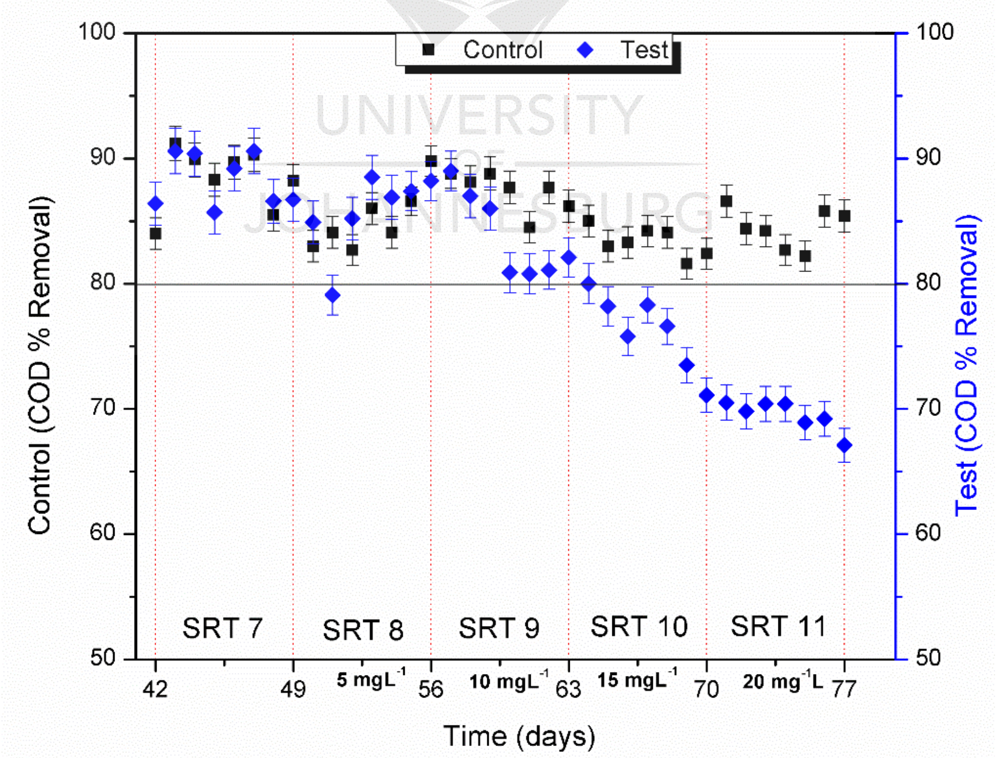

Figure 5.7: COD removal efficiency after addition of *m*-WO_3 nanoparticles

Measurements of BOD_5 in **Figure 5.8** had a similar correlation trend to the data obtained from COD. At SRT 10 and 11, the BOD_5 was significantly different from the test unit compared to the control which showed a removal of over 85%. This infers that at concentrations greater than 15 mgL^{-1} the nanoparticles tend to inhibit the respiration in the activated sludge (Zhou et al. 2015). Thus, the decrease in both the COD and BOD_5 could be attributed to the nanoparticles being adsorbed to the surface of the activated sludge (microorganisms) consequently reducing the rate of respiration. This is supported by work done by Zhou et al., 2015, who investigated how engineered nanoparticles impact the activated sludge in wastewater treatment reported that oxygen flux decreased greatly after the sludge have been exposed to various concentrations of nanoparticles (ZnO and TiO_2) for 4.5 hours.

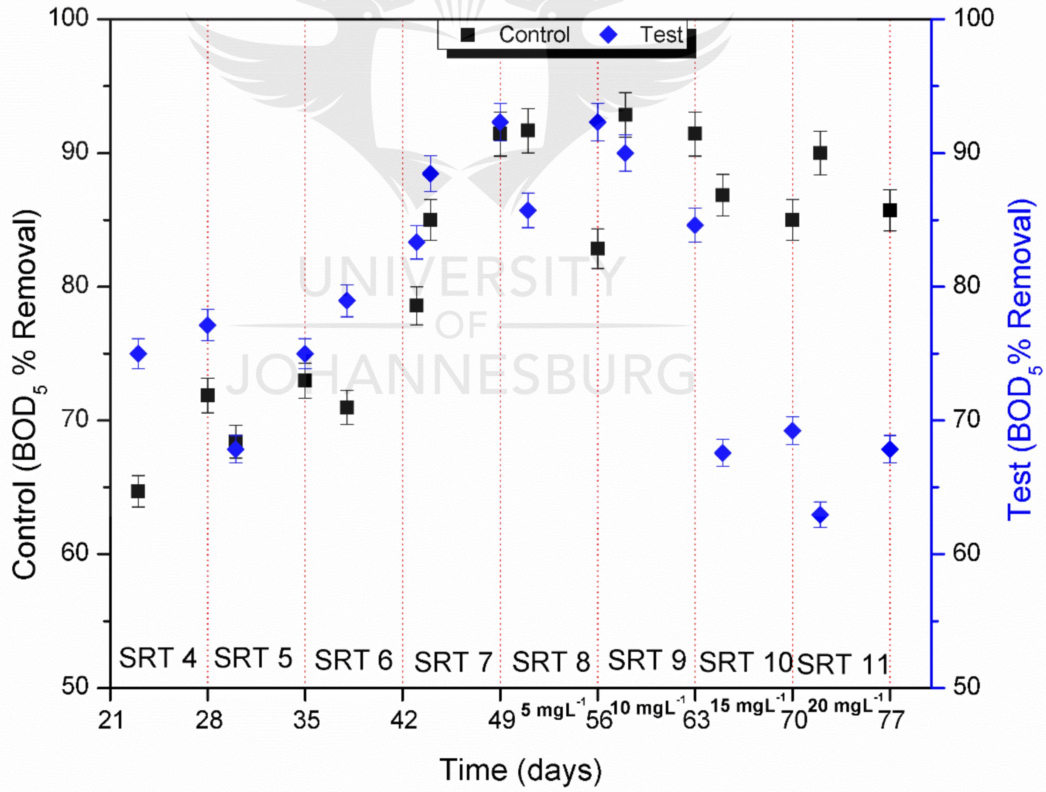

Figure 5.8: BOD_5 removal before and after addition of *m*-WO_3 nanoparticles

Of note, the conductivity measurements of the effluent samples from the test unit were increasing as the concentration of added nanoparticles increased. These were from 764.9 µS/cm with 5 mgL^{-1} *m*-WO_3 to 846.9 µS/cm with 20 mgL^{-1} while that of the control was maintained at around 750 µS/cm. The TDS followed a similar observation as illustrated in **Table 5.1**. The increase in both conductivity and TDS may be ascribed to the possible dissolution of W from WO_3 nanoparticles during the treatment process in the aeration units. Studies conducted on the dissolution of WO_3 revealed that WO_3 readily dissolute in an aqueous medium with pH>4 (Liu et al. 2011; Anik & Cansizoglu 2006). It thus infers that m-WO_3 nanoparticles would readily dissolute in both surface waters and wastewater as their pH ranges between 5-9. The presence of the W in the effluent is cause for concern as it indicates that tungsten could find its way to the main rivers through the discharge of the effluent. Strigul et al. 2009, reported that tungsten influences the early stages of fish development implying that even though small concentrations are released, bioaccumulation of this metal could be a great threat to marine organisms (Strigul et al. 2009). The pH measurements for both the control and test units were between 6.5 - 7.5 as tabulated in Table 2. Therefore, *m*-WO_3 will dissolute during the treatment process as these pH >4 hence the increase in conductivity of the effect in the test.

Table 5.1: Monitored parameters in aeration tanks and effluents during the addition of nanoparticles.

Parameters	**5 mgL^{-1} WO$_3$ (Day 50-56)**		**10 mgL^{-1} WO$_3$ (Day 57-63)**		**15 mgL^{-1} WO$_3$ (Day 64-70)**		**20 mgL^{-1} WO$_3$ (Day 71-77)**	
	Mean	SD	Mean	SD	Mean	SD	Mean	SD
Control								
pH	7.2	0.1	7.4	0.2	7.2	0.2	7.1	0.2
DO (mgL^{-1})	4.1	0.33	4	0.25	3.8	0.3	3.7	0.3
Temperature (˚C)	24	0.9	22.9	0.8	22.9	0.5	23.1	0.5
Conductivity (µS/cm)	753.8	45.4	749.7	38.4	756.4	20.9	743.7	64.2
TDS (mgL^{-1})	371.8	24.3	373.3	11.6	385.8	16.9	361.2	16.8
MLSS (mgL^{-1})	1511.3	73.8	1596.3	121.3	1585	30	1601.2	31.4
MLVSS (mgL^{-1})	1302.5	52.5	1378.8	101.3	1357.5	53	1405	27.5
COD (mgL^{-1})	58.9	7.4	60.9	9.4	67.6	4.3	62.8	4
TSS (mgL^{-1})	8.1	2.67	7.1	1.72	8.6	2.51	7.8	2.60
BOD$_5$ (mgL^{-1})	0.45	0.15	0.3	0.1	0.4	0.1	0.3	0.1
Test								
pH	7.2	0.2	7	0.1	6.8	0.1	6.9	0.1
DO (mgL^{-1})	4.1	0.18	4.2	0.22	3.7	0.17	3.8	0.3
Temperature (˚C)	24.1	0.6	23	0.7	22.9	0.5	22,9	0.4
Conductivity (µS/cm)	764.9	56.6	811.7	49.2	822.3	34.9	846.9	32.4
TDS (mgL^{-1})	379.8	39.1	426.8	16.4	431.1	17.9	444.6	13
MLSS (mgL^{-1})	1816.3	243.8	1805	307.5	1753.8	140.6	1603.8	29.4
MLVSS (mgL^{-1})	1515	157.5	1468.8	278.8	1352.5	158.8	1123.7	18.9
COD (mgL^{-1})	63.7	7.4	74.3	18	102	9.7	121.1	1.4
TSS (mgL^{-1})	7.0	1.76	7.1	1.84	12.6	2.70	12.9	3.21
BOD$_5$ (mgL^{-1})	0.5	0.2	0.45	0.15	1.0	0.2	0.95	0.05
SD: Standard Deviation								

The ratio of MLVSS to MLSS (MLVSS/MLSS) was also used to monitor the survival of the flocs in the aeration chambers. According to Fan J. et. al 2015, the ratio of MLVSS/MLSS should be greater 0.75 in a conventional wastewater treatment system (Fan et al. 2015; Wentzel et al. 2002) as it is an indicator of the concentration of the microorganisms constituted in the activated sludge. It is evident that the MLSS were mostly organic matter signifying the population of the microbes in the mixed liquor of the aeration tanks. In the control test, the observed ratio for MLVSS/MLSS was much greater than the expected 0.75 in conventional wastewater treatment system mainly because of the use of synthetic sewage which contained less suspended solids.

In this simulation, the ratios were found to be 0.83 (5 mgL^{-1} *m*-WO_3 added), 0.81 (10 mgL^{-1} WO_3 added), 0.77 (15 mgL^{-1} WO_3 added) and 0.70 (20 mgL^{-1} WO_3 added) for the test unit. The control unit also showed comparable ratios which were 0.86, 0.86, 0.85 and 0.88) (SRT 8, SRT 9, SRT 10 and SRT 11 respectively). The addition of humic acid in the synthetic influent provided an increased concentration of the organic material hence more food for the flocs. However, in the test unit, the ratio showed a decrease of MLVSS/MLSS ratio as the concentration of nanoparticles added increased implying that the MLSS were now containing more suspended solids which were mostly not organic in their nature. This observation complements both the SEM-EDS and mapping results which showed the presence of elemental tungsten which possible exited still in nanoparticle form.

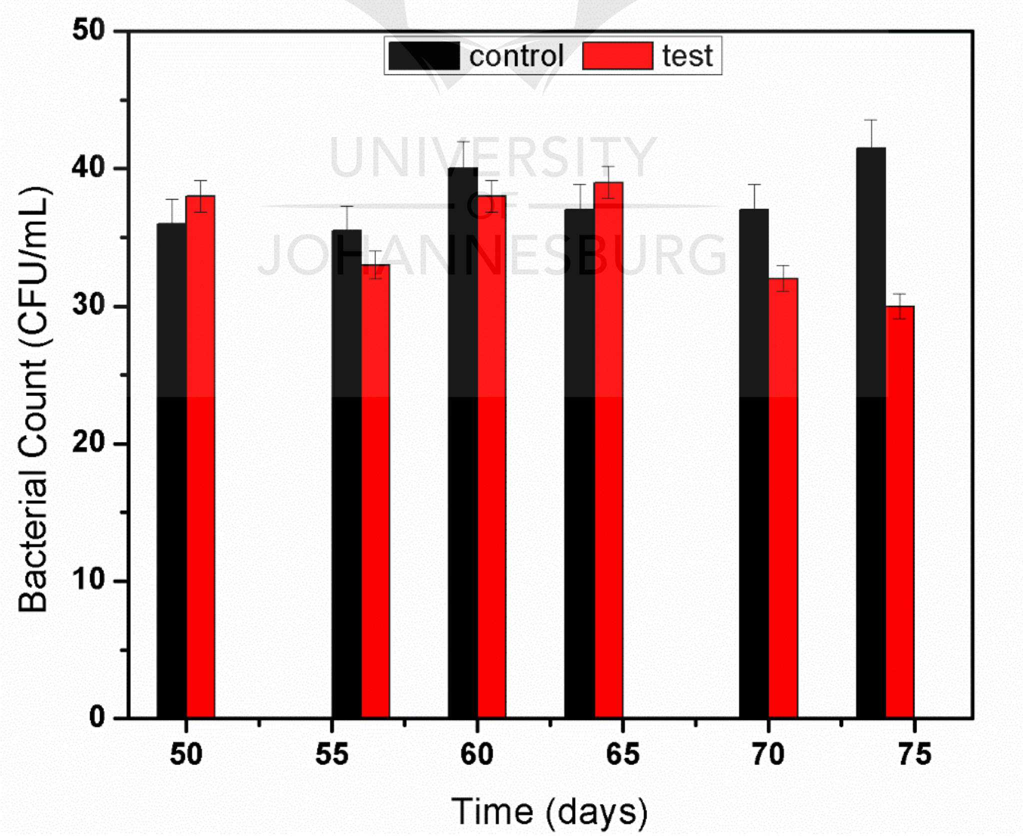

Figure 5.9: Total plate count of both aeration units indicating microbial population

The observation made with the MLVSS/MLSS ratio as indicative of the level of microorganism was further confirmed with the TPC method. The TPC method revealed that the amount of bacteria in the control aeration chamber were comparable throughout the experiment as shown in **Figure 5.9**. However, for the test unit, a decrease in the number of bacteria was observed after day 63 when 15 mgL^{-1} WO_3 was added. The decrease in the bacterial count after day 55 and then an increase could be due to the microorganism acclimatized in the 10 mgL^{-1} concentration of nanoparticles that was being spiked in the system. This decrease concurred with the COD removal efficiency data which showed a reduction in the COD removal efficiency which was ascribed to the decrease in the population of microorganisms in the aeration vessel. Furthermore, the TSS showed a drastic increase in the test effluent further confirming that the nanoparticles influenced the functionality of the treatment plant. The decrease in continuous decrease in colony forming bacteria could be due to either the death of microorganisms caused by the introduction of the nanoparticles. Secondly, the nanoparticles could have been responsible for the prolonged rate of settable solids observed in the test clarifier. Due to the poor settling rate, this resulted to a reduced RAS, for the sludge was eluted as suspended solids, consequently increasing the content of suspended solid in both SRT 10 and 11.

5.6 Distribution of *m*-WO_3 NPs in the WWTP

Knowledge on how the nanoparticles are distributed in the treatment plant or rather removed by the activated sludge process is of vital importance. Hence the concentration of the W in the sludge and effluent were compared to further compliment the results observed in the EDS and Mapping in SEM which showed the presence of W. **Figure 5.10** demonstrated a high correlation of 0.86 between the concentration of W in the sludge and effluent. About 80% the W was found to be in the sludge while only 20 to 21% m/m in the effluent. This observation suggested that the activated sludge treatment process could be used to remove W from wastewater.

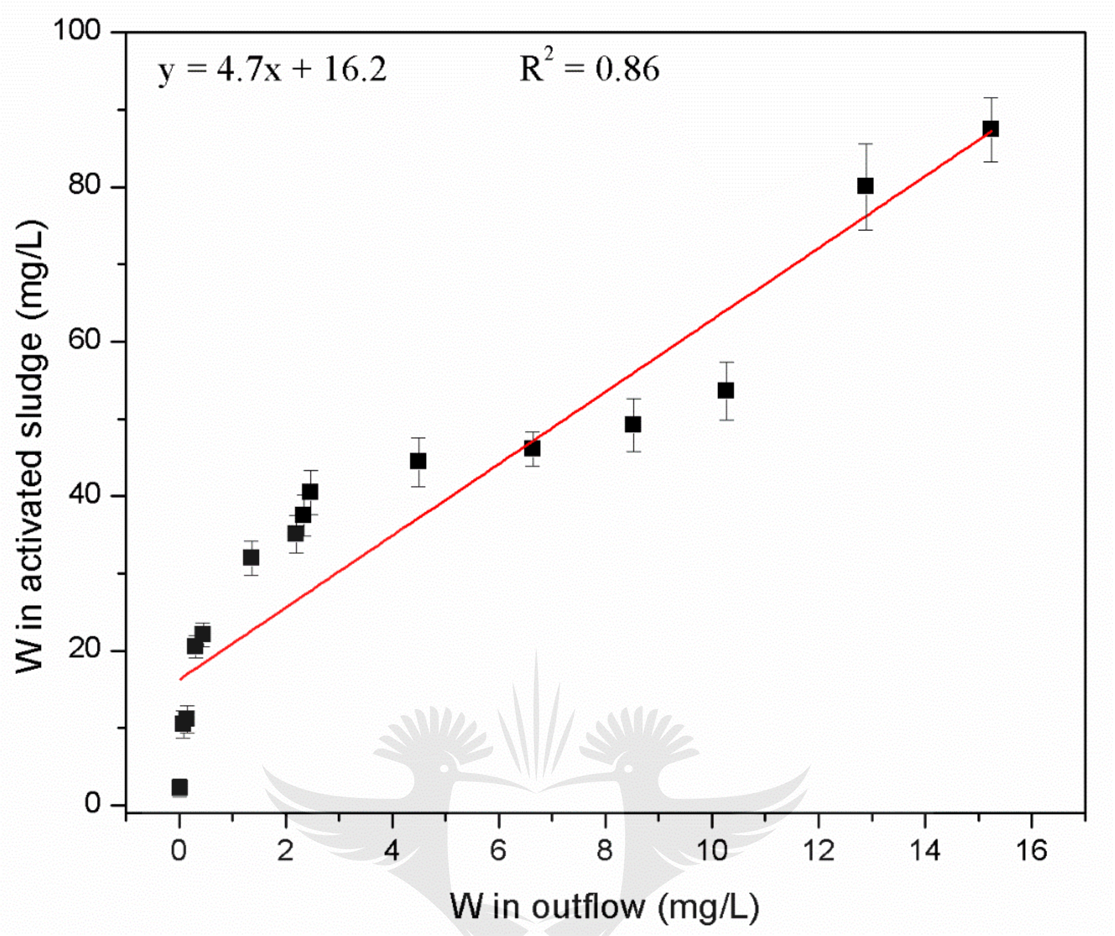

Figure 5.10: Correlation of W in activated sludge and effluent

The 20% m/m found in outflow could be accounted by considering sorption on the surface of the suspended solids found in the effluent. This was supported by a study conducted by Puay N. et. al 2015 who reported that sorption was the main route for the removal of ZnO nanoparticles in wastewater thus higher concentrations of ZnO in the activated sludge than in the effluent (Puay et al. 2015).

Several studies have reported varying efficiencies on the removal of nanoparticles in wastewater. For example, research done on the similar or other types of materials have shown variations in the removal efficiency of the nanoparticles. For example, Gomez-Rivera et al., 2012 reported 96% removal of CeO_2, while Gartiser et al., 2014 >95% of TiO_2 (Gómez-Rivera et al. 2012; Gartiser et al. 2014). Furthermore, a study conducted in a full-scale wastewater treatment plant reported

74 to 85% m/m removal of the Ti found in the influent (Shi et al. 2016). These variations could be ascribed to the differences in the surface properties of nanoparticles and the chemistries as they interact with the wastewater which also differs in constituent components (Chaüque et al. 2016). Thus, the 80% reported in this work could be due to the humic acid present in the synthetic influent which reduces the agglomeration of WO_3 nanoparticles and hence increase dispersion thus also increasing the likelihood of nanoparticles being found in the effluent.

5.7 References

Ahansazan, B., Afrashteh, H., Ahansazan, N. & Ahansazan, Z., 2014. Activated Sludge Process Overview. *International Journal of Environmental Science and Development 5, pp.1–5.*

Anik, M. & Cansizoglu, T., 2006. Dissolution kinetics of WO_3 in acidic solutions. *J. Appl. Electrochem.* 36, pp.603–608.

Brar, S. K., Verma, M., Tyagi, R. D. & Surampalli, R. Y., 2010. Engineered nanoparticles in wastewater and wastewater sludge – Evidence and impacts. *Waste Manag.* 30, pp.504–520.

Burkart, C., von Tümpling, W., Berendonk, T. & Jungmann, D., 2015. Nanoparticles in wastewater treatment plants: a novel acute toxicity test for ciliates and its implementation in risk assessment. *Environ. Sci. Pollut. Res.* 22, pp.7485–7494.

Chaüque, E. F. C., Zvimba, J. N., Ngila, J. C. & Musee, N., 2016. Fate, behaviour, and implications of ZnO nanoparticles in a simulated wastewater treatment plant. *Water SA* 42, pp.72–81.

Chaúque, E. F. C., Zvimba, J. N., Ngila, J. C. & Musee, N., 2014. Stability studies of commercial ZnO engineered nanoparticles in domestic wastewater. *Phys. Chem. Earth* 67–69, pp.140–144.

Demirel, B.,2016. The impacts of engineered nanomaterials (ENMs) on anaerobic digestion processes. *Process. Biochem.* 51, pp.308–313.

Department of water affairs. National Water Act- waste discharge standards, (2010). @ http://www.wateronline.co.za/wastewater/introduction/treatment-standards.html. Accessed: 16th April 2016.

Doolette, C. L., Mclaughlin, M. J., Kirby, J. K., Batstone, D. J.,Harris, Hugh H., Ge, H., & Cornelis, G., 2013. Transformation of PVP coated silver nanoparticles in a simulated wastewater treatment process and the effect on microbial communities. *Chem. Cent. J.* 7, pp.1–18.

Fan, J., Ji, F., Xu, X., Wang, Y., Yan, D., Xu, X.,Chen, Q., Xiong, J., & He, Q.,

2015. Prediction of the effect of fine grit on the MLVSS/MLSS ratio of activated sludge. *Bioresour. Technol.* 190, pp.51–56.

Gartiser, S., Flach, F., Nickel, C., Stintz, M., Damme, S., Schaeffer, A., Erdinger, L., Kuhlbusch, T. A. J., 2014. Behaviour of nanoscale titanium dioxide in laboratory wastewater treatment plants according to OECD 303A. *Chemosphere* 104, pp.197–204.

Gómez-Rivera, F., Field, J. A., Brown, D. & Sierra-Alvarez, R., 2012. Fate of cerium dioxide (CeO_2) nanoparticles in municipal wastewater during activated sludge treatment. *Bioresour. Technol.* 108, pp.300–304.

Gottschalk, F., Ort, C., Scholz, R. W. & Nowack, B., 2011. Engineered nanomaterials in rivers - Exposure scenarios for Switzerland at high spatial and temporal resolution. *Environ. Pollut.* 159, pp.3439–3445.

Greenberg, A., Clesceri, L. & Eaton, A. *Standard Methods for the Examination of Water and Wastewater*. American Public Health Association, 1992. @ https://www.mwa.co.th/download/file_upload/SMWW_4000-6000.pdf

Jennings, V., Goodhead, R. & Tyler, C. R., 2015. Ecotoxicology of Nanomaterials in Aquatic Systems. *Frontiers of Nanoscience, 8,pp.3-45*.

Klaine, S. J.,Alvarez, P. J. J. Batley, G. E., Fernandes, T. F., Handy, R. D., Lyon, D. Y., Mahendra, S., McLaughlin, M. J., & Lead, Jamie R., 2008. Nanomaterials in the Environment: Behaviour, fate, bioavailability and effects. *Environ. Toxicol. Chem.* 27, pp.1825–1851.

Li, Y., Yang, C., Guo, X., Dang, Z., Li, X., & Zhang, Q., 2015. Effects of humic acids on the aggregation and sorption of nano-TiO_2. *Chemosphere* 119, pp.171–176.

Liu, R., Lin, Y., Chou, L., Sheehan, S. W., He, W., Zhang, F., Hou, H. J.M., Wang, D., 2011. Water Splitting by Tungsten Oxide Prepared by Atomic Layer Deposition and Decorated with an Oxygen-Evolving Catalyst . *Angew. Chemie Int. Ed.* 50, pp.499–502.

Lynn, C. J., Dhir, R. K., Ghataora, G. S. & West, R. P., 2015. Sewage sludge ash characteristics and potential for use in concrete. *Constr. Build. Mater.* 98, pp767–779.

Magdziarz, A., Wilk, M., Gajek, M., Nowak W. D., Kopia, A., Kalemba-Rec, I., & Koziski, J. A., 2016. Properties of ash generated during sewage sludge combustion: A multifaceted analysis. *Energy* 113, pp85–94.

Monshi, A., Foroughi, M. R. & Monshi, M. R., 2012. Modified Scherrer Equation to Estimate More Accurately Nano-Crystallite Size Using XRD. *World J. Nano Sci. Eng.* 2, pp154–160.

Organization for Economic Co-operation and Development 303A, 2001. Aerobic Sewage Treatment – activated sludge units. Guidelines for the testing of chemicals. @ http://www.oecd.org/chemicalsafety/testing/34898616.pdf (assessed 15.04.16).

Puay, N.-Q., Qiu, G. & Ting, Y.P., 2015. Effect of Zinc oxide nanoparticles on biological wastewater treatment in a sequencing batch reactor. *J. Clean. Prod.* 88, pp139–145.

Qu, X., Alvarez, P. J. J. & Li, Q., 2013. Applications of nanotechnology in water and wastewater treatment. *Water Res.,* 47, pp3931–3946.

Sayed Abhudhahir, M. H. & Kandasamy, J., 2015. Synthesis and characterization of Manganese doped Tungsten oxide by Microwave irradiation method. *Mater. Sci. Semicond. Process.,* 40, pp695–700.

Shi, X., Li, Z., Chen, W., Qiang, L., Xia, J., Chen, M., Zhu, L., & Alvarez, P.J. J., 2016. Fate of TiO_2 nanoparticles entering sewage treatment plants and bioaccumulation in fish in the receiving streams. *NanoImpact,* 3–4, pp96–103.

Simelane, S., Ngila, J. C. & Dlamini, L. N., 2017. The Effect of Humic Acid on the Stability and Aggregation Kinetics of WO_3 Nanoparticles. in Press *Particulate Science and Technology*. doi:10.1080/02726351.2017.1302536. Accessed 24 March 2017.

Strigul, N., Koutsospyros, A. & Christodoulatos, C., 2009. Tungsten in the former

Soviet Union: Review of environmental regulations and related research. *L. Contam. Reclam.,* 17, pp189–215.

The Royal Society & The Royal Academy of Engineering, 2004. Nanoscience and nanotechnologies: opportunities and uncertainties. The Royal Society RS policy document 19/04, pp1-116, London.

Wentzel, M. C., Ubisi, M. F., Lakay, M. T. & Ekama, G. A., 2002. Incorporation of inorganic material in anoxic/aerobic-activated sludge system mixed liquor. *Water Res.,* 36, pp5074–5082.

Zhang, Y., Chen, Y., Westerhoff, P. & Crittenden, J., 2009. Impact of natural organic matter and divalent cations on the stability of aqueous nanoparticles. *Water Res.,* 43, pp4249–4257.

Zheng, H., Ou, J. Z., Strano, M. S., Kaner, R. B. & Mitchell, A., 2011. Nanostructured Tungsten Oxide – Properties , Synthesis , and Applications. *Adv. Funct. Mater.,* 21, pp2175–2196.

Zhou, X., Huang, B., Zhou, T., Liu, Y. & Shi, H., 2015. Aggregation behaviour of engineered nanoparticles and their impact on activated sludge in wastewater treatment. *Chemosphere,* 119,pp568–76.

Zhu, M., Wang, H., Keller, A. A., Wang, T. & Li, F., 2014. The effect of humic acid on the aggregation of titanium dioxide nanoparticles under different pH and ionic strengths. *Sci. Total Environ.,*487, pp375–380.

CHAPTER 6

CONCLUSIONS AND RECOMMENDATIONS

6.1 Conclusions

Monoclinic WO_3 was synthesised and characterized using Powder x-ray diffraction spectroscopy (PXRD), transmission electron microscopy (TEM), Brunauer-Emmett-Teller (BET), UV-Vis spectrometer (DRS), Raman, Fourier transformed Infrared (FTIR), Thermogravimetric Analysis (TGA) and Zetasizer Nano ZS. The nanoparticles had a surface area of 3.544 m2g-1 and an average particle size of 236.5 nm with a crystal size of 15.0 nm.

The stability of the *m*-WO_3 nanoparticles in water was found to increase as the concentration of humic acid increased. This is due to the bridging effect of the humic acid which then increases the repulsion forces between nanoparticles thus inducing steric hindrances. The reduction of the rate of agglomeration by 0.2 nm/s in water in the presence of humic acid provided further evidence to the increased stability of the nanoparticles. However, the existence of the cations in the matrix resulted in agglomeration of nanoparticles. This is due to the capability of the cations to compress the electric double layer thus resulting in the van der Waals attraction energies being dominant in order of $Ca^{2+} > Mg^{2+} > Na^{+}$.

The pzc of the nanoparticles was determined to be at pH 2.5 in DI water. Therefore, at post pzc, the nanoparticles were stable. Moreover, at pH 5, the nanoparticles demonstrated substantial agglomeration without compelling the compression of the electric double layer in the DI suspension. Thus, WO_3 nanoparticles are most likely to be stable and be transported longer distances in both surface and ground waters

The impact of humic acid on the microbiological population in the aeration chambers was investigated. Humic acid had no adverse effects on the functionality of the SWTP as acclimatization of the inoculum was successful with a removal efficiency greater than 80% in COD. The introduction of 5 mg/L nanoparticles has no impact on the COD removal. However, increased concentrations of the WO_3 nanoparticles had an average COD values also increasing resulting in reduced COD removal efficiency of 68%. This observation is due to that nanoparticle inhibiting the microbial oxygen consumption. The total suspended solids also increased while the MLVSS/MLSS ratio decreased due to an increased concentration of inorganic matter in the activated sludge. Thus, suggesting that WO_3 nanoparticles were adsorbed on the sludge.

The fate of the WO_3 nanoparticle was studied through analysis of the sludge. Both SEM mapping an EDS revealed the presence of W which was evenly distributed in the sludge. XRD analysis showed patterns of crystalline monoclinic WO_3 nanoparticles revealing that the activated sludge had no impact on the nanoparticles as the polymorph was maintained. ICP-OES analysis showed that 80% of the W was retained in the sludge while about 20-21% was passed with the effluent.

6.2 Recommendations for further work

The objectives of this research were achieved. However, several gaps have been identified for further work in future for accurate risk assessment of WO_3 nanoparticles in the wastewater treatment plant.

➢ The fate and behaviour of WO_3 nanoparticles during activated sludge in WWTPs was investigated. However, wastewater is composed of other complexing and precipitation agents such as humic acid, tannic acid, and sulphides, which are all pH dependent. Therefore, investigating the speciation of WO_3 nanoparticles in WWTPs may contribute to the development of appropriate methodologies for the removal of nanoparticles before the disposal or reuse of bio-solid.

❖ To fully understand the effect of the nanoparticles on the activated sludge investigation of the bacterial species that are highly sensitive to the presence of WO_3 should be studied to develop methodologies to overcome the adverse effect.

- The adverse impacts on the wastewater treatment processes, such as anaerobic digestion should also be conducted to fully determine the appropriate stage for the application of the nanoparticles in the treatment plant.

APPENDIX A: SEM images of pristine WO_3 depicting the different morphologies observed

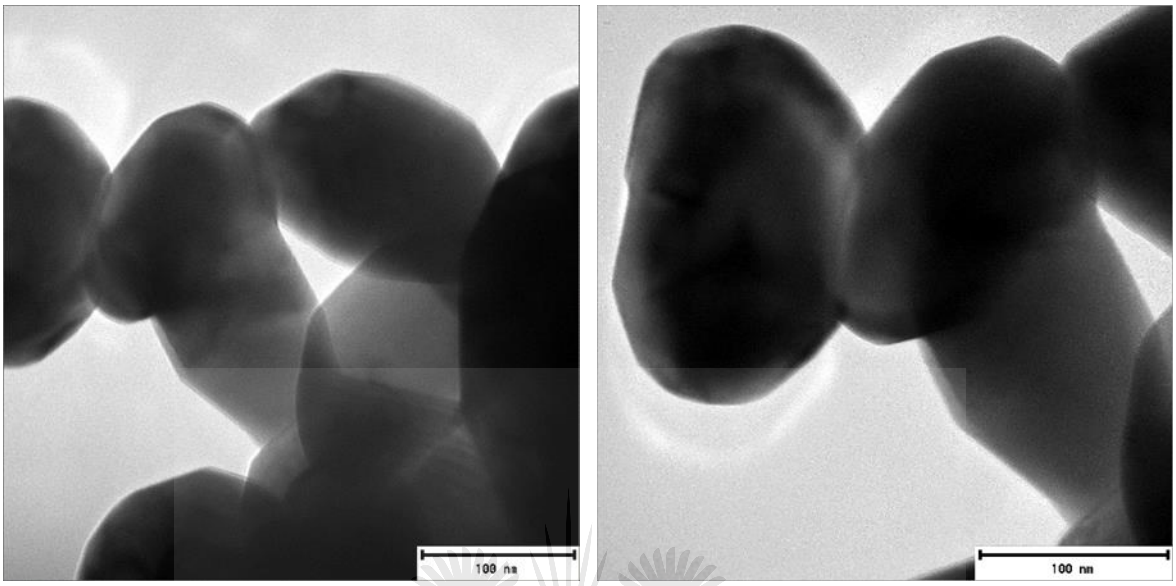

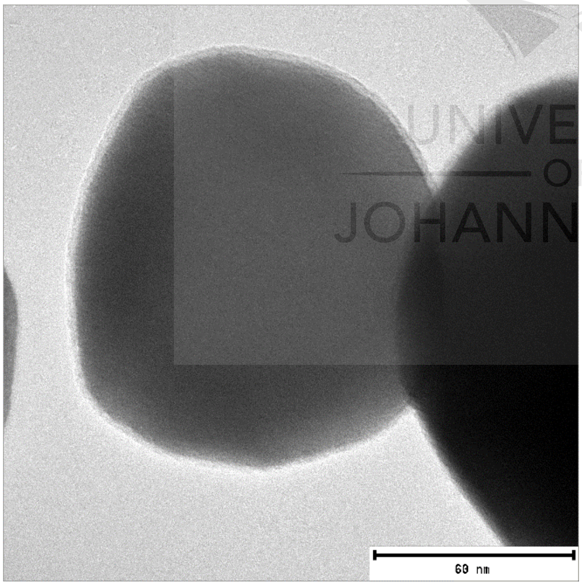

:

APPENDIX B: Plots of Hydro diameter against Time in Deionized Water Suspensions

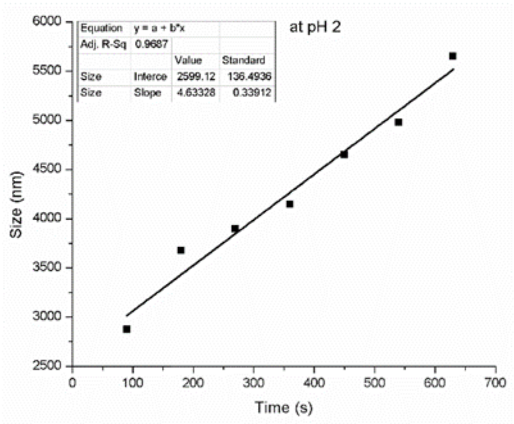

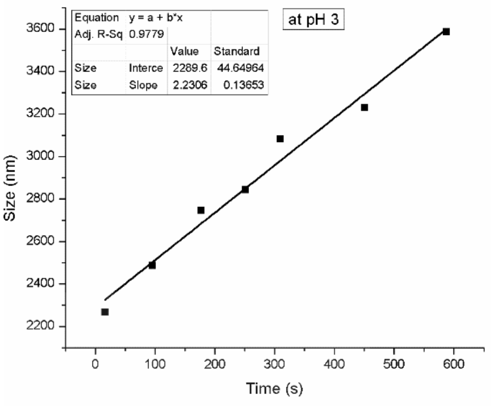

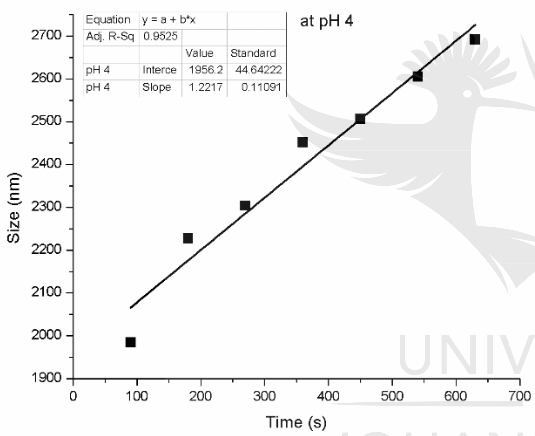

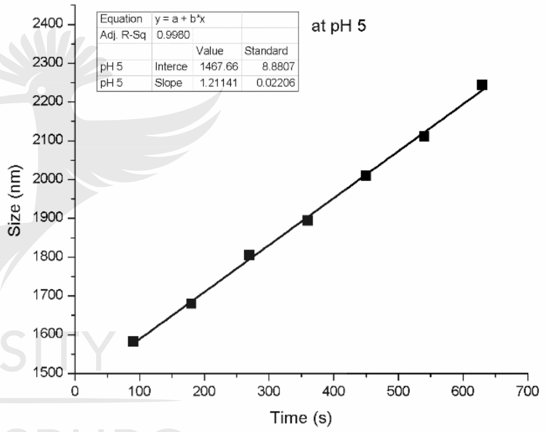

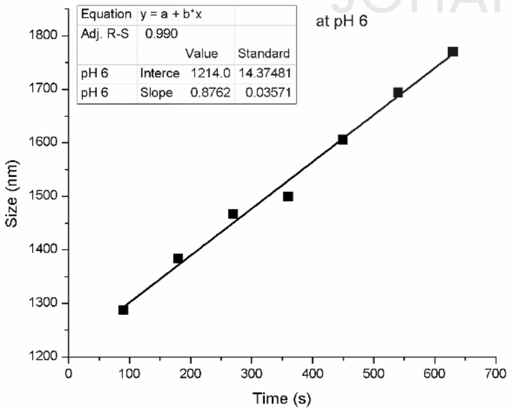

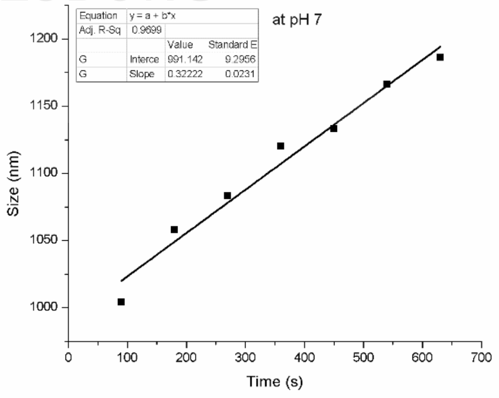

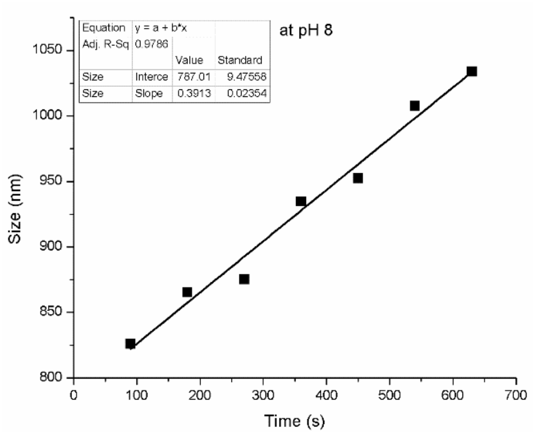
at pH 8
Equation | y = a + b*x
Adj. R-Sq | 0.9786
Value | Standard
Size | Interce | 787.01 | 9.47558
Size | Slope | 0.3913 | 0.02354
Size (nm)
1050
1000
950
900
850
800
0
100
200
300
400
500
600
700
Time (s)

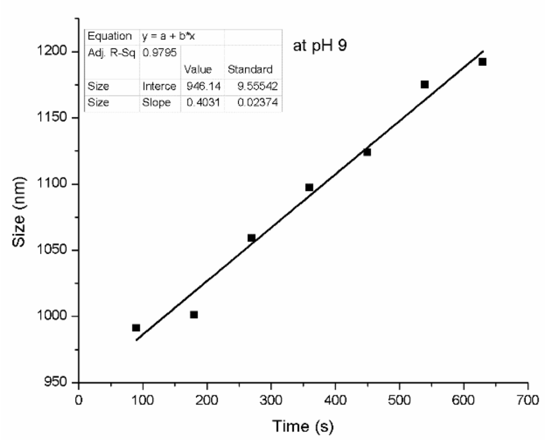
at pH 9
Equation | y = a + b*x
Adj. R-Sq | 0.9795
Value | Standard
Size | Interce | 946.14 | 9.55542
Size | Slope | 0.4031 | 0.02374
Size (nm)
1200
1150
1100
1050
1000
950
0
100
200
300
400
500
600
700
Time (s)

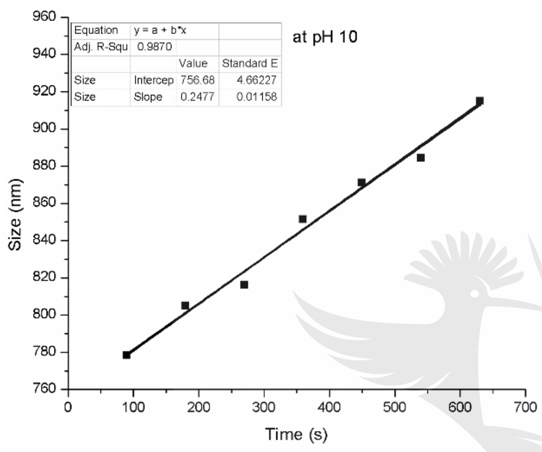
at pH 10
Equation | y = a + b*x
Adj. R-Squ | 0.9870
Value | Standard E
Size | Intercep | 756.68 | 4.66227
Size | Slope | 0.2477 | 0.01158
Size (nm)
960
940
920
900
880
860
840
820
800
780
760
0
100
200
300
400
500
600
700
Time (s)

APPENDIX C: Effect of Ionic Strength Raw data

Sodium Chloride						
Ionic Strength	Hydrodynamic diameter		Zeta potential		Agglomeration rate	
	nm	SD	mV	SD	nm/s	SD
0.2	1005	50.25	-19.3	0.579	0.315	0.02205
0.4	1046	52.3	-18.9	0.567	0.399	0.02793
0.6	1140	57	-18.7	0.561	0.41	0.0287
0.8	1122	56.1	-17.9	0.537	0.537	0.03759
1	1193	59.65	-17.9	0.537	0.625	0.04375
2	1287	64.35	-17.1	0.513	0.686	0.04802
4	1251	62.55	-16.1	0.483	0.74	0.0518
6	1290	64.5	-14.7	0.441	0.754	0.05278
8	1335	66.75	-13.7	0.411	0.868	0.06076
10	1370	68.5	-13.5	0.405	1.306	0.09142

Magnesium Chloride						
Ionic Strength	Hydrodynamic diameter		Zeta potential		Agglomeration rate	
	nm	SD	mV	SD	nm/s	SD
0.2	1799	89.95	-18.17	0.9085	0.936	0.03744
0.4	1975	98.75	-17.86	0.893	1.387	0.05548
0.6	1986	99.3	-16.37	0.8185	0.482	0.01928
0.8	2542	127.1	-16.1	0.805	1.749	0.06996
1	2869	143.45	-15.53	0.7765	1.576	0.06304
2	2701	135.05	-15.5	0.775	1.175	0.047
4	2567	128.35	-15.27	0.7635	2.298	0.09192
6	2995	149.75	-14.07	0.7035	1.115	0.0446
8	3002	150.1	-13.35	0.6675	2.849	0.11396
10	3151	157.55	-7.5	0.375	4.705	0.1882

Calcium Chloride						
Ionic Strength	Hydrodynamic diameter		Zeta potential		Agglomeration rate	
	nm	SD	mV	SD	nm/s	SD
0.2	1232	36.96	-14.17	0.9919	1.75	0.0525
0.4	1418	42.54	-14.86	1.0402	3.62	0.1086
0.6	1076	32.28	-12.37	0.8659	3.023	0.09069
0.8	1317	39.51	-12.1	0.847	3.67	0.1101
1	1770	53.1	-12.53	0.8771	2.901	0.08703
2	1872	56.16	-10.5	0.735	3.028	0.09084
4	1644	49.32	-10.27	0.7189	3.2	0.096
6	2423	72.69	-9.07	0.6349	4.014	0.12042
8	3549	106.47	-7.35	0.5145	4.702	0.14106
10	4235	127.05	-3.5	0.245	4.309	0.12927

APPENDIX D: Effect of Electrolyte Valency Raw data at 0.9 mM concentration

Sodium Chloride						
pH	Hydrodynamic diameter		Zeta potential		Agglomeration rate	
	nm	SD	mV	SD	nm/s	SD
2	2057	143.99	-9.1	0.637	1.508	0.10556
3	1562	109.34	-18.57	1.2999	1.158	0.08106
4	1331	93.17	-25.37	1.7759	1.054	0.07378
5	1307	91.49	-24.67	1.7269	0.989	0.06923
6	1155	80.85	-25.8	1.806	0.849	0.05943
7	1136	79.52	-26	1.82	0.806	0.05642
8	1066	74.62	-25.17	1.7619	0.802	0.05614
9	1055	73.85	-28.3	1.981	0.639	0.04473
10	1008	70.56	-28.3	1.981	0.225	0.01575

Magnesium Chloride						
pH	Hydrodynamic diameter		Zeta potential		Agglomeration rate	
	nm	SD	mV	SD	nm/s	SD
2	3181	159.05	-2.53	0.1012	2.725	0.19075
3	2860	143	-9.32	0.3728	2.44	0.1708
4	2621	131.05	-11.1	0.444	2.373	0.16611
5	2531	126.55	-12.36	0.4944	2.13	0.1491
6	2426	121.3	-12.6	0.504	1.928	0.13496
7	2182	109.1	-13.1	0.524	1.817	0.12719
8	2248	112.4	-13.87	0.5548	1.92	0.1344
9	2104	105.2	-13.53	0.5412	1.555	0.10885
10	1544	77.2	-14.63	0.5852	1.496	0.10472

Calcium Chloride						
pH	Hydrodynamic diameter		Zeta potential		Agglomeration rate	
	nm	SD	mV	SD	nm/s	SD
2	4932	246.6	2.29	0.1603	4.22	0.211
3	4611	230.55	-3.96	0.2772	3.42	0.171
4	4271	213.55	-7.23	0.5061	2.039	0.10195
5	3136	156.8	-9.18	0.6426	1.85	0.0925
6	2936	146.8	-8	0.56	1.445	0.07225
7	1865	93.25	-10.11	0.7077	1.056	0.0528
8	1486	74.3	-12.45	0.8715	1.005	0.05025
9	1485	74.25	-13.43	0.9401	0.956	0.0478
10	1056	52.8	-15.16	1.0612	0.478	0.0239

APPENDIX E: Influence of Humic acid studied at pH 5 in 0.9 mM electrolytic solutions

Deionized water and 0.9 mM electrolytic solutions with Humic Acid

HA Concentration (mg/L)	Zeta Potential (mV)							
	DI	SD	NaCl	SD	$MgCl_2$	SD	$CaCl_2$	SD
1	-15.18	1.0626	-13.33	1.333	-12.83	1.0264	-11.1	0.888
2	-18.1	1.267	-13.83	1.383	-12.87	1.0296	-11.7	0.936
3	-17.1	1.197	-14.83	1.483	-12.27	0.9816	-11.4	0.912
4	-19.37	1.3559	-16.7	1.67	-13.1	1.048	-11.3	0.904
5	-19.9	1.393	-17.99	1.799	-12.77	1.0216	-11.63	0.9304
10	-21.2	1.484	-19.26	1.926	-13.1	1.048	-12.4	0.992

Deionized water with different concentrations of Humic Acid

Time (s)	Hydrodynamic diameter (nm)					
	1 ppm	2 ppm	3 ppm	4 ppm	5 ppm	10 ppm
90	1474	1727	1279	1874	1320	1526
180	1523	1883	1482	1954	1404	1606
270	1690	1949	1554	2050	1573	1781
360	1726	2098	1678	2194	1633	1874
450	1832	2226	1775	2330	1765	1956
540	1989	2382	1864	2426	1789	2028
630	2001	2444	2166	2492	1811	2164

Sodium Chloride with different concentrations of Humic Acid

Time (s)	Hydrodynamic diameter (nm)					
	1 ppm	2 ppm	3 ppm	4 ppm	5 ppm	10 ppm
90	1439	1535	1718	1695	1557	1465
180	1523	1715	1981	1700	1787	1584
270	1653	1829	2054	1870	1819	1677
360	1795	1945	2196	1908	1990	1899
450	1883	2047	2215	2093	2073	1936
540	1926	2161	2300	2277	2114	2070
630	2081	2227	2371	2290	2290	2175

Magnesium Chloride with different concentrations of Humic Acid						
	Hydrodynamic diameter (nm)					
Time (s)	1 ppm	2 ppm	3 ppm	4 ppm	5 ppm	10 ppm
90	2493	2538	2400	2482	2332	2259
180	2615	2668	2605	2597	2397	2314
270	2818	2779	2812	2604	2421	2348
360	2942	2870	2918	2801	2608	2401
450	3085	2995	2998	2944	2769	2572
540	3284	3205	3090	3041	2804	2656
630	3396	3276	3122	3116	3041	3060

Calcium Chloride with different concentrations of Humic Acid						
	Hydrodynamic diameter (nm)					
Time (s)	1 ppm	2 ppm	3 ppm	4 ppm	5 ppm	10 ppm
90	2952	2882	2704	2599	2297	2228
180	3116	2974	2819	2624	2501	2369
270	3336	3171	2947	2935	2700	2489
360	3416	3281	3096	3237	2701	2566
450	3614	3348	3293	3312	2719	2656
540	3719	3407	3329	3388	3073	2733
630	3828	3509	3479	3546	3110	2843

APPENDIX F: SEM Mapping and EDS spectra of the test unit waste sludge

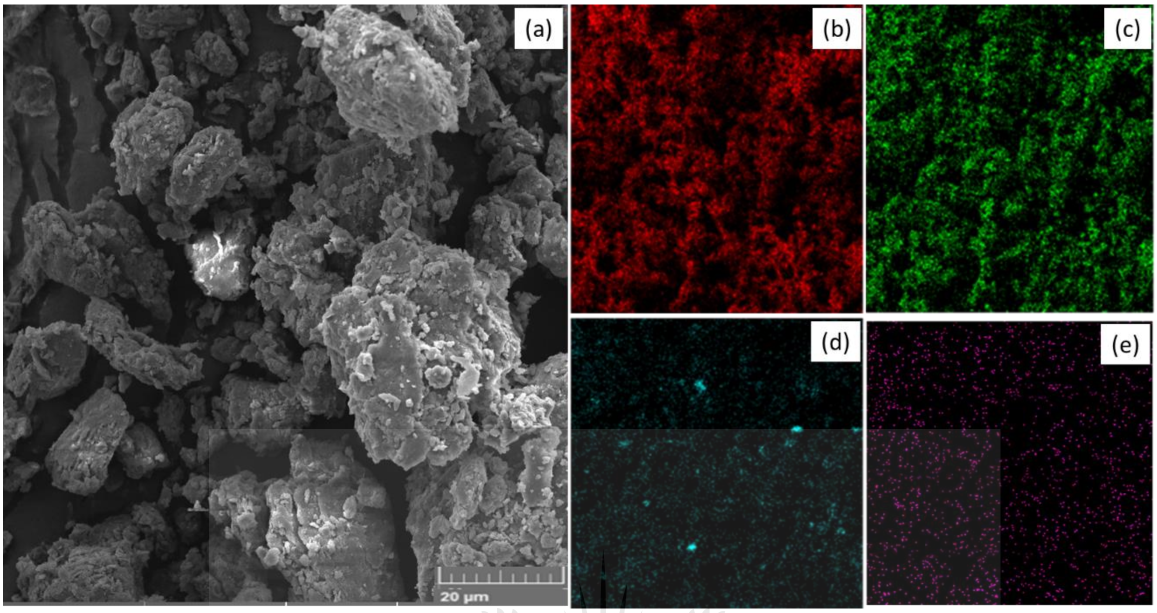

SEM image of dried the sludge during the addition of 5 mgL^{-1} WO_3 with the respective inserts of (b) carbon, (c) oxygen, (d) silicon and (e) tungsten after SEM mapping of the image.

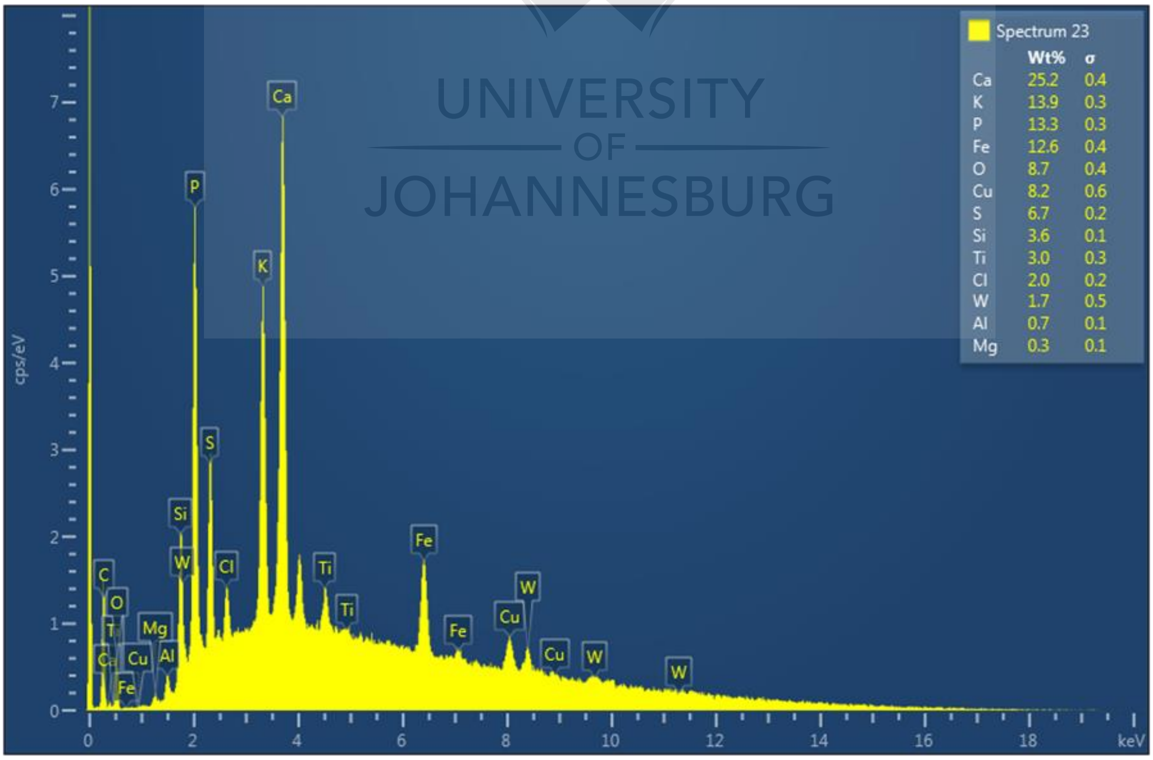

	Wt%	σ
Ca	25.2	0.4
K	13.9	0.3
P	13.3	0.3
Fe	12.6	0.4
O	8.7	0.4
Cu	8.2	0.6
S	6.7	0.2
Si	3.6	0.1
Ti	3.0	0.3
Cl	2.0	0.2
W	1.7	0.5
Al	0.7	0.1
Mg	0.3	0.1

EDS analysis of the activated sludge in the test unit spiked with 5 mgl^{-1} WO_3 NPs.

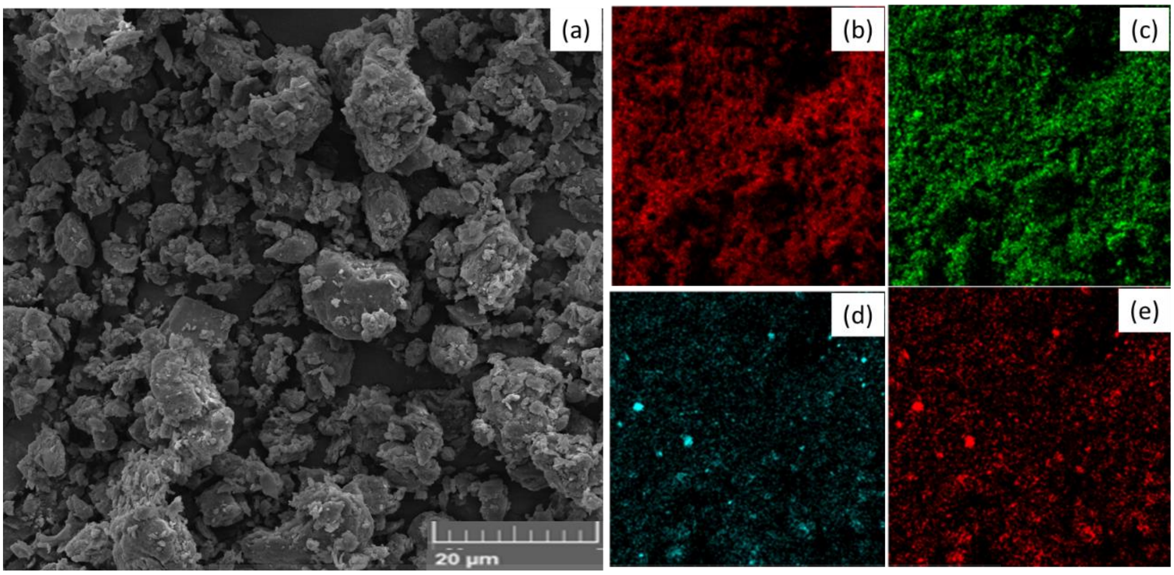

SEM image of dried the sludge during the addition of 10 mgL^{-1} WO_3 with the respective inserts of (b) carbon, (c) oxygen, (d) silicon and (e) tungsten after SEM mapping of the image.

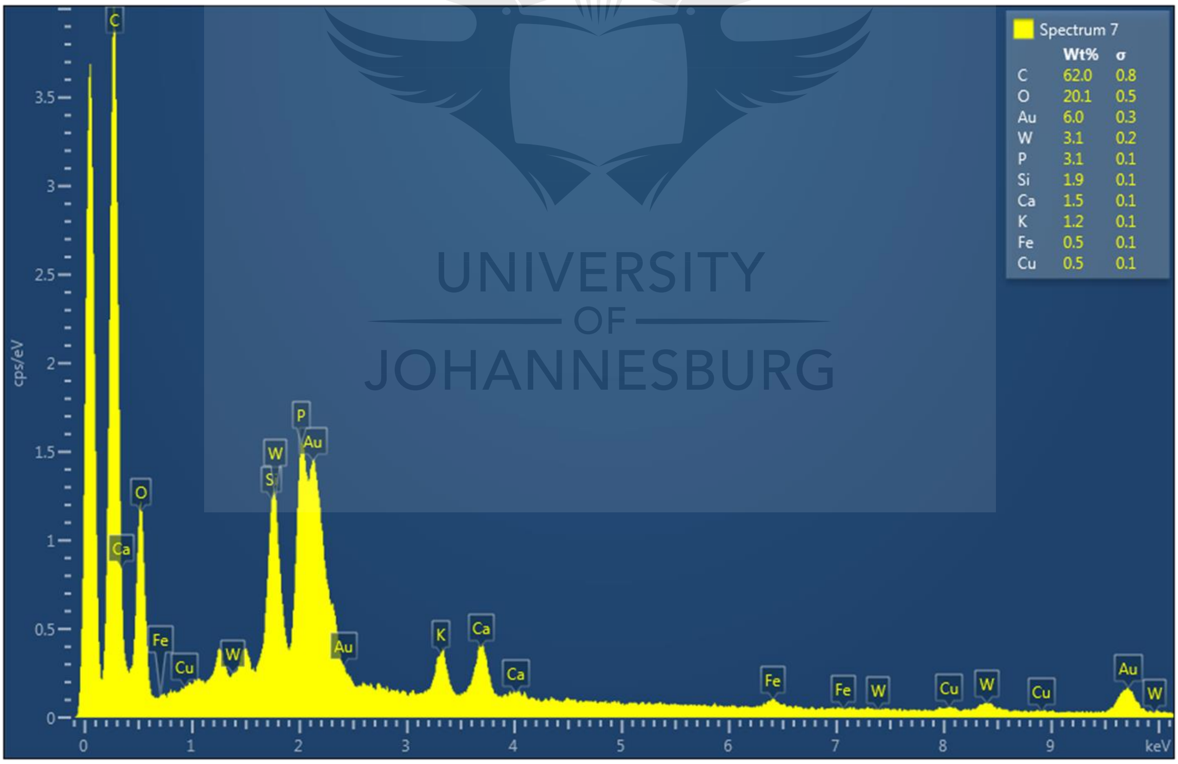

	Wt%	σ
C	62.0	0.8
O	20.1	0.5
Au	6.0	0.3
W	3.1	0.2
P	3.1	0.1
Si	1.9	0.1
Ca	1.5	0.1
K	1.2	0.1
Fe	0.5	0.1
Cu	0.5	0.1

EDS analysis of the activated sludge in the test unit spiked with 10 mgl^{-1} WO_3 NPs.

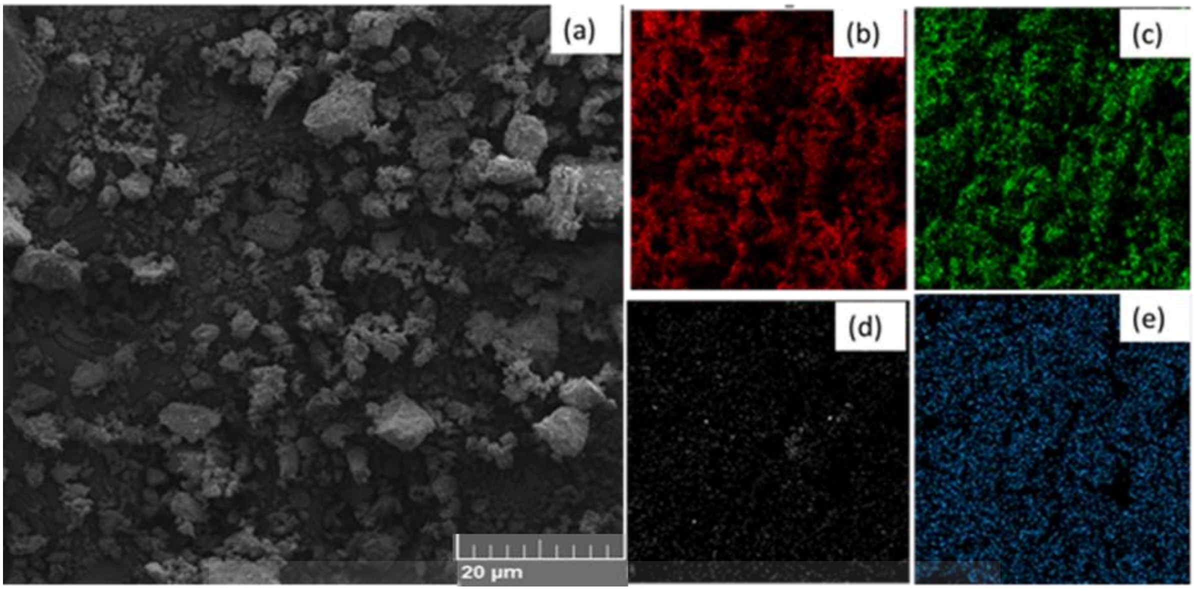

SEM image of dried the sludge during the addition of 20 mgL^{-1} WO_3 with the respective inserts of (b) carbon, (c) oxygen, (d) silicon and (e) tungsten after SEM mapping of the image.

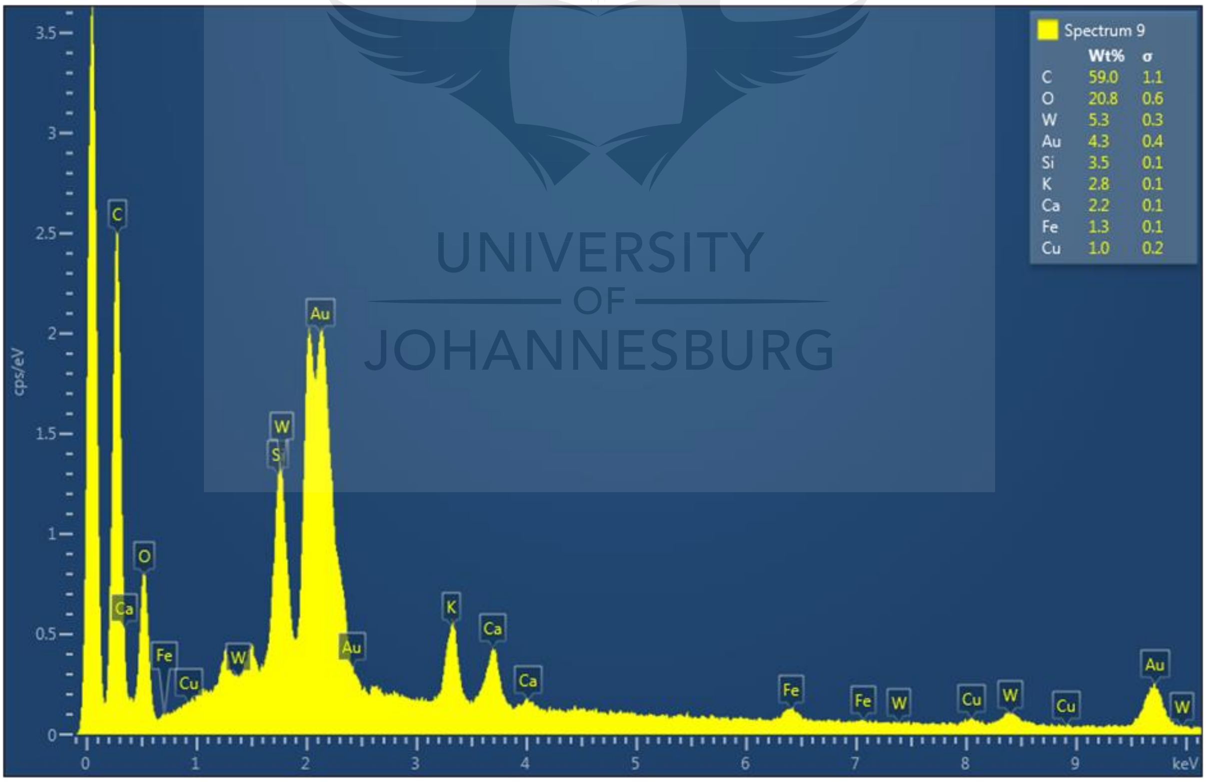

EDS analysis of the activated sludge in the test unit spiked with 20 mgl^{-1} WO_3 NPs.

APPENDIX G: Measured influent parameters during Simulation

Parameters	SRT 1		SRT 2		SRT 3		SRT 4		SRT 5		SRT 6	
	Mean	**SD**	**Mean**	**SD**	**Mean**	**SD**	**Mean**	**SD**	**Mean**	**SD**	**Mean**	**SD**
Control												
pH	7.20	2.9	7.19	0.1	7.57	0.2	8.18	0.1	8.13	0.1	8.32	0.2
Conductivity (µS/cm)	1960	28.3	1378.5	79.9	1168		1280	25.3	1114.3	21.8	1114.3	56.4
TDS (mg/L)	994.8		719		585		634		568.8	17.9	562.8	30.2
COD (mg/L)	440.9	12.2	461.2	45.1	459.1	70.8	500.2	44.3	377.7	39.0	484.1	24.1
TSS												
BOD5 (mgL-1)	-	-	-	-	2.95	0.05	3.3	0.1	3.75	0.05	2.95	0.15
Test												
pH	7.20	2.9	7.19	0.04	7.74	0.3	8.24	0.2	8.05	0.2	8.14	0.2
Conductivity (µS/cm)	1970	21.2	1407	57.9	1148		1157	12.8	1183	31.8	1118.5	43.1
TDS (mg/L)	994.3		730		581		592.7		571.8	12.8	531	36.0
COD (mg/L)	445.9	3.1	428.6	32.2	393.3	30.7	453.6	52.4	393.3	30.6	490.1	19.9
TSS												
BOD5 (mg/L)	-	-	-	-	3.45	0.25	3.15	0.35	3.0	0.2	3.4	0.4

Parameters	SRT 7		SRT 8		SRT 9		SRT 10		SRT 11	
	Mean	**SD**	**Mean**	**SD**	**Mean**	**SD**	**Mean**	**SD**	**Mean**	**SD**
Control										
pH	8.00	0.4	8.16	0.1	8.15	0.4	8.13	0.2	8.13	0.2
Conductivity (µS/cm)	1140	43.7	1167	29.0	1125	47.7	1118.6	47.7	1143.1	46.2
TDS (mg/L)	533.7	21.4	570.2	13.9	556.3	25.0	549.1	20.2	576.9	34.5
COD (mg/L)	489.1	40.3	335.9	19.4	446.6	74.8	407.7	29.6	395.9	11.0
TSS										
BOD5 (mgL-1)	2.75	0.75	3.55	0.05	3.85	0.35	2.9	0.9	2.4	0.4
Test										
pH	8.26	0.1	8.30	0.5	8.30	0.3	8.18	0.3	8.15	0.1
Conductivity (µS/cm)	1323.5	54.7	1118	38.6	1186.7	34.5	1116.4	71.4	1169.9	42.4
TDS (mg/L)										
COD (mg/L)	482.3	32.1	384.7	45.8	407.5	89.5	390.4	21.0	394.8	10.9
TSS	564.5	25.0	594.1	31.3	538.1	27.6	551.9	42.6	595.2	12.2
BOD5 (mg/L)	2.6		3.44	0.5	3.45	0.45	3.15	0.55	2.75	0.05
SD: Standard Deviation										

APPENDIX H: Measured parameters of the Aerobic chambers during the treatment process

Parameters	**SRT 1**		**SRT 2**		**SRT 3**		**SRT 4**		**SRT 5**		**SRT 6**		**SRT 7**	
	Mean	**SD**	**Mean**	**SD**	**Mean**	**SD**	**Mean**	**SD**	**Mean**	**SD**	**Mean**	**SD**	**Mean**	**SD**
Control														
Temperature (˚C)	22.9	0.6	23.3	0.5	23.1	0.4	24.0	1.1	24.1	0.5	24.0	0.9	23.8	0.4
DO (mg/L)	3.68	0.33	3.91	0.27	3.77	0.32	3.82	0.38	3.91	0.20	4.10	0.21	3.48	0.54
MLSS (mg/L)	1431.3	53.8	1445	117.5	1400	40	1358.8	73.7	1378.4	25.6	1405	43.2	1511.3	74.9
MLVSS (mg/L)	1351	37.5	1247.5	126.3	1188.8	36.9	1195	80	1202.6	25.0	1188.0	36.7	1302.5	52.5
VSS/SS	0.92	0.02	0.86	0.03	0.85	0.01	0.88	0.02	0.87	0.01	0.85	0.01	0.86	0.03
Test														
Temperature (˚C)	22.6	0.6	23.1	0.2	22.0	0.2	24.2	1.2	24.3	0.6	24.1	0.7	22.9	0.8
DO (mg/L)	3.79	0.29	4.00	0.20	3.82	0.28	3.99	0.19	3.93	0.17	3.99	0.15	3.78	0.38
MLSS (mg/L)	1616.3	48.8	1502.5	56.3	1562.5	51.2	1522.5	102.9	1611.2	31.1	1562.8	38.1	1816.2	43.5
MLVSS (mg/L)	1496.2	36.3	1321.3	58.8	1365	57.5	1385	85.0	1412.5	40.0	1348.3	25.7	1515	157.5
VSS/SS	0.93	0.01	0.88	0.02	0.87	0.02	0.86	0.01	0.88	0.03	0.87	0.02	0.84	0.03
SD: Standard deviation														

APPENDIX I: Measured parameters of the Effluent during the treatment process

---

Parameters	SRT 1		SRT 2		SRT 3		SRT 4		SRT 5		SRT 6		SRT 7	
	Mean	**SD**	**Mean**	**SD**	**Mean**	**SD**	**Mean**	**SD**	**Mean**	**SD**	**Mean**	**SD**	**Mean**	**SD**
Control														
pH	7.36	0.2	6.90	0.1	7.28	0.3	7.22	0.1	7.20	0.3	7.16	0.4	7.24	0.3
Conductivity (mg/L)	1279.3	161.3	1026.5	95.3	840	-	845.3	15.5	867	-	753.4	45.4	749.7	38.4
TDS (mg/L)	638		509.8	-	420	-	434	-	372.3	25.8	371.9	24.3	373.3	11.6
COD (mg/L)	72.4	25.9	67.9	7.2	77	9.6	68.2	7.1	57.9	5.5	52.7	4.2	64.7	3.90
BOD$_5$ (mg/L)	-	-	0.8	-	1.05	0.15	1.10	0.1	0.75	0.15	0.3	-	0.45	0.14
TSS (mg/L)	9.0	2.85	7.6	1.8	7.90	2.32	6.0	2.27	7.30	2.18	8.10	2.37	7.20	1.21
Test														
pH	7.29	0.2	6.84	0.3	7.34	0.2	7.19	0.1	7.13	0.4	7.16	0.3	7.02	0.5
Conductivity (mg/L)	1361.5	129.5	1024.8	94.4	1033	-	1021	21.5	876	-	764.9	56.6	811.7	49.2
TDS (mg/L)	677.3	-	512	-	482	-	512	-	371.4	24.1	379.9	39.1	426.8	16.4
COD (mg/L)	80.9	30.0	66.9	9.4	80.3	12.8	67.4	3.9	63.4	6.6	55.9	7.3	60.9	4.9
BOD$_5$ (mg/L)	-	-	1.05	0.05	0.75	0.07	0.85	0.04	0.65	0.14	0.25	0.05	0.5	0.2
TSS (mg/L)	9.1	2.40	7.60	2.11	7.5	1.29	6.71	1.44	8.9	2.39	7.1	1.27	8.4	1.97

SD: Standard Deviation